ANL-75-72

ANL-75-72

LIGHT-WATER-REACTOR SAFETY RESEARCH PROGRAM: QUARTERLY PROGRESS REPORT

July–September 1975

ARGONNE NATIONAL LABORATORY, ARGONNE, ILLINOIS

Prepared for the U. S. NUCLEAR REGULATORY COMMISSION
Office of Nuclear Regulatory Research

DISCLAIMER

The facilities of Argonne National Laboratory are owned by the United States Government. Under the terms of a contract (W-31-109-Eng-38) between the U. S. Energy Research and Development Administration, Argonne Universities Association and The University of Chicago, the University employs the staff and operates the Laboratory in accordance with policies and programs formulated, approved and reviewed by the Association.

MEMBERS OF ARGONNE UNIVERSITIES ASSOCIATION

The University of Arizona
Carnegie-Mellon University
Case Western Reserve University
The University of Chicago
University of Cincinnati
Illinois Institute of Technology
University of Illinois
Indiana University
Iowa State University
The University of Iowa
Kansas State University
The University of Kansas
Loyola University
Marquette University
Michigan State University
The University of Michigan
University of Minnesota
University of Missouri
Northwestern University
University of Notre Dame
The Ohio State University
Ohio University
The Pennsylvania State University
Purdue University
Saint Louis University
Southern Illinois University
The University of Texas at Austin
Washington University
Wayne State University
The University of Wisconsin

Printed in the United States of America
Available from
National Technical Information Service
U. S. Department of Commerce
5285 Port Royal Road
Springfield, Virginia 22161
Price: Printed Copy $6.50; Microfiche $2.25

Distribution Categories:
Water Reactor Safety
Research—Fuel Behavior
(NRC-3)
Water Reactor Safety
Research—Analysis Development
(NRC-4)

ANL-75-72

ARGONNE NATIONAL LABORATORY
9700 South Cass Avenue
Argonne, Illinois 60439

LIGHT-WATER-REACTOR SAFETY RESEARCH PROGRAM: QUARTERLY PROGRESS REPORT

July–September 1975

Robert G. Sachs, Laboratory Director
Jack A. Kyger, Associate Laboratory Director

Previous reports in this series:

ANL-75-28 January-March 1975
ANL-75-58 April-June 1975

THIS PAGE

WAS INTENTIONALLY

LEFT BLANK

TABLE OF CONTENTS

TABLE OF CONTENTS

TABLE OF CONTENTS

LIST OF FIGURES

LIST OF FIGURES

LIST OF FIGURES

LIST OF FIGURES

LIST OF FIGURES

LIST OF FIGURES

LIST OF TABLES

ABSTRACT

This progress report summarizes the Argonne National Laboratory work performed during July, August, and September 1975 on water-reactor-safety heat-transfer and flow problems. The following research and development areas are covered: (1) Loss-of-coolant Accident Research; Heat Transfer and Fluid Dynamics; (2) Transient Fuel Response and Fission-product Release Program; and (3) Mechanical Properties of Zircaloy Containing Oxygen. Also included is an appendix on Kinetics of Fission Gas and Volatile Fission-product Behavior under Transient Conditions in LWR Fuel.

I. LOSS-OF-COOLANT ACCIDENT RESEARCH: HEAT TRANSFER AND FLUID DYNAMICS

Responsible Section Managers:
M. A. Grolmes, R. E. Henry, and P. A. Lottes, RAS

Current activities include analytical and experimental investigations related to (A) the occurrence of system oscillations during the reflood stage of a PWR LOCA (pressurized-water-reactor loss-of-coolant accident); (B) improved mathematical formulations for representing the fluid dynamics of vapor-liquid mixtures; (C) use of the "drift-flux model" as a potentially more general and more accurate basis for correlating vapor-liquid phase velocities and vapor volume fractions; and (D) the occurrence of critical heat fluxes (CHF's) during the blowdown stage of a PWR LOCA. Summaries of progress on each of these activities follow:

A. Analysis of PWR FLECHT-SET Oscillations. This study has now been concluded. The results indicate that the idealized model devised to account for the effects of transverse flows cannot show that frictional dissipation as a result of such flows will cause significant damping of oscillatory flooding behavior.

B. Vapor Generation in Flashing Flows. A mechanistic description for nonequilibrium vapor generation rate in steady, flashing flows has been formulated. This description shows that one must analyze the vapor-formation process in Lagrangian space. This has been completed and the results applied to bubble growth in decompression processes. Accurate predictions of bubble growth in exponential pressure-decay and linear-saturation temperature-decay fields have been demonstrated validating the approach taken. Recent data of steady-state flashing in a straight-divergent duct have also been examined, and calculations of the nonequilibrium vapor generation rates from these data are presented. Significant differences between equilibrium and nonequilibrium generation rates are found, but the data indicate the need for a more accurate and extensive series of tests.

C. One-dimensional Drift-flux Modeling; Vapor-drift Velocity in Annular-flow Regime. In annular two-phase flows, the relative motions between phases are governed by the interfacial geometry, the body force field, and the interfacial momentum transfer. A constitutive equation for the vapor-drift velocity has been developed by taking into account those macroscopic effects of the structured two-phase flows.

D. Transient Critical Heat Flux. A 1-sec inlet flow stoppage before blowdown did not precipitate an immediate critical heat flux (CHF). Two CHF's were observed in a longer transient. The first CHF at 400 msec was localized at the bottom 8 in. of test section; it was quenched subsequently. The second CHF occurred at a time corresponding to the complete depletion of coolant in the test section.

A. Analysis of PWR FLECHT-SET Oscillations (R. P. Stein, RAS)

A mathematical model of the FLECHT-SET Phase A apparatus, which includes an idealized representation of transverse flows in the simulated core region, was described in the previous Quarterly Progress Report.[1]* It was noted that an important objective was to develop a model of sufficient simplicity to make it unnecessary to use or develop a large computer code, so that results could be obtained quickly. The purpose of including transverse flows in the model was to provide a basis for studying the effects of such flows on oscillatory flooding behavior.

Large-amplitude oscillations were observed in the FLECHT-SET experiments. However, transversely nonuniform pressure distributions, caused by transversely nonuniform boiling, would be more likely to occur in a large-core region of PWR size than in the small-core size of the experiments. Transverse flows, resulting from transversely nonuniform pressure distributions, would provide an additional mechanism for frictional dissipation not present in the experiments. Thus, system oscillations in a PWR during reflood might be heavily damped compared to those observed in the experiments.

Additional computations have been performed with the model for the purpose of exploring a variety of different representations for nonuniform boiling in the core. Also, an attempt was made to extend the model by including additional terms in the axial momentum equations that would allow for an additional mechanism for frictional dissipation resulting from the turbulent transfer of momentum between the two subchannels in the simulated core region. This attempt was not successful; the current model with its localized "cross-connect" between subchannels is too idealized to allow inclusion of such additional terms in a reasonable and consistent manner.

This study has now been concluded, slightly behind schedule. The results indicate that the idealized model devised to account for the effects of transverse flows cannot show that frictional dissipation as a result of such flows will cause significant damping of oscillatory flooding behavior. However, it is also noted that the idealizations implicit in the model may be too severe to warrant extrapolation of this result to an actual PWR. Computations based on more inclusive modeling will probably be required. The attempts being made at Battelle-PNL to extend and apply the latest revisions of the computer code COBRA may provide this additional information.

B. Vapor Generation in Flashing Flows (O. C. Jones, Jr., RAS)

1. Introduction

The purpose of this effort is to describe the actual vaporization process during depressurization of a flowing two-phase mixture. Similar to

*Publications referred to in Sec. I of this report are listed starting on page 25.

the beyond-CHF (critical heat flux) and subcooled boiling problems, one additional relationship is required to account for the nonequilibrium partition of energy between the liquid and vapor phases. This problem has features common to both: bulk superheating of the liquid phase due to decompression, similar to the bulk superheating of the vapor phase in BCHF conditions; and possible wall superheating of the boundary layer similar to the subcooled boiling problem and due to energy release from the pipe walls.

2. Bubble Growth: Description of the Current Effort

To obtain a mechanistic solution to the nonequilibrium flashing problem, one must describe the vaporization process during decompression. A search of the existing literature has revealed no applicable work. Thus, the bubble-growth problem was solved where the time-pressure relationship is a variable. To check the solution, several cases were tested where data existed. For the case in which a spherical bubble undergoes constant-property, exponential decompression, the dimensionless bubble radius is found to be

$$R^* = 1 + \frac{2C}{\sqrt{\pi}} \sqrt{\frac{\alpha}{R_0^2\Omega}}\left[(J_{aT} + J_{ap})\sqrt{t^*} - J_{ap}D(\sqrt{t^*})\right], \tag{1}$$

where the bubble radius is normalized with respect to its radius at time zero. The Jakob numbers J_{aT} and J_{ap} are for initial superheat and saturation temperature difference due to decompression, respectively, R_0 is the initial radius, C is the sphericity correction,[2,3] Ω is the inverse time constant of the decompression process, and α is the thermal diffusivity of the liquid. The dimensionless time is $t^* = \Omega t$. Dawson's integral is included in Eq. 1 as $D(\sqrt{t^*})$, where

$$D(u) = e^{-u^2}\int_0^u e^{\zeta^2}\, d\zeta \tag{2}$$

and has been tabulated by Lohmender and Rittsten[4] among others. Dawson's integral has the asymptotic behavior that

$$D(\sqrt{x}) \sim \begin{cases} \sqrt{x} & \text{as } t \to 0 \\ 1/(2\sqrt{x}) & \text{as } t \to \infty. \end{cases} \tag{3}$$

Unlike the thermally dominated, uniform superheat solutions, the growth rate due to depressurization alone is zero at time zero because the potential for growth to occur has not developed. However, at large times, $D(\sqrt{t^*}) \to 0$, and growth is asymptotically similar to the superheat case where $R^* \simeq \sqrt{t^*}$. This is to be expected, because near the end of the exponential decay $p \to p_\infty$, and the problem looks like the previously analyzed case. Recall

that the properties were taken to be constant to obtain Eq. 1, an approximation that may not be valid for large changes in pressure.

Similarly, it is easily shown that when the pressure decay is such that there is a linear decrease in saturation temperature, the bubble growth rate is given as

$$R^* = 1 + \frac{2C}{\sqrt{\pi}} \sqrt{\frac{\alpha}{R_0^2 \Omega}}\, t^{*1/2}\left(\tfrac{2}{3} J_{ap} t^* + J_{aT}\right), \tag{4}$$

where the terms are similar, except that Ω is based on the slope of the temperature time curve, -b, given as $\Omega = b/\Delta T_r$, and ΔT_r is the reference temperature drop used in J_{ap}. The Jakob number J_{aT} again is based on initial superheat existing at the start of bubble growth.

3. Bubble Growth: Discussion

To date, the only data we have found giving bubble growth in decaying pressure fields are those of Hewitt and Parker[5] and of Niino.[6] The former included data where existing vapor bubbles undergoing condensation were suddenly subjected to approximately exponential pressure decay and the growth was followed over 200-250 msec. In this case, the initial superheat is zero so that J_{aT} in Eq. 1 vanishes. It was found that using the sphericity correction factors of Plesset and Zwick[2] or of Forster and Zuber[3] overpredicted the data. On the other hand, taking the sphericity correction factor, C, as being unity, corresponding to the classical solution of Fritz and Ende,[7] gave reasonable results.

These same data were previously analyzed by Theofanous et al.,[8] who numerically evaluated the growth under both equilibrium liquid-vapor interface conditions and nonequilibrium conditions through the use of an evaporation coefficient. A simplified relationship of mass transfer was used based on the Maxwellian distribution for the vapor molecules. Inertia was included through the Rayleigh equation. Theofanous et al. found negligible effect of nonequilibrium for condensation coefficients of 0.1 and 1.0, and predicted nearly linear growth after the first 2 msec by using the actual values of liquid and vapor properties with time in their numerical solution.

In the presently considered case, it is the vapor density that changes most drastically (0.0067 to 0.0046 g/cm^3 over the range of the data). An inexact but partially compensating procedure is to use the instantaneous value of vapor density during evaluation of the bubble growth. The results of such a calculation for the Hewitt-Parker "data" are shown in Fig. I.1.

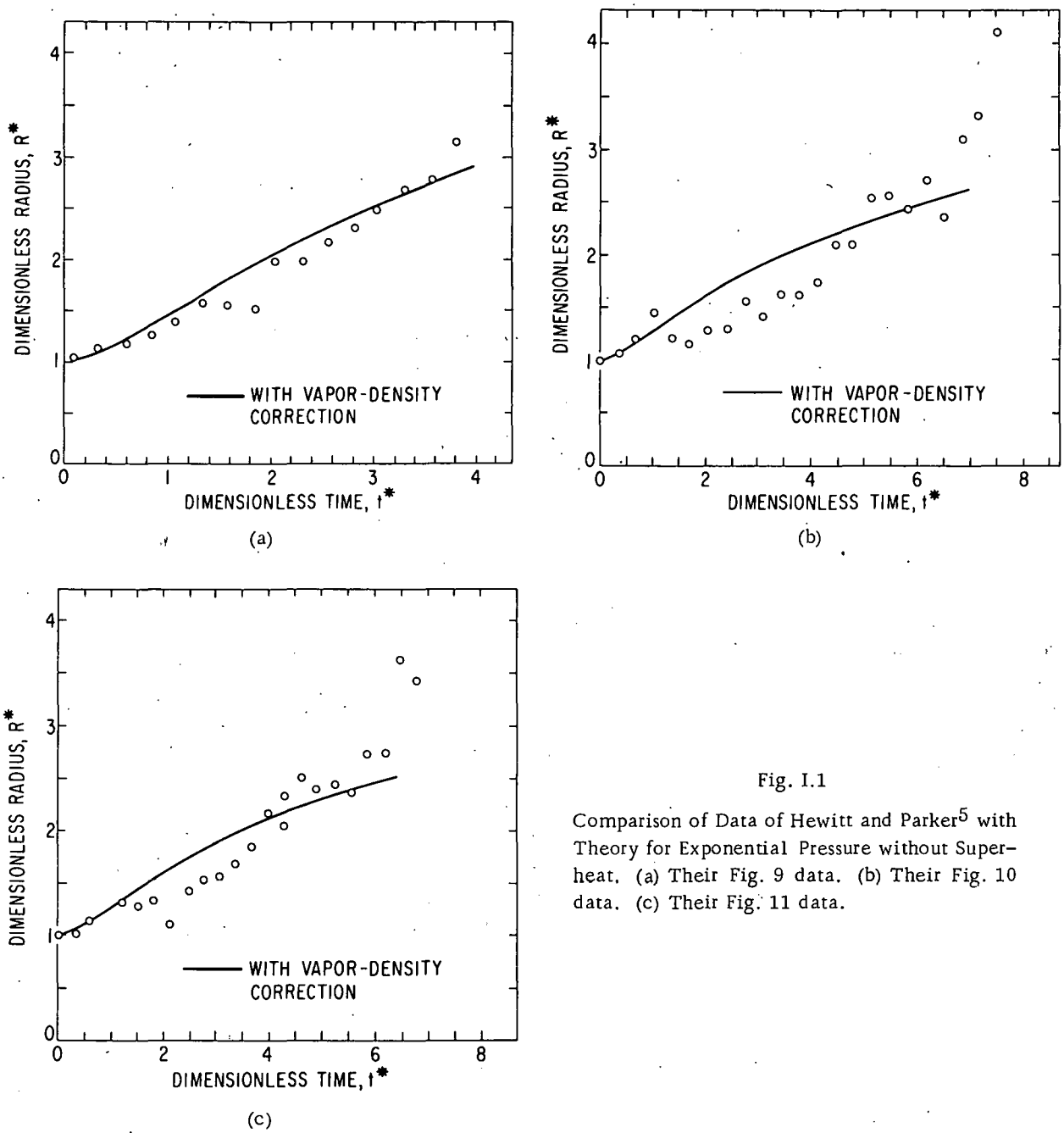

Fig. I.1

Comparison of Data of Hewitt and Parker[5] with Theory for Exponential Pressure without Superheat. (a) Their Fig. 9 data. (b) Their Fig. 10 data. (c) Their Fig. 11 data.

Agreement with the data is quite satisfactory in magnitude, although not so pleasing in trends. In fact, the data are fit quite well by a $t^{*3/2}$ curve in all three cases, indicative of some extraneous effects either not considered in the analysis or inherent in the experiments. Since the bubbles photographed and measured were condensing, and thus decreasing in size, up to the start of the pressure transient, the thermal boundary layer was probably not uniform, but dependent on the past history of the bubble. Also, the measurement times were quite long, up to 0.2 sec, so that gravitational translation of about 1-2 cm could have resulted. If there was any thermal stratification, the net effect could have been similar to uniform bulk heating with the resultant $\sim t^{*3/2}$ power

behavior. As to the possibility that the pressure transients were not really exponential, these were checked at times equal to 0.5, 1.0, 1.5, and 2.0 time constants which spanned the upper 87% of the pressure decay range. The actual time constant in each case was determined and the ranges were: Fig. I.1a (Hewitt and Parker's Fig. 9 data), $27.8 \leq \Omega \leq 31.3$ sec^{-1}; Fig. I.1b (Hewitt and Parker's Fig. 10 data), $40.0 \leq \Omega \leq 43.5$ sec^{-1}; Fig. I.1c (Hewitt and Parker's Fig. 11 data), $35.7 \leq \Omega \leq 38.5$ sec^{-1}. This consistency was fairly indicative of the adequacy of the exponential assumption.

The recent work of Niino[6] described bubble growth induced in pressure-decay systems following laser-pulsed nucleation. Growth thus began from an initially superheated state and continued with data being given over a small fraction (a few milliseconds) of the decay period. The data apparently fall into two categories: those for which the decay is well represented by an exponential, and those not well represented as such. In the former case, decay frequencies at $t^* = 0.5$, 1.0, 1.5, and 2.0 were typically quite constant, such as 350, 350, 342, and 355 sec^{-1}; those not well represented exhibited frequencies that varied significantly, such as 1211, 894, 741, and 654 sec^{-1}. A comparison of Eq. 4 in the former case with Niino's data is shown in Fig. I.2, where the overall time span is about 1.2 msec. Comparison with the data is quite reasonable without the sphericity correction factor. Similarly, in the second case, it was determined that the temperature drop was almost perfectly linear during the bubble-growth period and the representation by Eq. 3 was excellent, including the sphericity correction of Foster and Zuber[3] of $\sqrt{3}$, as seen in Fig. I.3. It is uncertain why the sphericity correction does not seem to apply in exponential pressure decay but does in linear temperature decay. It is also uncertain what effect the laser had in disturbing the thermal boundary layer from the uniform superheat assumed. It might be argued that the local liquid temperature had to be heated close to that required for spontaneous nucleation, which would yield higher growth rates than if the superheat were uniform.

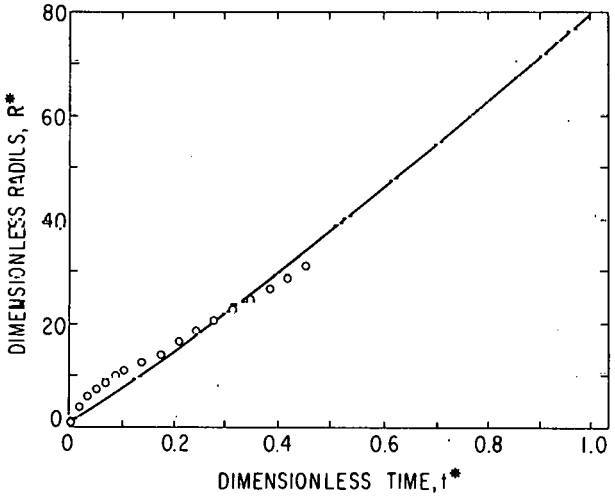

Fig. I.2. Comparison of Data of Niino[6] with Theory for Exponential Pressure Decay with Initial Superheat

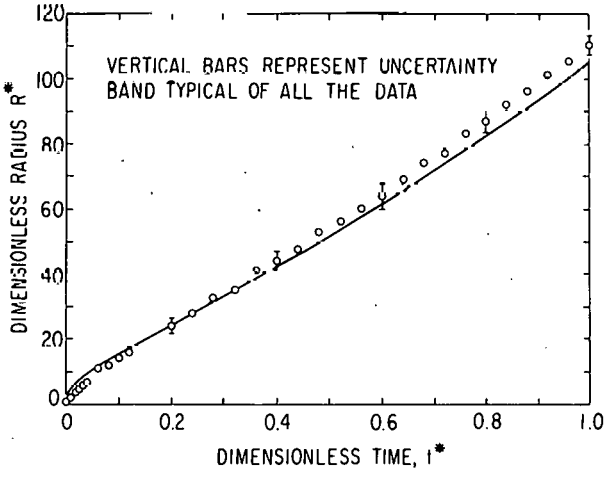

Fig. I.3. Comparison of Data of Niino[6] with Theory for Linear-saturation Temperature Decay and Initial Superheat

4. Vapor Source: Description of the Current Effort

At any location z in a duct, the steady-state quality is given by

$$x = x_0 + \frac{1}{G}\int_{z_0}^{z} \Gamma_V(\zeta)d\zeta, \qquad (5)$$

where $x_0 = x(z_0)$, the initial quality, and $\Gamma_V(z)$ is the local volumetric vapor-generation rate. Data to enable evaluation of Γ_V in flashing flows are virtually nonexistent, as they require detailed measurement of local quality and/or void fraction as well as axial pressure profiles. The data of Reocreaux[9] approach these criteria. Some of these data have been analyzed to determine the variation of Γ_V with location in a straight-diverging round duct. The lead-in to the throat was of 10-mm radius, the divergence section was of 7° total included angle, and the exit section was of 30-mm radius. Detailed void and pressure data were obtained in the vicinity of the throat. The results are shown in Figs. I.4-I.7 for inlet mass velocities of 4180, 6500, 8650, and 10,300 kg/m^2-sec. Calculations were based on unity slip and one-dimensional flow, taking the pressure as the correct indicator for the saturation properties. No expansive cooling was accounted for in the liquid, since in all cases the actual qualities were quite low (<0.0075) where calculations of Γ_V could be made.

5. Vapor Source: Discussion

Equilibrium values of Γ and Γ_E were calculated based on the pressure measurements and, in two cases, are shown in Figs. I.4 and I.5. Generally, these values were considerably larger than the actual values, but exhibit a much larger degree of scatter. The scatter is caused by two successive pressure readings in a small span, giving the same reading and hence giving the same local quality. The result is an equilibrium generation rate that vanishes.

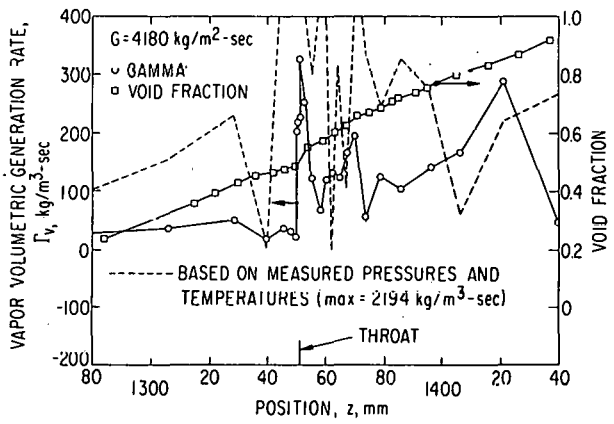

Fig. I.4. Reocreaux[9] Run 403 Data, Including Vapor Volumetric Generation Rates (equilibrium based on measured pressures; nonequilibrium based on measured void fractions) and Void Fraction

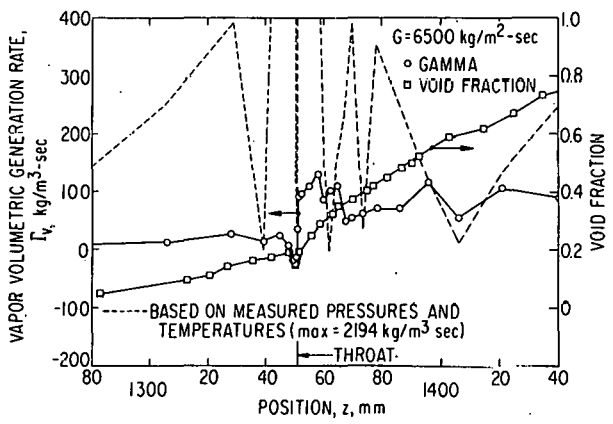

Fig. I.5. Reocreaux[9] Run 400 Data, Including Vapor Volumetric Generation Rates (equilibrium based on measured pressures; nonequilibrium based on measured void fractions) and Void Fraction

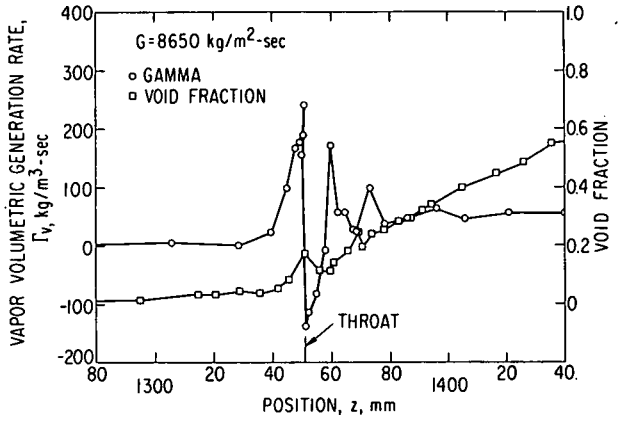

Fig. I.6. Reocreaux[9] Run 405 Data. Including Vapor Volumetric Generation Rates (equilibrium based on measured pressures; nonequilibrium based on measured void fractions) and Void Fraction

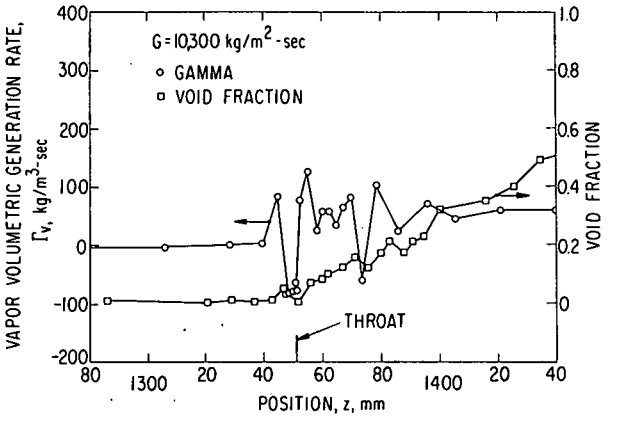

Fig. I.7. Reocreaux[9] Run 408 Data, Including Vapor Volumetric Generation Rates (equilibrium based on measured pressures; nonequilibrium based on measured void fractions) and Void Fraction

Examples include readings of 1.491 bars (Reocreaux's significant digits) at each of two successive locations 2.5 mm apart. The implied resolution is ±0.0005 bar (±1 psf = ±0.2 in. H_2O). This may be compared with a pressure difference of 0.002 bar in 2 mm, yielding an equilibrium-quality difference of 0.00008 for an equilibrium Γ_E of 218 kg/m³-sec. However, these data were obtained on Statham transducers having a minimum full-scale range of 1.75 bars and referenced to atmosphere. The best Statham transducer is rated at 0.5% of full-scale (3.6 in. of water) hysteresis and linearity, although repeatability of a calibrated (Statham) transducer may be better than 0.2% of span. The former would represent an error of over 900 kg/m³-sec, not at all atypical of the order of scatter seen in the Γ_E calculations.

Future comparison of calculations of Γ's from Reocreaux's data may include some degree of smoothing of the data, but this is not clear at this time. For one thing, smoothing may mask real effects such as, possibly, a large increase in Γ_V at the throat. Such an effect was noticeable in all four runs analyzed. It may be noted, however, that although the pressure measurements are the predominant source of error in calculations of Γ_E, they are only used to determine the fluid properties in calculations of Γ_V. In the latter case, the largest errors arise from errors in void measurements.

It appears from the previous discussion that more data are required (1) at higher reduced pressures where qualities are larger, (2) with more accurate pressure measurements, and (3) with more confirmatory measurements to measure actual quality as well as void fraction.

6. Summary

A mechanistic description for nonequilibrium vapor-generation rate in steady, flashing flows has been formulated. This description shows

that one must analyze the vapor-formation process in Lagrangian space. This has been completed and the results applied to bubble growth in decompression processes. Accurate predictions of bubble growth in exponential-pressure-decay and linear-saturation-temperature-decay fields have been demonstrated, validating the approach taken. Recent data of steady-state flashing in a straight-divergent duct have also been examined, and calculation of the non-equilibrium vapor generation rates from these data presented. Significant differences between equilibrium and nonequilibrium generation rates are found, but the data indicate the need for a more accurate and extensive series of tests.

C. One-dimensional Drift-flux Modeling; Vapor-drift Velocity in Annular-flow Regime (M. Ishii and T. C. Chawla, RAS)

1. Notation

A = total flow area per channel

a, b, c = constants defined by Eq. 24

D = hydraulic diameter

f_i = interfacial friction factor

f_{wf} = wall friction factor based on film

g = acceleration of gravity

j_f = liquid volumetric flux, superficial liquid velocity

j_{ftr} = absolute liquid volumetric flux at laminar turbulent transition, defined by Eq. 18

p = pressure

P_i = wetted perimeter of interface

P_{wf} = wall perimeter wetted by film

Re_f = film Reynolds number defined by Eq. 10

t = time

V_{gj} = vapor-drift velocity

v_f = average liquid velocity

v_g = average gas velocity

v_m = mixture center-of-mass velocity

v_r = $v_g - v_f$, relative velocity between phases

z = axial coordinate

α = void fraction of gas phase

Γ_g = vapor-generation rate

$\Delta\rho$ = density difference

δ = average film thickness

ϵ = roughness parameter of interface

μ_f = liquid viscosity

ξ = ratio of the two wetted perimeters given by Eq. 6

ρ_f = liquid density

ρ_g = gas density

ρ_m = mixture density

τ_i = interfacial shear stress

τ_{wf} = wall shear stress

2. Drift-flux Model

In two-phase flows, there is always some relative motion of one phase with respect to the other. Therefore, a two-phase flow problem should be formulated in terms of two velocity fields. According to the degree of the dynamic coupling between the phases, two-phase flow problems can be formulated in terms of a two-fluid model or a drift-flux model.[10,11] The two-fluid model is formulated by considering each phase separately, whereas the drift-flux model is formulated by considering the mixture as a whole. The latter model requires only four field equations: equations of continuity, momentum, and energy for the mixture, and the continuity equation or the diffusion equation for one of the phases.[10]

It is evident that the drift-flux model is simpler than the two-fluid model. However, the former requires some drastic constitutive assumptions, since it has only four field equations in contrast to six field equations in the two-fluid model. It is therefore natural that some of the characteristics of two-phase flow will be lost. The simplification introduced by using only four field equations rather than six makes the use of the drift-flux model an attractive and powerful technique for analyzing a number of engineering problems. In particular, the drift-flux model is useful when the information required is the response of the total mixture and not that of each constituent phase separately. For example, in the dynamic analyses of two-phase flow systems, only the response of the total system is desired.

The four field equations in the drift-flux model are the result of the elimination of one energy and one momentum equation from the original six field equations of the two-fluid model. Therefore, the relative motion and energy difference should be expressed by additional constitutive equations. These two effects inherent to the two-phase flows are taken into account by using a continuity equation for one of the phases and supplementing it with kinematic and phase-change constitutive equations. Thus, by taking a vapor-continuity equation, we have

$$\frac{\partial \alpha \rho_g}{\partial t} + \frac{\partial}{\partial z}(\alpha \rho_g v_m) = \Gamma_g - \frac{\partial}{\partial z}\left(\frac{\alpha \rho_g \rho_f}{\rho_m} V_{gj}\right). \tag{1}$$

The kinematic constitutive equation gives

$$V_{gj} = V_{gj}(\alpha, p, g, v_m, \ldots), \tag{2}$$

and the phase-change constitutive equation gives

$$\Gamma_g = \Gamma_g\left(\alpha, p, v_m, \frac{dp}{dt}, \ldots\right), \tag{3}$$

where V_{gj} is the vapor-drift velocity and Γ_g is the vapor-generation rate.

It may be noted that the vapor-drift velocity in the drift-flux model plays a role similar to that of the diffusion coefficient in a single-phase two-component system. However, the application of a diffusion coefficient is useful only when the relative motion between components or phases is due to a concentration gradient and can be expressed by a linear constitutive law. For general two-phase flow systems, the Fick's law of diffusion may not hold, since in this case the interfacial geometry, the body-force field, and the interfacial momentum transfer are the factors governing the relative motion of phases. In other words, the diffusion of phases in two-phase systems is macroscopic, whereas in single-phase two-component systems it is due to the microscopic molecular diffusion.

It is therefore expected that the constitutive equation for the vapor-drift velocity depends strongly on the two-phase flow regimes, since the momentum transfer between the phases is governed by the geometry of the interfaces as well as by the interfacial area concentration. The constitutive equation for the vapor-drift velocity for bubbly and slug flow regimes has been obtained by Zuber et al.[12] by balancing the gravity force with the drag force. Staub[13] has attempted to obtain the drift velocity for an annular-flow regime. His analysis is based on a linear velocity profile in the liquid film and contains an empirical constant. The linear velocity profile is valid only when the film flow is laminar and the gravitational effect is negligible. It has been demonstrated in our analysis that Staub's empirical constant is actually a function of a void fraction.

The purpose of the study is to present a more general expression for the drift velocity for an annular flow by taking into account the effect of gravity, interfacial shear stress with its dependence on interfacial roughness, and flow regimes in the liquid film.

A particularly important application of the present model is in the area of computer-code developments for thermohydraulic analyses of light-water-reactor transients and accidents, since in this application one of the

dominant flow regimes to be expected is annular flow. Another important application is in accident analyses of liquid-metal fast breeder reactors, for which the most likely flow regime encountered in sodium boiling is also annular flow.

3. Analysis

Inasmuch as the vapor-drift velocity in the drift-flux model is a substitute for one of the phase-momentum equations, a natural starting point for the derivation of the vapor-drift velocity is the momentum equations for two components. Assuming steady-state adiabatic two-phase annular flow with constant single-phase properties, we have the following one-dimensional momentum equations for each phase:

$$-\left(\frac{dp}{dz} + \rho_g g\right) = \frac{\tau_i P_i}{\alpha A} \tag{4}$$

and

$$-\left(\frac{dp}{dz} + \rho_f g\right) = \frac{\tau_{wf} P_{wf}}{A(1 - \alpha)} - \frac{\tau_i P_i}{A(1 - \alpha)}. \tag{5}$$

We define the hydraulic diameter D and the ratio of the wetted perimeters by

$$D \equiv 4A/P_{wf}; \quad \xi = P_i/P_{wf}. \tag{6}$$

Assuming that the film thickness δ is small compared with the hydraulic diameter, we have

$$\frac{4\delta}{D} = (1 - \alpha). \tag{7}$$

We note here that, for an annular flow in a pipe, ξ reduces to $\sqrt{\alpha}$. From the analyses of thin films, the wall shear stress for both laminar and turbulent flows can be given approximately by

$$\tau_{wf} = \frac{f_{wf}\rho_f v_f |v_f|}{2} = \frac{1}{3}\Delta\rho g \delta. \tag{8}$$

Here the gravity-correction term on the right-hand side of Eq. 8, which arises naturally for a laminar film flow, has been assumed to be the same for a turbulent flow as well. The friction factor[14] is then given by

$$f_{wf} = \begin{cases} 16/Re_f & \text{(laminar flow)} \\ 0.0791 Re_f^{-0.25} & \text{(turbulent flow)}, \end{cases} \tag{9}$$

where the film Reynolds number is given by

$$Re_f = \frac{4\rho_f|v_f|\delta}{\mu_f} \simeq \frac{\rho_f|j_f|D}{\mu_f}. \tag{10}$$

Here μ_f is the liquid viscosity and j_f is the liquid volumetric flux; i.e., $j_f = (1 - \alpha)v_f$.

The interfacial shear stress τ_i can be expressed as

$$\tau_i = \frac{f_i \rho_g v_r^2}{2}, \tag{11}$$

where v_r is the relative velocity between the phases. The interfacial friction factor f_i can be given, for example, from Wallis' correlation[15] as

$$f_i = \pm 0.005(1 + \epsilon) \begin{cases} + \text{ for } V_{gj} \geq 0 \\ - \text{ for } V_{gj} < 0, \end{cases} \tag{12}$$

with the roughness parameter given by

$$\epsilon = 300\delta/D \simeq 75(1 - \alpha). \tag{13}$$

By definition, the vapor-drift velocity is related to v_r through

$$V_{gj} = (1 - \alpha)v_r. \tag{14}$$

Eliminating dp/dz between Eqs. 4 and 5, and using Eqs. 6-12 in the resultant equation, we obtain the vapor-drift velocity for a laminar flow in the liquid film:

$$V_{gj}^2 = \frac{16\alpha}{\rho_g f_i \xi}\left[\frac{\mu_f j_f}{D} + \frac{\Delta\rho g D(1 - \alpha)^3}{48}\right]. \tag{15}$$

In contrast to the above expression, the semiempirical correlation of Staub[13] is given by $V_{gj} = 23[\mu_f j_f/(\rho_g D)]^{1/2}$, where the empirical constant 23 has been obtained from a limited number of experimental data. By comparing hio correlation to the present model for a separated flow with a laminar liquid film, we see that the important contribution from the gravity force has been neglected in Ref. 13 and the empirical constant is actually a function of void fraction. For an annular flow in a pipe with $\xi = \sqrt{\alpha}$ and $0.8 < \alpha < 1$, this empirical "constant" varies from 13 to 50. This shows that the Staub's correlation is an overly simplified form of Eq. 15 based only on limited experimental data.

The drift velocity for a separated flow with turbulent film flow is obtained similarly as

$$V_{gj}^2 = \frac{\alpha(1-\alpha)^3 D}{\xi f_i \rho_g}\left[\left(\frac{0.0791}{Re_f^{0.25}}\right)\frac{\rho_f j_f |j_f|}{D(1-\alpha)^3} + \tfrac{1}{3}\Delta\rho g\right]. \tag{16}$$

We note here that V_{gj} takes a negative root of Eq. 15 or 16 if the value of the terms in the square bracket is negative.

A simpler form of Eq. 16 can be obtained by use of a constant turbulent wall-friction factor defined as

$$f_{wf} = \begin{cases} 16/Re_f & \text{if } Re_f \le 3200 \\ 0.005 & \text{if } Re_f > 3200, \end{cases} \tag{17}$$

which was also used by Wallis[15] in his simple annular-flow theory. Then the transition-liquid volumetric flux at the laminar-turbulent transition point is given by

$$j_{ftr} = \frac{3200\mu_f}{\rho_f D}. \tag{18}$$

The vapor-drift velocity for a separated flow with a turbulent film flow becomes

$$V_{gj}^2 = \frac{\alpha}{\xi}\frac{(1-\alpha)^3 D}{f_i \rho_g}\left[\frac{0.005\rho_f j_f |j_f|}{D(1-\alpha)^3} + \tfrac{1}{3}\Delta\rho g\right]. \tag{19}$$

The vapor-drift velocity V_{gj} in the form expressed by Eqs. 15 and 16 or 19 is convenient for use in analyzing steady-state adiabatic or thermal-equilibrium flows, since in these cases the local value of j_f can be easily predicted. However, in a general drift-flux-model formulation, V_{gj} should be expressed in terms of the mixture velocity v_m rather than j_f, as it is the velocity field that is used in the description of the drift-flux model.[12]

From the definitions of mixture velocity, $v_m = [(1-\alpha)\rho_f v_f + \alpha\rho_g v_g]/\rho_m$, and from V_{gj} as given by Eq. 14, the liquid volumetric flux can be expressed in terms of the mixture velocity and the vapor-drift velocity as

$$j_f = (1-\alpha)v_m - \frac{\alpha\rho_g}{\rho_m}V_{gj}. \tag{20}$$

Substituting Eq. 20 into Eq. 15, we obtain for a laminar film

$$V_{gj} = \frac{8\mu_f\alpha^2}{\rho_m D f_i \xi}\left(-1 + \left\{1 + \frac{f_i D\rho_m^2(1-\alpha)\xi}{4\mu_f\alpha^3\rho_g}\left[v_m + \frac{\Delta\rho g D^2(1-\alpha)^2}{48\mu_f}\right]\right\}^{1/2}\right). \tag{21}$$

Thus, in view of Eqs. 18 and 20, the above expression is valid for laminar film flow in concurrent or countercurrent flow situations with V_{gj} in the range

$$\frac{(1-\alpha)\rho_m v_m - \rho_m j_{ftr}}{\alpha\rho_g} \le V_{gj} \le \frac{(1-\alpha)\rho_m v_m + \rho_m j_{ftr}}{\alpha\rho_g}. \tag{22}$$

If we adopt the sign convention such that, for $v_m \ge -\Delta\rho g D^2(1-\alpha)^2/48\mu_f$, f_i has a positive sign, and for $v_m < -\Delta\rho g D^2(1-\alpha)^2/48\mu_f$, f_i has a negative sign, Eq. 21 is simultaneously valid for positive as well as negative values of V_{gj}. The form of the solution of Eq. 21 as a function of v_m keeping α constant is given in Fig. I.8. As can be seen from this figure, V_{gj} for laminar flow is bounded in the range given by Eq. 22. For $V_{gj} \le (1-\alpha)\rho_m v_m/\alpha\rho_g$, the flow is concurrent upward; for $V_{gj} > (1-\alpha)\rho_m v_m/\alpha\rho_g$, the direction of the liquid flow is downward. The case $V_{gj} = 0$ corresponds to the free-falling film without interfacial shear.

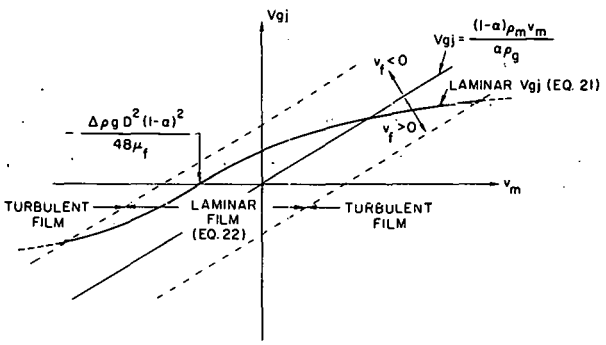

Fig. I.8

Laminar-film V_{gj} at Constant Void Fraction. ANL Neg. No. 900-5767.

To obtain V_{gj} as a function of v_m for turbulent film flow, we substitute Eq. 20 into Eq. 19. Then, by solving for V_{gj} for the case when the upward liquid flow is given by

$$v_m \ge \sqrt{cb^2/a} = \left[\frac{\Delta\rho g D(1-\alpha)^3\alpha^3\rho_g}{3\rho_m^2 f_i \xi}\right]^{1/2},$$

we have

$$V_{gj} = \begin{cases} \dfrac{-bv_m + [av_m^2 + (a - b^2)c]^{1/2}}{(a - b^2)} & \text{if } a - b^2 \neq 0 \\ (v_m^2 + c)/2bv_m & \text{if } a - b^2 = 0. \end{cases} \tag{23}$$

Here we have introduced for convenience

$$\left.\begin{aligned} a &\equiv \frac{f_i \xi \rho_g}{0.005\alpha\rho_f(1-\alpha)^2}; \\ b &\equiv \frac{\alpha\rho_g}{\rho_m(1-\alpha)}; \\ c &\equiv \frac{\Delta\rho g D(1-\alpha)^3}{0.015\rho_f}. \end{aligned}\right\} \tag{24}$$

However, for v_m lying in the range

$$-\sqrt{\frac{\Delta\rho g D(1-\alpha)^3}{0.015\rho_f}} = -\sqrt{c} < v_m < \sqrt{cb^2/a},$$

we have

$$V_{gj} = \frac{-bv_m + [-av_m^2 + (a+b^2)c]^{1/2}}{a+b^2}. \tag{25}$$

Here the lower boundary for v_m corresponds to zero interfacial shear stress, whereas the upper limit is the point of the flow reversal. In the range of v_m given by $v_m \leq -\sqrt{c}$, we have

$$V_{gj} = \frac{-bv_m + [av_m^2 - c(a-b^2)]^{1/2}}{a-b^2}, \tag{26}$$

which applies to the concurrent downward flow.

The above solutions for V_{gj} can be applied only if the following turbulent criterion is satisfied:

$$\left.\begin{aligned} V_{gj} &\leq [(1-\alpha)\rho_m v_m - \rho_m j_{ftr}]/\alpha\rho_g \\ \text{or} \\ V_{gj} &\geq [(1-\alpha)\rho_m v_m + \rho_m j_{ftr}]/\alpha\rho_g \end{aligned}\right\}. \tag{27}$$

The solution of Eqs. 23, 25, and 26 for a fixed value of α is shown in Fig. I.9, where V_{gj} is plotted against v_m. In the figure, the laminar-turbulent

transition occurs at the hyperbolic part of the solution. However, depending on the parameters, it is possible that the elliptic part, Eq. 25, could occur in the turbulent regime, i.e., in the range given by Eq. 27.

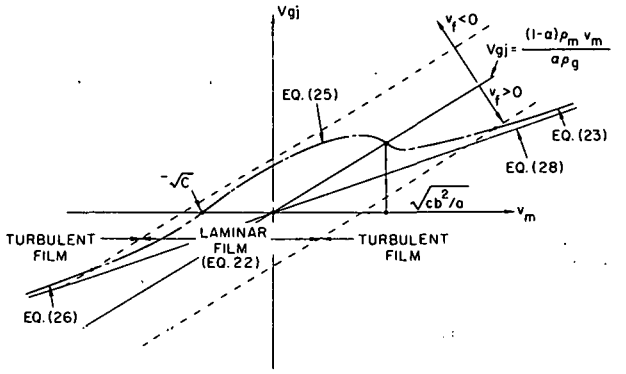

Fig. I.9

Turbulent-film V_{gj} at Constant Void Fraction. ANL Neg. No. 900-5766.

If the absolute value of the mixture velocity is large, such that the flow is essentially concurrent and the gravity effect is small, then the turbulent solution can be approximated by the simple form

$$V_{gj} = \frac{(1 - \alpha)v_m}{\frac{\alpha\rho_g}{\rho_m} + \left\{\frac{\xi\rho_g[1 + 75(1 - \alpha)]}{\alpha\rho_f}\right\}^{1/2}}. \tag{28}$$

As can be seen in Fig. I.9, the expression given by Eq. 28 is an asymptote to the more exact solution given by Eqs. 24 and 26.

Note here that the expression (Eq. 28) for the drift velocity can be transformed to obtain the slip ratio v_g/v_f under the simplifying assumption that the average liquid velocity is much smaller than the vapor velocity. Then we have

$$\frac{v_g}{v_f} = \sqrt{\frac{\rho_f}{\rho_g}}\left[\frac{\sqrt{\alpha}}{1 + 75(1 - \alpha)}\right]^{1/2} \tag{29}$$

for an annular flow in a pipe for which $\xi = \sqrt{\alpha}$. The above expression for slip ratio is similar to that obtained by Fauske,[16] namely, $v_g/v_f = (\rho_f/\rho_g)^{1/2}$, which has no dependence on the void fraction. The factor that takes the void fraction into account in Eq. 29 varies roughly from 0.24 to 1 for the range of α given by $0.8 < \alpha < 1$. Therefore, it is expected that for a turbulent film the Fauske correlation will give reasonably accurate results at high void fractions.

4. Discussion and Comparison with Data

Some experimental data for annular two-phase flow are available in the literature. One of the most extensive and reliable sets of data were obtained at Harwell by G. F. Hewitt and his associates. In particular, those obtained by Gill and Hewitt[17] for upward concurrent flow of air-water mixtures at near-atmospheric pressure in a 3.175-cm-dia acrylic resin tube have been used to verify the present correlation. Since the annular or drop-annular flow regime is confirmed for all the data points by their observations, all their tabulated data (approximately 130 data points) have been used in the present study.

A second set of data used was that of Alia et al.[18] These data were taken in 1.5- and 2.5-cm-dia tubes with water or ethyl alcohol as a liquid phase and argon as a gas phase. The ranges of the gas and liquid flow rates were 15-100 and 20-200 g/cm^2-sec, respectively. The experiments were performed at near-room temperature with system pressures up to 22 kg/cm^2. The total number of the data points was about 300; however, these data were taken at various flow regimes, and unfortunately there were no explicit indications of the flow regimes for any data point. Consequently, we have made flow-regime analyses based on the flow-regime map of Alia et al.[18] as well as the method described by Collier.[19] These analyses show that only a limited number of data occurred for a pure annular-flow regime. About 50 points belong to the churn, slug, or bubbly flow regimes, and another 50 were in the transition region between the slug-type and the annular or drop-annular flow regimes. Thus, only 200 data points belonged to annular or drop-annular flow regimes with moderate to high droplet entrainment. To show that the present model for V_{gj} can also be used for annular flow with moderated entrainment, about half the data for the drop-annular flow regime obtained with lower gas flow rates have been used together with the data for the pure annular-flow regime. Consequently, about 125 data points from Alia et al.[18] have been used in the present study

Another set of data considered were those of Cravarolo et al. obtained under conditions similar to those of Alia et al.[18] In the experiment of Cravarolo, the void fraction was not measured directly, but was deduced from the pressure-drop and wall shear-stress measurements. As explained by Alia et al., this method of obtaining the void fraction is unreliable at high flow rates. Consequently, we eliminated some of the data based on the criteria given by Alia et al. Among the 220 data points of Cravarolo, 180 were clearly in the drop-annular flow regime, based on the given flow-regime map and the flow-regime criteria given by Collier.[19] Among these, about 90 data points have been eliminated because of the uncertainty of the void-fraction prediction at high flow rates and the expected effect of higher entrainment.

The three sets of data considered constitute about 350 data points for annular and drop-annular flow regimes. Figure I.10 compares the experimental data to the theoretical vapor-drift velocities based on the present

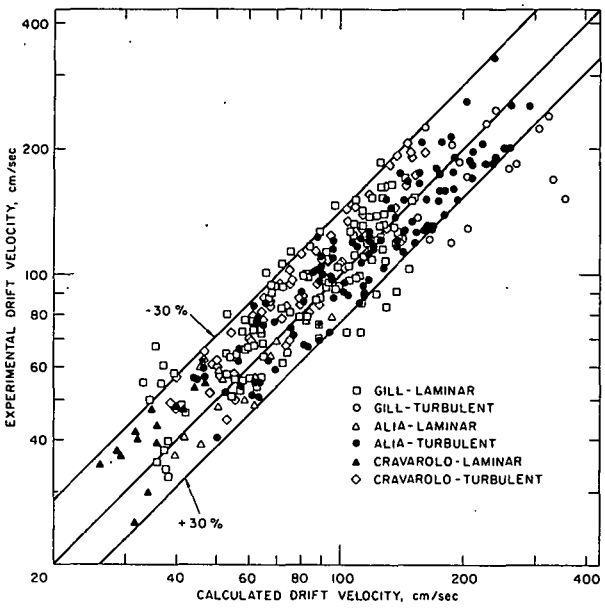

Fig. I.10. Comparison of Theory to Experimental Data. ANL Neg. No. 900-5768.

analysis (Eqs. 15 and 19, which are identical to Eqs. 21, 23, 25, and 26). Theoretical predictions are within about ±30% of the experimental values over a wide range of vapor-drift velocity lying between 20 and 250 cm/sec. A uniform distribution of the data can be attributed to the uncertainty in the determination of void fraction in the above experiments.

We note here that these data include a considerable number of points taken in the drop-annular flow regime at moderate gas-flow rates. This indicates that the present vapor-drift-velocity correlation can be used both for ideal annular flows without entrainment as well as for drop-annular flows with moderate to low entrainment. However, as the amount of liquid entrained in the gas core becomes large at high gas flow rates,[21,22] the measured vapor-drift velocity starts to depart considerably from the predicted values, and the present analysis overpredicts these values. The prediction of V_{gj} in the region where droplet entrainment is sufficiently high is beyond the scope of the present study.

The present constitutive equation for the vapor-drift velocity in an annular flow regime has been obtained from the steady-state and adiabatic formulation. The effects of heat transfer and phase changes on the vapor-drift velocity were considered as secondary. These effects appear only indirectly through the local variables such as the void fraction and the mixture velocity in the drift constitutive equation. It is a common practice to apply constitutive relationships obtained under steady-state conditions to the transient problems, with an assumption that the parameters entering into a constitutive relationship are local variables and are functions of time. Therefore, the application of the present constitutive equation for V_{gj} to a transient two-phase annular flow with a phase change will be consistent with common practice.

D. Transient Critical Heat Flux (J. C. M. Leung, R. E. Henry, and O. C. Jones, RAS)

Two transient-blowdown CHF tests are reported: one short transient (Run 4/22) with a 1-sec inlet-flow stoppage and a long transient (Run 5/29) in which two CHF's were observed.

1. Run 4/22

For Run 4/22, the transient was initiated with solenoid valves SW1 and SW3 closed about 1 sec before SW2 opened. (For the location of the valves, see Fig. I.11.) As a result, the fluid in the test section was stagnant (see flow measurement in Fig. I.12) and the pressure in the system began to rise, as shown in Fig. I.13, until decompression occurred on opening valve SW2. Time zero was taken to be the start of depressurization, and the steady-state conditions are indicated in Fig. I.13.

The heater-wall temperature and the fluid temperature are shown in Fig. I.14. With a 1-sec inlet-flow stoppage before decompression, efficient cooling was maintained during this very low flow period, as indicated by the heater-wall temperature. If the fluid in the heated section remained close to saturation in liquid phase (i.e., no net generation of vapor), the calculated temperature rise of the bulk fluid is about 40°F/sec. The rise in heater-wall temperature was only about 7°F, and if the surface had been dry, a temperature excursion of 80°F/sec was predicted.

The observed pressure rise in the test section resulted in an increase in the T_{sat} value of about 8°F, which is in close agreement with that observed. Countercurrent flow might have existed during this period, as the upper-void probe showed a continuous rise to almost 100% void just before depressurization. Note that complete voiding of the channel would not have occurred, because in this closed system, such a vapor volume would require supercritical pressures.

The start of temperature excursion (critical-heat-flux condition) coincided with the sharp rise in upper-channel void (see Fig. I.15). This phenomenon is in agreement with Run 5/19-A.[23] This upper-channel void measurement indicates that the channel was almost depleted of liquid coolant, and as a result, "dryout" occurred. The above observation tends to support the view that allowable heat flux at low flow can be quite high without experiencing CHF as in pool boiling[24,25] and that flow reversal does not precipitate an instantaneous CHF.

2. Run 5/29

Run 5/29 was performed with the full-size blowdown vessel (blowdown volume* = 0.318 ft^3); the transient lasted almost 1 min. The results are shown in Figs. I.16-I.22.

Two distinct CHF's occurred. The first temperature excursion in Fig. I.17 was observed only at the bottom 8 in. of the heated length, with the most severe rise at the extreme end. Rewetting quickly took place at the

*Blowdown volume is defined to be the system volume between the lower plenum and SW3 valve.

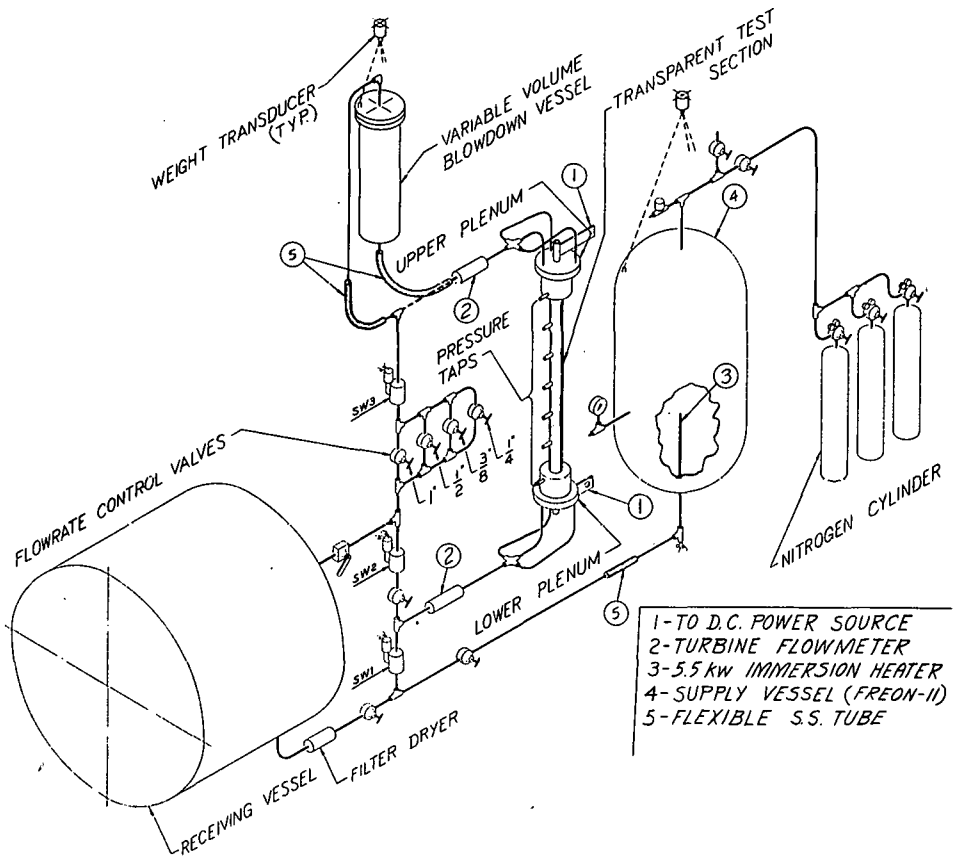

Fig. I.11. Transient-blowdown Critical-heat-flux Test Loop. ANL Neg. No. 900-4557 Rev. 1.

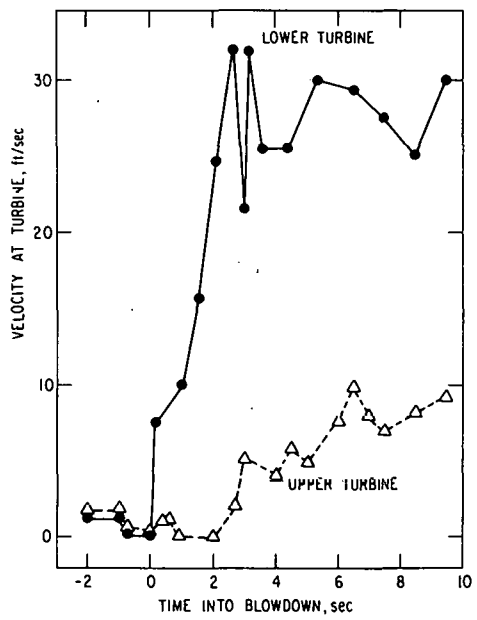

Fig. I.12. Turbine Flow Measurement for Run 4/22. ANL Neg. No. 900-75-339.

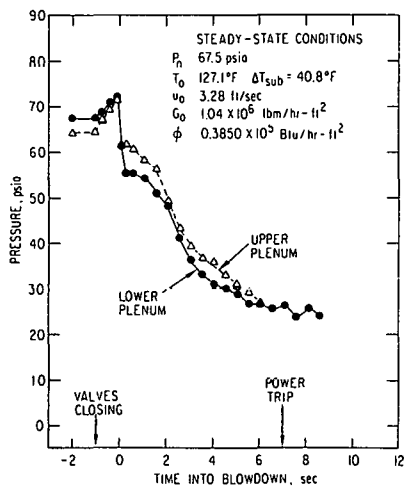

Fig. I.13. Pressure History for Run 4/22. Blowdown volume ≃0.08 ft^3. ANL Neg. No. 900-75-342.

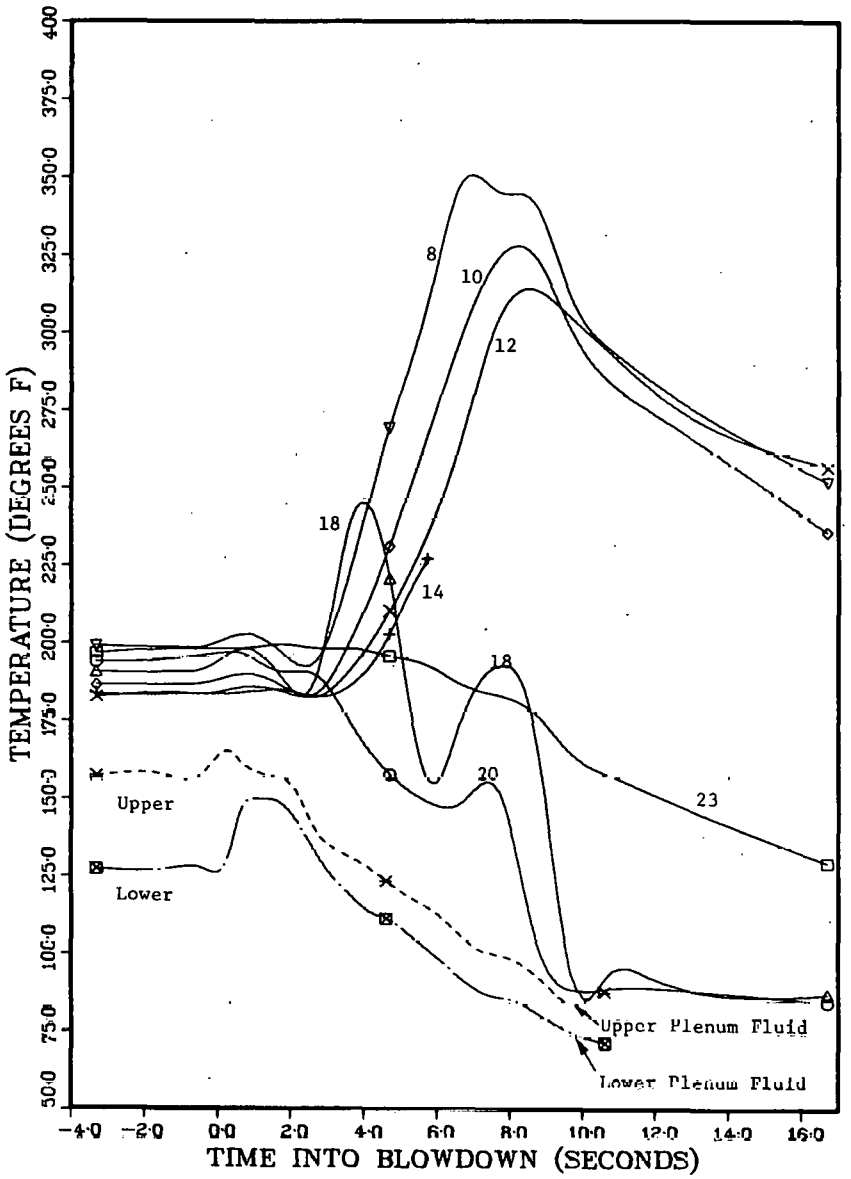

Fig. I.14. Temperature History for Run 4/22. ANL Neg. No. 900-75-346.

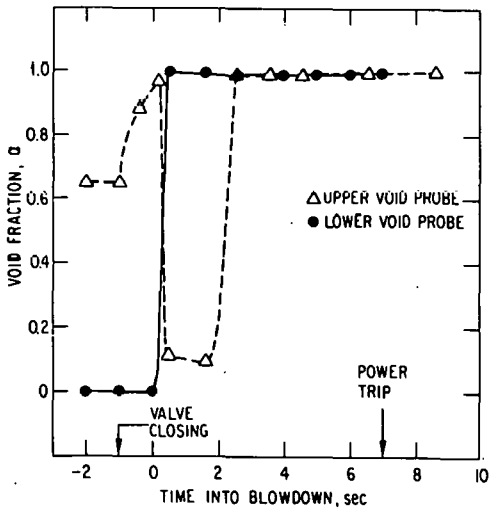

Fig. I.15

Void-fraction Measurement for Run 4/22. ANL Neg. No. 900-75-341.

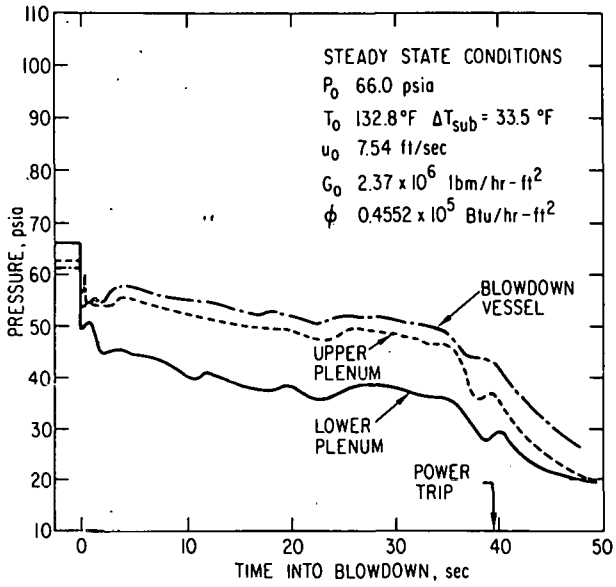

Fig. I.16

Pressure History for Run 5/29. ANL Neg. No. 900-75-417.

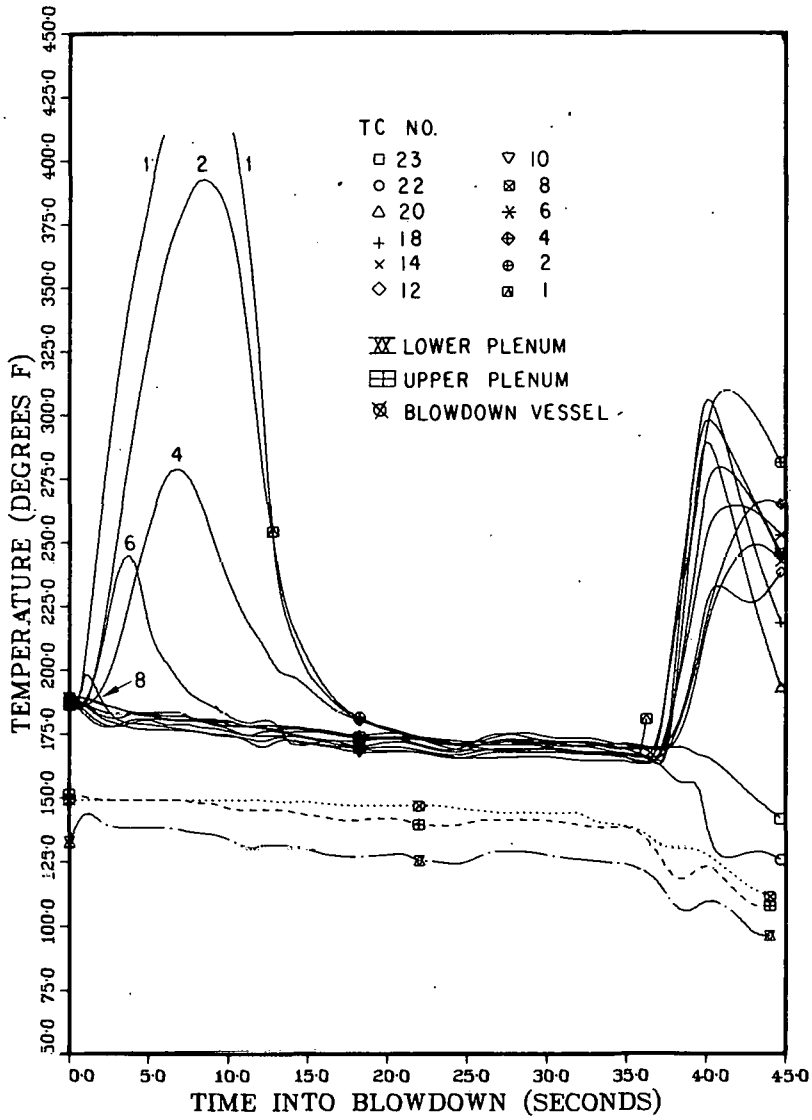

Fig. I.17. Temperature History for Run 5/29. ANL Neg. No. 900-75-412.

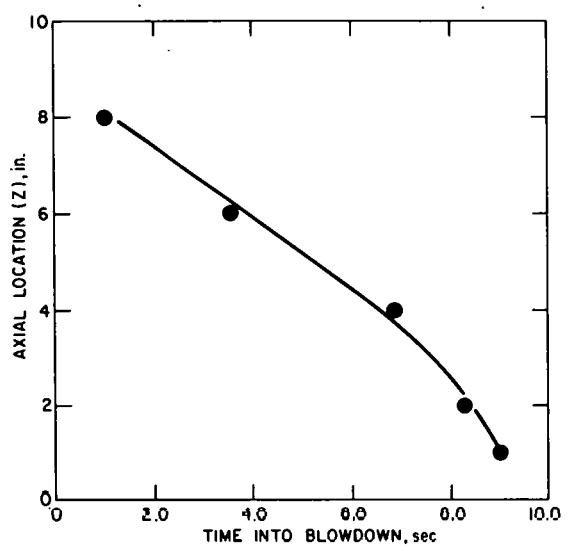

Fig. I.18. Onset of Rewetting during Run 5/29. ANL Neg. No. 900-75-419.

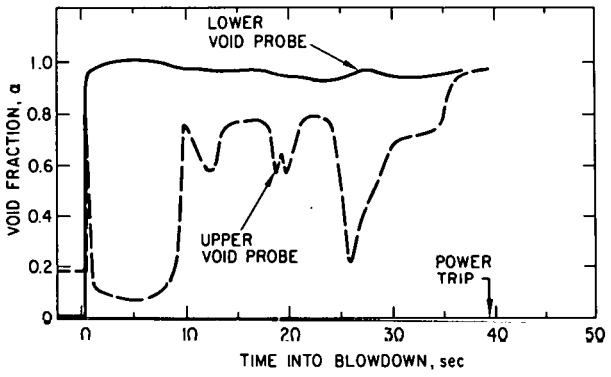

Fig. I.19. Void-fraction Measurement for Run 5/29. ANL Neg. No. 900-75-418.

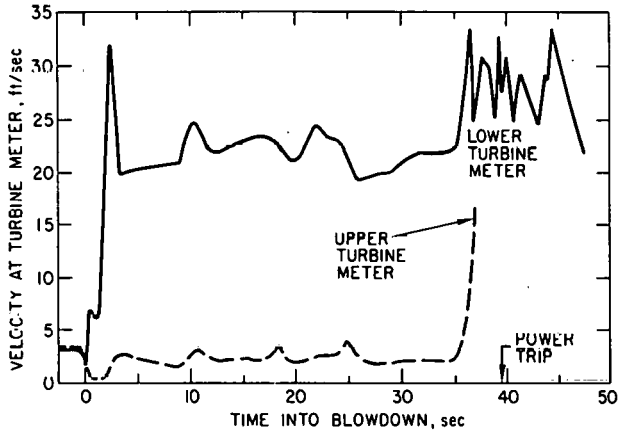

Fig. I.20. Flow Measurement during Blowdown for Run 5/29. ANL Neg. No. 900-75-480.

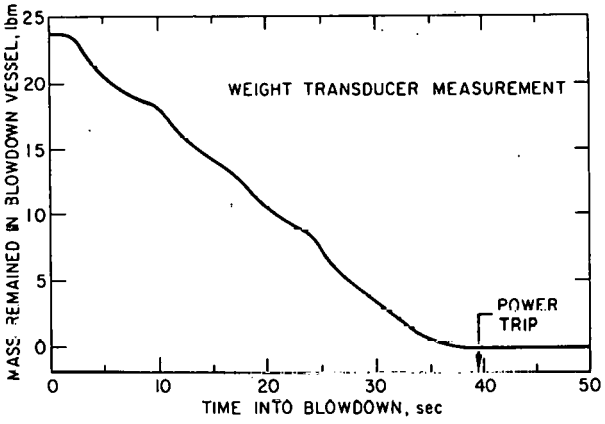

Fig. I.21. Mass in Blowdown Vessel for Run 5/29. ANL Neg. No. 900-75-414.

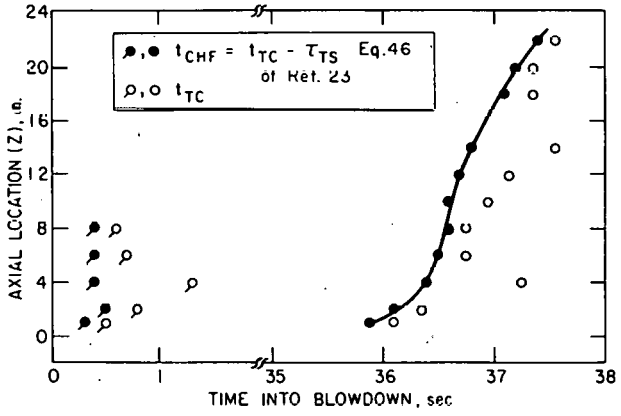

Fig. I.22

Time to CHF vs Axial Location for Run 5/29. ANL Neg. No. 900-75-413 Rev. 1.

8-in. location and propagated downstream, as shown in Fig. I.18. Figure I.19 indicates that the occurrence of the second temperature excursion coincided with the upper-void probe measuring close to 100% void. The upper turbine meter in Fig. I.20 also showed a rapid rise at the same time, indicating high-quality vapor flow. Further, the mass that remained in the blowdown vessel as sensed by the weight transducer was essentially zero. These measurements indicated that the heated channel was depleted of liquid, and as a result "dryout" occurred.

This "dryout" front followed the same kind of locus as in Run 5/19-A,[23] but the rate of propagation was faster. The time to the first CHF was about the same at all CHF locations (400 msec). This suggests that the first CHF occurs by a different mechanism than the second one.

References

1. R. P. Stein, "Analysis of PWR FLECHT-SET Oscillations," Light-water-reactor Safety Research Program: Quarterly Progress Report, April-June 1975, ANL-75-58, p. 2 (Sept 26, 1975).
2. M. S. Plesset and S. A. Zwick, The Growth of Bubbles in Superheated Liquids, J. Appl. Phys. 25, 493 (1954).
3. H. K. Forster and N. Zuber, Growth of a Vapor Bubble in a Superheated Liquid, J. Appl. Phys. 25, 474 (1954)
4. B. Lohmender and S. Riggsten, Table of the Function $y = e^{-x^2} \int_0^x e^{t^2} dt$, Kungl. Fysiogr. Sällsk. i Lund Föhr. 28, 45-52 (1958).
5. H. C. Hewitt and J. D. Parker, Bubble Growth and Collapse in Liquid Nitrogen, J. Heat Trans. 90, 22-26 (1968).
6. Masa-Yuki Niino, Study of a Single Bubble Generation and Growth by a Laser Beam, Ph.D. thesis, University of Tohoku, Japan (1975).
7. W. Fritz and W. Ende, Verdampfungsvorgang anch Kinematographischen and Aufnahmen an Dampfblassen, Phys. Z. 37, 401 (1936).
8. T. Theofanous, L. Biasi, H. S. Isbin, and H. K. Fauske, Theoretical Study on Bubble Growth in Constant and Time-Dependent Pressure Fields, Chem. Eng. Sci. 24, 885-897 (1969).
9. M. Reocreaux, Contribution a l'Etude des Debits Critiques en Enconlement Diphasique Eau-Vapeur, These pour Docteur Es-Sciences Physiques, A l'universite Scientifique et Medicale de Grenoble (Oct 2, 1974).
10. N. Zuber, "Flow Excursions and Oscillations in Boiling, Two-Phase Flow Systems with Heat Addition," Proc. Symp. on Two-Phase Flow Dynamics, Vol. 1, 1071 (1967).
11. M. Ishii, Thermo-Fluid Dynamic Theory of Two-Phase Flow, Chapters IX and X, Eyrolles, Paris, Scientific and Medical Publication of France, N.Y. (1975).

12. N. Zuber, F. W. Staub, G. Bijwaard, and P. G. Kroeger, Steady State and Transient Void Fraction in Two-Phase Flow Systems, General Electric Co. Report GEAP-5417, Vol. 1 (1967).

13. F. W. Staub, Prediction of the Void Fraction in Subcooled Boiling, Annular and Ideal Bubbly Flow, General Electric Co. Report GEAP-5414 (1966).

14. G. F. Hewitt and N. S. Hall-Taylor, Annular Two-Phase Flow, pp. 78-80, Pergamon Press, N.Y. (1970).

15. G. B. Wallis, Annular Two-Phase Flow, Part 1: Simple Theory, J. Basic Eng. 59 (1970).

16. H. Fauske, "Critical Two-Phase, Steam Water Flows," Proc. 1961 Heat Transfer and Fluid Mech. Inst. 78, Stanford University Press, Stanford, Cal. (1962).

17. L. E. Gill and G. F. Hewitt, Further Data on the Upwards Annular Flow of Air-Water Mixtures, UKAEA Report AERE-R3935 (1962).

18. P. Alia, L. Cravarolo, A. Hassid, and E. Pedrocchi, Liquid Volume Fraction in Adiabatic Two-Phase Vertical Upflow-Round Conduit, CISE Report 105, Italy (1965).

19. J. G. Collier, Convective Boiling and Condensation, pp. 14-18, McGraw-Hill, N.Y. (1972).

20. L. Cravarolo, A. Giorgini, A. Hassid, and E. Pedrocchi, A Device for the Measurement of Shear Stress on the Wall of a Conduit; Its Application in the Mean Density Determination in Two-Phase Flow; Shear Stress Data in Two-Phase Adiabatic Vertical Flow, CISE Report 82, Italy (1964).

21. G. B. Wallis, One-Dimensional Two-Phase Flow, pp. 390-393, McGraw-Hill, N.Y. (1969).

22. M. Ishii and M. A. Grolmes, Inception Criteria for Droplet Entrainment in Two-Phase Concurrent Film Flow, AIChE J. 21, 308 (1975).

23. J. C. M. Leung, R. E. Henry, and O. C. Jones, "Transient Critical Heat Flux," Light-water-reactor Safety Research Program: Quarterly Progress Report, April-June 1975, ANL-75-58, p. 27 (Sept 26, 1975).

24. B. S. Shiralkar et al., Transient Critical Heat Flux--Experimental Results, GEAP-13295 (1972).

25. R. A. Smith, Critical Heat Flux in Flow Reversal Transients, Ph.D. thesis, M.E. Dept., MIT (1975).

II. TRANSIENT FUEL RESPONSE AND FISSION-PRODUCT RELEASE PROGRAM

Responsible Group Leaders:
L. A. Neimark and R. B. Poeppel, MSD

Coordinated by:
L. R. Kelman, MSD

Prediction of the behavior of Light-Water Reactor (LWR) fuel rods and fission products under off-normal and accident conditions requires a physically realistic description of fuel swelling and fission-product release that currently does not exist. To satisfy this need, the LWR fuel program at Argonne National Laboratory (ANL) has as its prime objective the development of a comprehensive computer-based model that describes the release of fission products as a function of thermal transients anticipated in hypothetical accident situations. This model will be incorporated into the Fuel-Rod Analysis Program (FRAP) code being developed by the Aerojet Nuclear Company (ANC). The analytical effort is supported by data developed from characterization of irradiated LWR fuel and from out-of-reactor transient heating tests of irradiated LWR fuel under conditions that simulate hypothetical LWR accidents.

The progress during the past year and the status of the program were presented at the Third Water Reactor Safety Information Meeting held at the National Bureau of Standards in Gaithersburg, Md., on September 30, 1975. The following significant advances have been made this quarter in the analytical and experimental efforts of the program:

1. A preliminary version of the LWR Steady-State and Transient (SST) fuel-element behavior code has been verified for steady-state fuel-centerline temperatures.

2. GRASS Steady-state Modification 1 is currently being calibrated and more fully developed for steady-state gas release.

3. A preliminary model has been developed for the behavior of volatile fission products during both steady-state and transient conditions.

4. The hot cell has been equipped to experimentally simulate the thermal conditions anticipated for LWR fuels during hypothetical accidents and to collect the released fission products.

5. Some checkout and scoping tests of the direct-electrical-heating (DEH) equipment have been made using unirradiated UO_2 pellets, and the electronics and the temperature-measuring capability are being improved.

6. A fuel-removal technique has been developed and used successfully to recover two DEH specimens from the Robinson fuel.

7. Fuel-removal equipment and a gas sampling and measuring apparatus are being assembled in and adjacent to the hot cell.

8. Characterization of the Robinson fuel is underway.

Thanks are due Dr. C. Ronchi* for his contribution, during the present quarter, to the development of analytical models and to the characterization of irradiated fuel.

A. Modeling of Fuel-Fission-product Behavior (J. Rest and C. Ronchi, MSD)

1. Modeling of Fission-gas Behavior during Steady-state Conditions

The LWR SST fuel-element code is based on the LIFE analysis for fast-reactor fuel elements,[1,2] discussed in the April-June 1975 quarterly report (ANL-75-58, p. 34), and was generated as an aid to the development and verification of the steady-state GRASS code. A version of SST has been verified for steady-state fuel-centerline temperatures and has been transmitted, upon request, to the Nuclear Regulatory Commission (NRC),[3] where it will be compared with the FRAP code. SST is an interim code, used to obtain operating temperatures for GRASS, and will eventually be replaced by FRAP. At present, SST is not being used to calculate fuel motion, although the code has that capability.

Table II.1 compares SST-calculated centerline-temperature results for four Halden rods with data points obtained from graphs of thermocouple centerline-temperature measurements versus local rod power.[4] Figure II.1 shows SST-calculated centerline-temperature results for two Halden fuel rods with different local rod power histories. To model the radial flux depression, the radial temperature gradient, and the sharp variation in the axial flux shape for these rods, the fuel was divided into six axial fuel sections and one plenum section. Each fuel section was then subdivided into seven radial rings.

Except for the temperature values at 14 h, the SST-calculated centerline temperatures are in good agreement with the experimental results (Table II.1 and Fig. II.1). For a constant power level (rods AA and AE) and a decreasing power level (rods AK and AO) between 14 and 28 h of operation, the measured temperatures show a sizable increase, whereas the calculated temperature values decrease, as would normally be expected. A possible explanation for this behavior is the existence of fabrication processes not modeled by the code (e.g., fuel impurities that are burned off into the fuel-cladding gap, thereby decreasing the gap thermal conductivity). The predicted temperatures for these four rods were found to be highly sensitive to the initial gap size and moderately sensitive to the initial fractional porosity. The initial gap sizes and initial fractional porosities were adjusted within the fabrication uncertainties[4] to give the best agreement with the data.

*Visiting Scientist from EURATOM, European Transuranium Institute, Karlsruhe, Germany.

TABLE II.1. Comparison of SST-calculated Centerline Temperatures with Halden Thermocouple Measurements

Halden Rod	Variables	Time, h								
		14	28	40	43	49	57	67	75	81
AA	Local Rod Power, kW/ft	9.9	9.9	2.5	4.8	4.8	9.7	9.7	2.0	7.0
	Calculated Temp, °C	1539	1485	498	800	788	1499	1459	438	1106
	Thermocouple Temp, °C	1300	1480	563	833	833	1479	1479	458	1104
AE	Local Rod Power, kW/ft	10.3	10.3	2.5	4.8	4.8	10.1	10.1	2.0	7.0
	Calculated Temp, °C	1609	1553	502	810	797	1571	1526	441	1117
	Thermocouple Temp, °C	1300	1490	560	792	792	1495	1495	458	1063
AK	Local Rod Power, kW/ft	14.6	12.8	4.0	6.4	6.4	12.8	12.8	3.0	8.4
	Calculated Temp, °C	2016	1744	640	970	953	1806	1756	522	1232
	Thermocouple Temp, °C	1630	1750	685	917	917	1729	1729	535	1177
AO	Local Rod Power, kW/ft	14.6	12.8	4.0	6.5	6.5	13.3	13.3	3.0	8.4
	Calculated Temp, °C	2044	1772	644	980	964	1895	1844	523	1249
	Thermocouple Temp, °C	1790	1885	685	958	958	1896	1896	542	1213

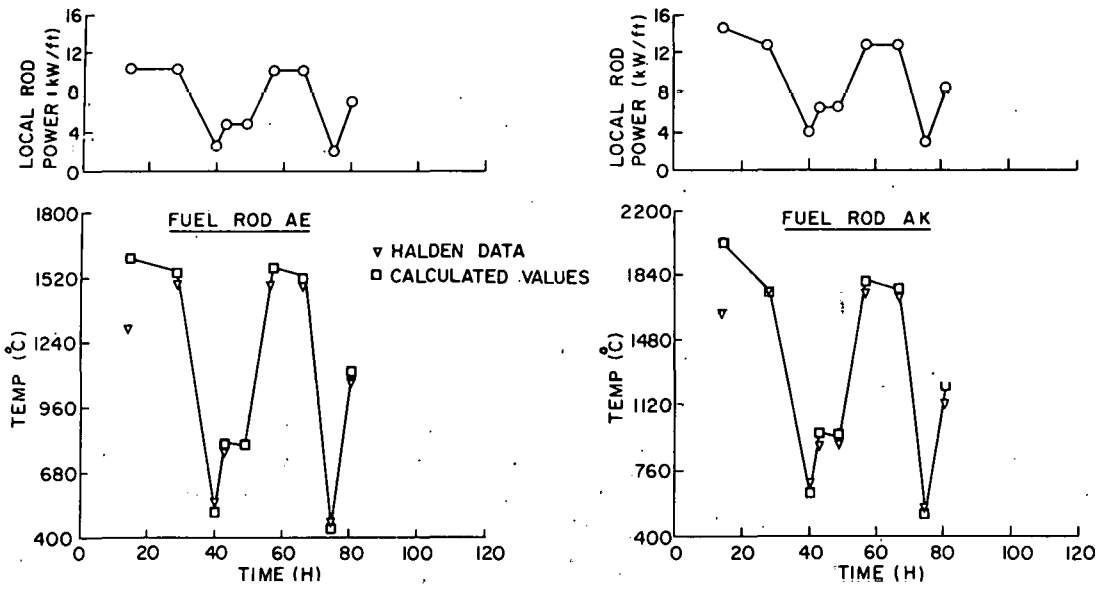

Fig. II.1. Comparison of SST-calculated Centerline Temperatures with Halden Thermocouple Measurements for Two Fuel Rods of Different Local Rod Power Histories. Neg. No. MSD-62080.

GRASS Steady-state Modification 1 [GRASS(SS)-Mod 1] is currently being calibrated for steady-state gas release. The GRASS code[5] does not contain a treatment of interlinked porosity; only after the GRASS code was written was the role of interlinked porosity generally recognized.[6-8] Initial calibration results demonstrate the need for an interlinked-porosity model for fission-gas release and swelling and indicate that the enhanced diffusivities currently used in the GRASS(SS)-Mod 1 code for diffusion of fission gas on grain boundaries are too low. When calibrated to predict gas release for "medium" average-temperature rods, GRASS(SS)-Mod 1 overpredicts the gas release for "higher" average-temperature rods and underpredicts the gas release for "lower" average-temperature rods. The present model multiplies the atomic diffusivity of fission gas in the lattice by a scale factor to obtain the grain-boundary diffusivities; however, this gives an incorrect temperature dependence for diffusion of fission gas on grain boundaries. The activation energy of atomic grain-boundary diffusion is believed to be much less than that for lattice diffusion (about half the lattice activation energy).[9] Results from the "higher" average-temperature rod show that appreciable reduction in the fractional porosity with time occurs in the hotter portions of the fuel. An interlinked-porosity model would predict a reduction in the release of gas from the hotter fuel regions (relative to diffusional release alone) and an increase in fuel swelling due to the buildup of fission gas.

A percolation model of interlinked porosity for fission-gas release and swelling has been developed. In this model, the degree of pore interlinkage along the grain edges is a function of the fractional porosity, the grain size, and the pore size. The pore interlinkage fraction F_∞ is given by

$$F_\infty = \frac{1}{\sqrt{2\pi\sigma}} \int_{P_c=1.57}^{\infty} \exp[-(x - P)^2/2\sigma^2]dx,$$

where

$$P = \tfrac{1}{2} N_p \left\{ 1 + (F^{-1} - 1) \frac{2N_p}{\pi} \frac{1 - \sqrt{1 - \left(\frac{g}{1+g}\right)^2}}{g^3} \right\}^{-1},$$

N_p is the coordination number for a compact arrangement of pores, g is the ratio of grain size to pore size, F is the fractional porosity, and $P_c = 1.57$ is the condition that a chain of interlinked pores connects to the free surface.[10] The width of the probability distribution, σ, can be calculated from the experimental histograms of grain size, pore size, and fractional porosity (see Appendix). The gas released from a section of fuel is given by the amount of gas in the pores, multiplied by F_∞. The remaining gas trapped in the pores, the original amount of gas multiplied by $(1 - F_\infty)$, increases the pore volume according to the equation of state

$$nRT = \frac{4}{3}\pi r_p^3\left(\frac{2\gamma}{r_p} + \sigma_h\right),$$

where n is the moles of gas in the pore, R is the gas constant in ergs/mole-°K, T is temperature in °K, r_p is the radius of the pore in centimeters, γ is the surface energy of UO_2 in ergs, and σ_h is the local hydrostatic pressure in dynes/cm^2. The present GRASS development and calibration work is focused on obtaining more realistic diffusivities for the fission gas, both in the lattice and on grain boundaries, and on including the interlinked-porosity model for fission-gas release and swelling in the code.

Table II.2 lists SST-calculated fractional gas-release results obtained, using subroutine GASOUT, for three CVTR fuel rods; the GASOUT fission-gas release model is a simplified development of diffusion from an athermal spherical body in which the release rate from each fuel ring is given by an Arrhenius function of the average ring temperature. A comparison of the GASOUT-calculated fractional gas-release data with the measured data for the two higher-burnup (also, higher-average-temperature) rods is reasonable. The discrepancy between measured and GASOUT-calculated gas release for the lower-burnup (lower-average-temperature) rod may be due to the lack of a GASOUT model for irradiation-enhanced diffusion that includes fission-gas knockout and recoil; these mechanisms are important up to ~1250°C and can account for as much as 5% of the additional gas release in lower-temperature fuel rods.

TABLE II.2. SST Fractional Gas Release Using GASOUT Option

CVTR Rod Numbers	Maximum Burnup, at. %	Time, h	SST-calculated Gas Release, %	Measured Gas Release, %
13.831	0.92	4872	9.3	10.8
33.833	0.78	3744	9.53	15.0
44.732	0.96	3744	28.13	28.6

Irradiation-enhanced diffusion is included in GRASS-Mod 1. The fission-rate-independent model for irradiation-enhanced diffusion, previously used in the GRASS code, has been replaced by a fission-rate-dependent model based on the experimental work of Hölt and Matzke.[11] The irradiation-enhanced diffusion, D*, is given by

$$D^* = 2.0 \times 10^{-29}\ TFPV \exp(-3161/T),$$

where TFPV is the total fissions per unit volume per second, and T is the absolute temperature in °K. The temperature-dependent term is based on the work of Cornell.[12] The validity of this expression for irradiation-enhanced diffusion will become more apparent as the GRASS(SS)-Mod 1 verification effort proceeds.

2. Modeling of Fission-product Behavior during Transient Conditions

Models have been developed for transient bubble coalescence, the rate of bubble growth after coalescence, and the behavior of volatile fission products during steady-state and transient conditions (see Appendix).

GRASS calculates fission-gas swelling that results from successive coalescence of bubbles. The calculation for the probability of bubble coalescence is based on the capture probability of a diffusing species by a precipitation center and is extended to the case in which the precipitation center is also subjected to Brownian motion. A steady-state solution of the diffusion equation is assumed. This formalism is justifiable for the case in which the concentration of precipitation centers is so low that the effect of the surrounding precipitation centers is negligible or when no large variations in the concentrations of precipitation centers and diffusing species occur during the time step considered. However, for temperature transients in which strong bubble variations occur in a relatively short time, the assumptions are no longer valid. In this case, the GRASS calculation of the bubble-coalescence probability has to be made by taking into account the effect of neighboring precipitation centers on a precipitation center.

For steady-state conditions, instantaneous growth to equilibrium size of coalescing bubbles is a reasonable assumption, considering the relatively long time between coalescences. However, for transient conditions, this assumption will break down if the time for coalescing bubbles to reach equilibrium size is of the order of the time between coalescences. Bubble coalescence is visualized as a two-stage process; the first stage conserves volume--the second stage conserves surface area. The second stage of bubble coalescence results in an increase in bubble volume and, hence, an increase in fuel swelling. This growth stage is physically characterized by a net flow of lattice vacancies through the bubble surface under the driving force of the stress field generated by the nonequilibrium configuration. The rate of growth of noncoalescing bubbles under conditions of changing temperatures and stresses is also controlled by the flux of vacancies through the bubble surface. The vacancy flux is strongly dependent on the vacancy self-diffusivity. Thus, the vacancy self-diffusivity must be determined carefully as a function of temperature and of the local fuel stoichiometry that markedly affects the diffusion coefficient.

The steady-state model for the behavior of volatile fission products is based on the work of Turnbull and Friskney[13] and includes a percolation model of interconnected porosity for fission-product release. According to this model, the diffusion of volatile fission products occurs in two stages: (1) diffusion through the lattice to grain boundaries and (2) rapid diffusion along grain boundaries to grain edges where the volatiles may be released through the interconnected porosity. The rapid grain-boundary diffusion is considered to be important only before the advent of a stabilized network of interconnected porosity venting to the free surface.

The history of a typical volatile fission product found in a nuclear fuel consists of the production of a parent via fission and then the production of a succession of generations via decay until a relatively stable fission product is produced. Given only several precursors, the general solution of the problem is quite complex. Therefore, as a first attempt to predict volatile fission-product release, the effort of the modeling group will concentrate only on fission products with precursors that have short lifetimes compared with the lifetime of the fission product under consideration. In this formalism, the solution consists of solving two coupled equations, one for the concentration of the volatiles in the lattice and the other for the concentration of the volatiles on the grain boundaries.

The solution for the concentration of volatiles in the lattice generates the source term in the equation for the concentration of volatiles on the grain boundaries. The fission products on the grain boundary have two possible mechanisms of release: (1) diffusion along the grain boundary to the outer pellet surface and (2) percolation flow through the porosity channels via vapor or liquid phase. At the end of the steady-state calculation, the following volatile fission-product quantities can be evaluated: the concentration at the grain boundaries, the concentration in solution within the grains, the concentration trapped in closed pores, the amount of volatiles released via percolation, and the amount of volatiles released via grain-boundary diffusion. These results will enable the transient analysis to be initiated with a sufficiently detailed description of the pretransient fuel conditions.

The transient release of volatile fission products is too rapid to be described by long-range diffusional processes. The transient fission-product-release model is based on the theory of viscous flow in a porous medium and includes the effects of evaporation-condensation processes on volatile fission-product behavior. With this model, the observed rapid-transient release of volatile fission products can be qualitatively described.

The equations for the steady-state and transient volatile fission-product models have been derived. The use of these equations to predict the behavior of volatile fission products requires the determination of many physical parameters. The incorporation of these equations into a computer code will require considerable effort. For the steady-state model, parameters such as lattice and grain-boundary diffusivities of the volatiles must be determined as a function of temperature. For the transient model, the critical parameters to be determined are the volatile fission-product viscosities, the heats of vaporization, the ratio of the actual path traveled by the volatile fission-product fluid to the macroscopic permeated distance, and the ratio of the pore volume to the pore specific surface. The development of these volatile fission-product models will be dependent on basic input data from the experimental program, such as the structural modification of the fuel during temperature excursions. However, based on guidance from NRC,[14] additional analytical work on the volatile fission-product models has been postponed for about one year.

ANL received a copy of the FRAP-T code from ANC and has made the necessary modifications to run the code on the ANL IBM-370/195 computer. (ANC has a 360/75 computer.) FRAP-T was run for a sample problem provided by ANC, and the results of the computation agree exactly with the results obtained by ANC. However, to be used on the 370/195 computer, the plotting routine supplied with FRAP-T will entail additional work, and it is not being pursued at this time. The capability to run the FRAP-T computer program at Argonne will enable ANL to assist ANC in the incorporation of the GRASS code system into FRAP.

B. Experimental Technique (M. G. Seitz and L. R. Kelman, MSD)

1. Hot Cell (M. G. Seitz, D. R. Pepalis, W. D. Jackson, and L. R. Kelman, MSD)

The K-1 hot cell in M-Wing of Building 200 (see ANL-75-58, p. 38) has been equipped to serve the experimental effort of the Transient Fuel Response and Fission-product Release Program. The equipment includes a completely enclosed box within the cell for the preparation of fuel specimens for DEH transient testing. The specimen-preparation box has an exhaust to a monitored stack and may be purged with nitrogen gas to reduce the likelihood of fire. A shielded safe has been assembled from lead brick to store fuel in lengths to ~1 m (40 in.). The safe was designed to permit entry into the cell while all the fuel for this program is stored in the safe.

The DEH specimen chamber has been ventilated to prevent the spread of radioactive material when irradiated fuel is being worked with. Air is drawn into the chamber through the open doorway and down through a filter-backed grill below the front of the chamber.

2. Direct-electrical-heating Apparatus (M. G. Seitz, L. R. Kelman, and D. R. Pepalis, MSD, and E. W. Johanson, EL)

Figure II.2 shows the DEH specimen chamber, as positioned at the principal work station of the K-1 hot cell. Operating experience with the DEH specimen chamber and the electronic components described in ANL-75-28 (p. 23) suggested several changes. Completed modifications include electrical insulation of the DEH specimen chamber to prevent arcing and the addition of an extension handle and counterweights as an aid in the use of manipulators to tip the specimen chamber on its side. A 0- to 15-psig gauge has been fitted to the specimen chamber to measure the back pressure during operation. The fission-product collection system was tested by means of a bubble solution and a helium leak detector and was found to be leak-tight to 10-psig helium pressure. The specimen chamber door was modified to improve the tightness of the system.

Installation of heavy electrical cable to the specimen chamber decreased voltage loss to the cable and copper electrodes to only 5 mV/A, resulting in negligible power losses during operation.

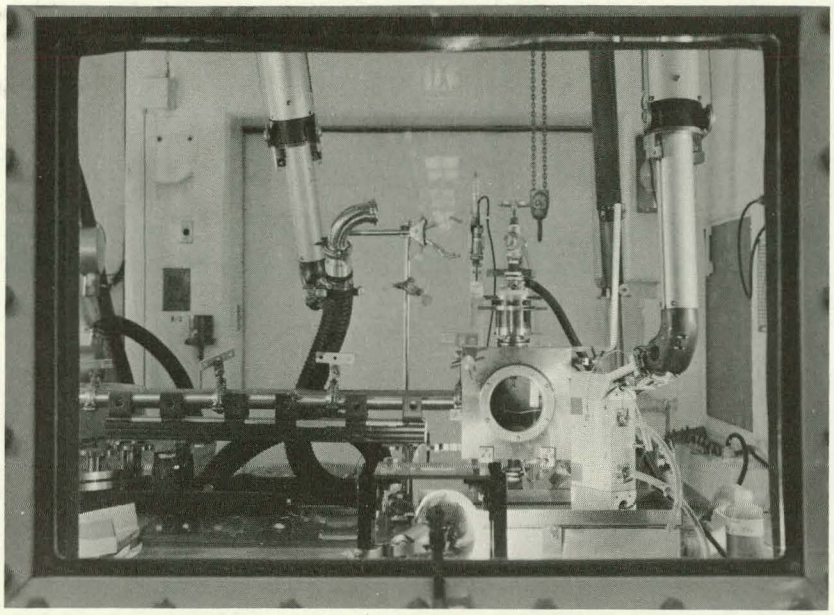

Fig. II.2. DEH Specimen Chamber Positioned at the Principal Work Area of the K-1 Hot Cell. Neg. No. MSD-185768.

An infrared line heater (Research, Inc., Model 5193-5, rated at 100 W/in. at 120 V) with an elliptical reflector was obtained to provide initial heating of the fuel specimens, bake out the bond, and increase the electrical conductivity of the fuel. Tests indicate that the line heater works extremely well at its rated voltage in that centerline temperatures of 400°C are produced in less than 2 h in free-standing UO_2 pellets. The heating rate and temperature are controlled by the applied voltage. The surface temperature, as a function of time, of a 4-cm-long quartz-clad UO_2 pellet stack is shown in Fig. II.3.

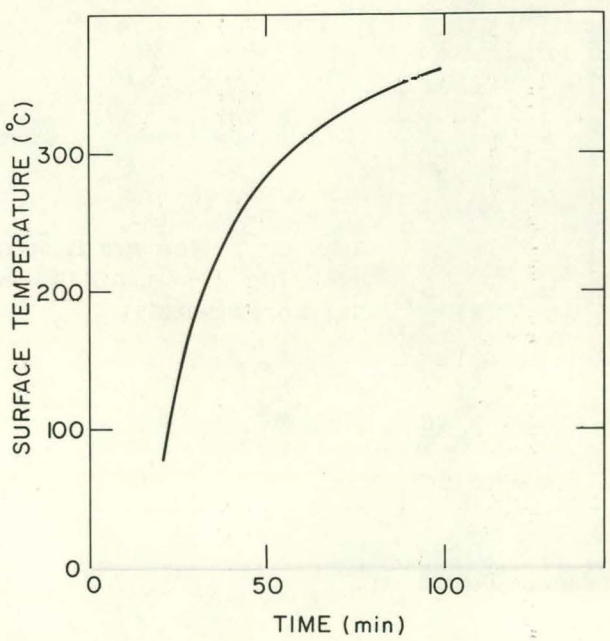

Fig. II.3

Surface Temperature, as a Function of Time, of Quartz-clad UO_2 Pellet Stack with a Lamp Voltage of 128 V. A gradual increase in filament voltage from zero started at time zero. Neg. No. MSD-62087.

Initial heating resulted in a reduction of the resistance of the fuel stack from ~6 x 10^4 to 70 Ω/cm. Because of the decrease in electrical resistance of almost three orders of magnitude, current flow through a 4-cm stack of UO_2 pellets at 40 V was sufficient to increase the temperature of the pellets after the linear heater was removed. This procedure greatly decreased the electrical and thermal shocking of the pellets during heatup.

With the present DEH capability, pellet stacks can be transient-tested to failure (melting or slumping). The DEH tests can be interrupted in a predetermined fraction of time of the transient. Thus, a series of tests using the same input conditions can be run to determine the behavior of fuel and fission products as a function of the time of a specific simulated accident. This interruption capability will be used on a group of fuel specimens with simulated cladding in the initial series of DEH tests.

The DEH power supply is being modified to more accurately indicate the power input to the pellet stack. An analyzer that can measure the root-mean-square values of the current and voltage and average power from complicated waveforms is being introduced into the electronic instrumentation.

3. Correlation between Nuclear and Electrical Heating (M. G. Seitz, J. Moteff,* R. N. Blomquist,** F. E. Savoie, and L. R. Kelman, MSD)

To obtain detailed information on the fuel-temperature profiles that result from direct-electrical heating, experiments were performed using the apparatus shown in Fig. II.4. An insulated Pt-versus-Pt-10% Rh thermocouple was designed to be moved in a hole drilled through the diameter of a

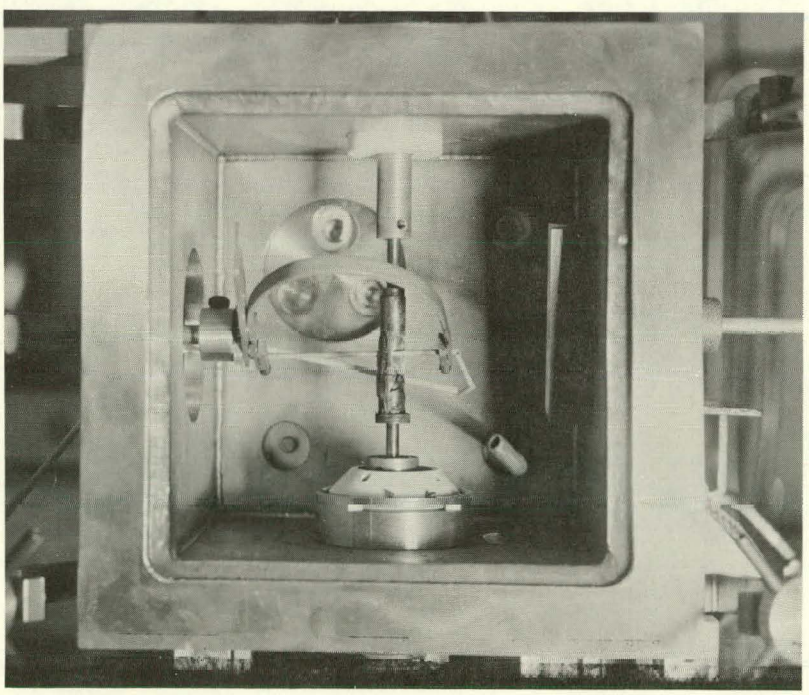

Fig. II.4

Apparatus for Measuring Temperature Profiles of Fuel in DEH Chamber. Neg. No. MSD-185111.

*Participant in the ANL 1975 Summer Undergraduate Research Participation Program.
**Participant in the ANL 1975 Summer Graduate Student Program.

UO_2 pellet. The insulator was clamped into a micrometer-driven translational device and moved back and forth through the pellet. The thermocouple voltage was measured with a potentiometer. Temperature profiles were recorded after steady-state conditions were attained; a profile normally consisted of 40 or more measurements taken in ~4 min. Figure II.5 shows a temperature profile obtained from an uncracked, uniformly heated UO_2 pellet stack under steady-state conditions. The temperature profile depends upon the stack properties, current, voltage, and coolant flow.

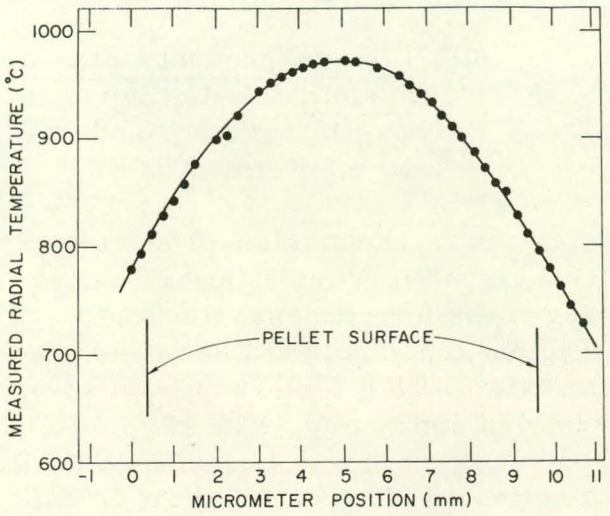

Fig. II.5

Radial Temperature Profile in a Direct Electrically Heated UO_2 Pellet as Measured with a Pt–vs–Pt–10% Rh Thermocouple at Steady-state Conditions. Neg. No. MSD-62081.

Unsymmetric profiles with large, irregular temperature gradients unlike that seen in Fig. II.5 were also obtained. Such behavior could be associated with cracks and hot spots that were visible to the eye.

Profiles of uniformly heated pellets have been obtained to examine the detailed effects of power input and coolant flow on the temperature distribution in UO_2 pellets. These data serve to complement and verify information on temperature profiles as calculated by the Direct Electrical Heating Transient Temperature Distribution (DEHTTD) Code (see ANL-75-58, p. 40) that will be relied upon to predict both steady-state and transient temperature profiles in the irradiated fuel.

A thermocouple to measure the surface temperature of the fuel stack has been incorporated as part of the experimental apparatus. The thermocouple (Chromel versus Alumel) is sealed through the right side of the specimen chamber and can be adjusted to contact the surface of the fuel by spring action. The bead is then bonded to the fuel and insulated from the coolant flow with UO_2 slip. In test runs, this arrangement has been satisfactory.

The high-temperature pyrometer (2000-Series Ircon pyrometer, 1100-2000 and 1500-3000°C ranges) was calibrated through the cell window. The approach used a tungsten-ribbon filament lamp that was calibrated as an optical radiation source. The indicated temperatures were compared to provide a correction curve for absorption through the window, with and without

attenuation by the hot-cell window. This is a fair approximation, since the emissivity of tungsten varies only from 0.441 to 0.390 over the spectral range of the pyrometer (at 1400°K) and from 0.418 to 0.385 over the temperature range from 1200 to 2600°K. Figure II.6 shows the correlation between the lamp calibration temperature and the temperature indicated by the pyrometer with an emissivity setting of 0.1.

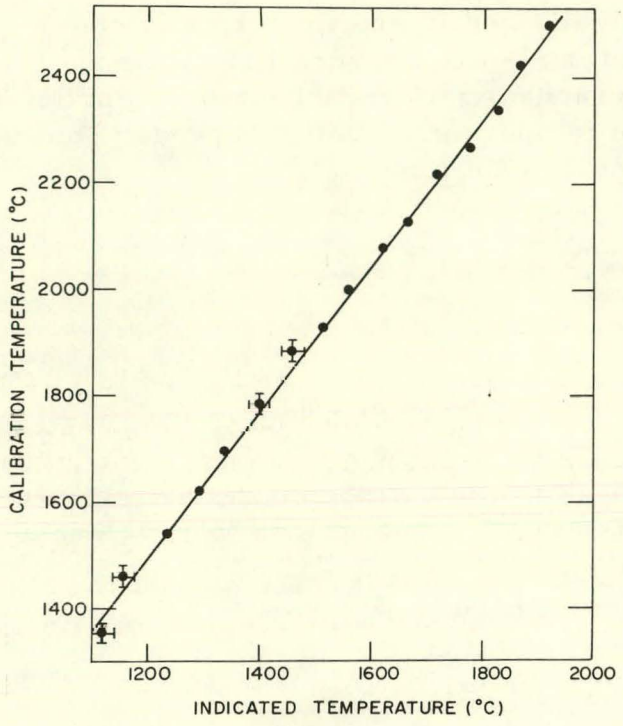

Fig. II.6. Calibration Temperature vs Temperature Indicated on High-temperature Optical Pyrometer as Read through Cell Window. Cell window is 28 in. thick and consists of glass and a zinc bromide solution. The pyrometer was set with an emissivity of 0.1. Neg. No. MSD-62083.

4. Fission-product Collection System (M. G. Seitz, W. D. Jackson, and L. R. Kelman, MSD)

The fission-product collection system, consisting of Ta-Raschig ring traps for condensables and a krypton-xenon cold trap as described in ANL-75-28 (p. 30), has been assembled and tested. The krypton-xenon cold trap was loaded with 0.5 kg of activated charcoal, and the Millipore filter was equipped with a 0.45-μm (HAWP-29300) particulate filter. Figure II.7 shows the back pressure caused by the flow of helium through the total collection system and that caused by only the tantalum traps and Millipore filter.

A blank test for heavy noble gases extracted from 300 ft^3 of helium gas (STP) has been run using the krypton-xenon cold trap. The gases recovered

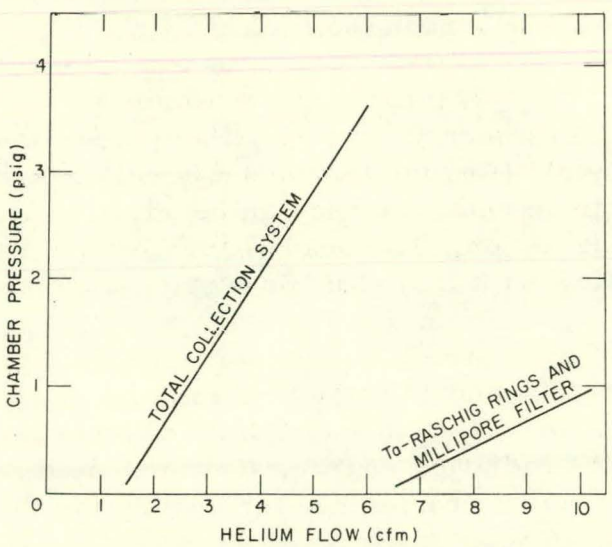

Fig. II.7

Pressure in DEH Specimen Chamber Produced by Flow of Helium through Fission-product Collection System. Neg. No. MSD-62084.

from the trap did not contain a measurable amount of krypton or xenon, indicating that commercially purchased gas may be used without additional purification.

Procurement and fabrication of items for the fission-gas measurement and sampling apparatus have been completed, and assembly and installation of the components are 85% complete. Leak-testing and calibration of the system will follow installation.

5. Recovery of Irradiated Fuel Specimens (S. M. Gehl, D. R. Pepalis, F. E. Savoie, and L. R. Kelman, MSD)

Those details of fuel-rod microstructure that affect fuel-recovery processes were discussed in ANL-75-58 (p. 41). Pertinent microstructural characteristics of the Robinson fuel are shown in Fig. II.8. The fuel exhibits a coarse pattern of cracks, the fuel-cladding gap varies from 0.110 to 0.022 mm (0.0043 to 0.0009 in.), and the fuel does not appear to be bonded to the cladding. In these respects, the Robinson fuel is similar to the MAPI M-12 rod shown in Fig. II.5 of ANL-75-58. The fuel-recovery approach used on the Robinson fuel is based on the slip-impregnation method that was used successfully to extract MAPI fuel pellets.

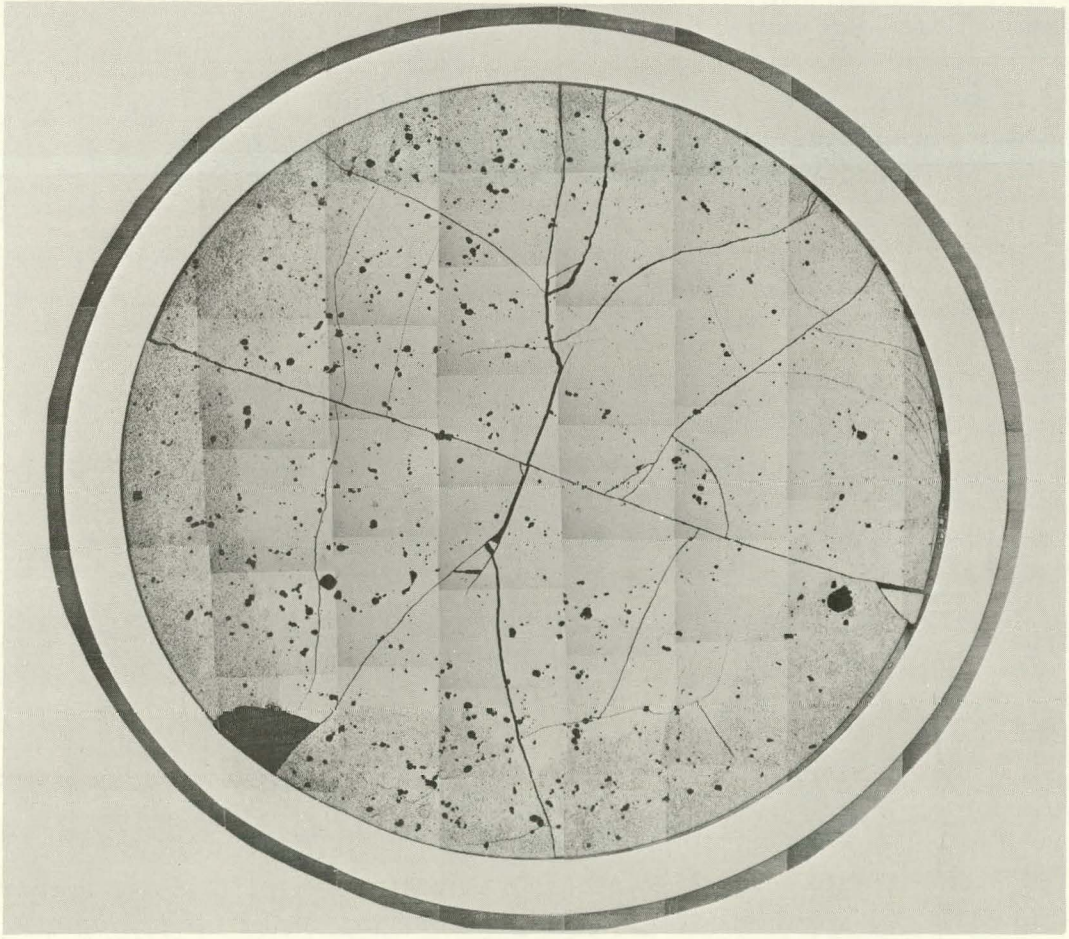

Fig. II.8. As-polished Microstructure of High-burnup Pellet ~35 in. from Bottom of Robinson Fuel Rod F-7. Mag. 12X. Neg. No. MSD-185339.

Two changes were made from the earlier method: The composition of the slip was modified (see Table II.3) to improve pellet strength; and the method of slip impregnation was improved as shown schematically in Fig. II.9. Compression fittings are used to connect one end of a 100- to 150-mm (4- to 6-in.) length of clad fuel to a lever-actuated grease gun and the other end to a vacuum line. The grease gun is used to pump slip into the pellet interfaces and cracks and into the gap between the fuel and cladding. The clad fuel is evacuated before the slip is injected to prevent the occurrence of trapped air bubbles that could expand and drive the slip out of the cracks when the injection pressure is released. The slip-impregnated clad fuel is then cut into 15- to 25-mm (0.6- to 1.0-in.) lengths.

TABLE II.3. UO_2 Slip Compositions

Material	Old Formula	New Formula[a]
0.6-μm depleted UO_2 powder, g	400	400
Ammonium alginate,[b] g	24	20
Hydroxypropyl methylcellulose,[c] g	-	20
Distilled water, ml	250	300
Ammonium hydroxide, drops	15	15

[a]See Ref. 15.
[b]Kelco Superloid.
[c]Dow Methocel F4M.

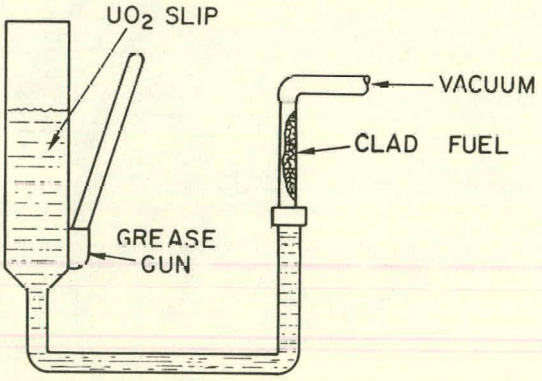

Fig. II.9
Schematic of Slip-impregnation Apparatus. Neg. No. MSD-62086.

The fuel in these pieces is pushed out of the cladding by using an extractor device similar to one developed for LMFBR fuel.[16] To accomplish this, the dimensions of the earlier design were changed to accept LWR fuel, the provision for heating the fuel rod during extraction was not used, and a flat-bottomed quartz tube was designed to receive the extracted fuel.

The quartz tube, shown schematically in Fig. II.10, is loaded with a tungsten disk and a depleted-UO_2 pellet before the fuel is introduced. After the tube is removed from the extractor, a second depleted pellet is placed in

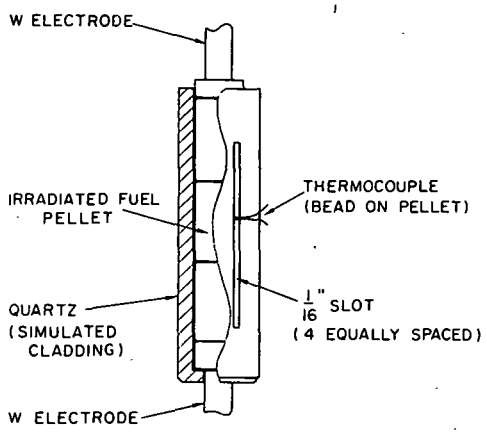

Fig. II.10. Specimen Assembly for DEH Tests on Irradiated LWR Fuel Pellet(s) in Simulated Cladding. Neg. No. MSD-62085.

the tube on top of the fuel. This tube is designed to remain in place as a simulated cladding during transient testing. The slots in the tube allow for the escape of fission gases in a transient, permit the insertion of a thermocouple for surface-temperature measurement, and provide access for the helium coolant gas. The lower-specimen-chamber electrode contacts the pellet stack through a hole in the base of the tube.

With these modifications to the slip-impregnation and fuel-extraction techniques, two lengths of Robinson fuel, each ~20 mm (0.8 in.) long, were successfully recovered from the cladding. These pieces remained intact during manipulator handling and transportation and will be tested in the DEH apparatus. The protection provided by the quartz tube is the primary contribution to the ease with which the specimens could be handled. This technique will be improved to permit more efficient recovery of fuel specimens.

The development of a technique for extracting free-standing pellet stacks is another goal of our continuing fuel-recovery studies. One approach being evaluated is to use a close-fitting split tube to receive fuel in the extractor device. This tube would remain in place to protect the fuel during the handling, transportation, and specimen-chamber loading operations, but would be removed to expose the pellet stack before DEH testing.

C. Fuel Material (L. R. Kelman and S. M. Gehl, MSD)

The three irradiated H. B. Robinson Reactor Unit No. 2 Zircaloy-4-clad UO_2 fuel rods that will be the main fuel for the experimental test and characterization program are described in ANL-75-58 (p. 44) and in Sec. II.D below. The 12 ~0.97-m (38-in.) sections of fuel rod had been cut at Battelle Columbus Laboratories (BCL) from the original three 3.86-m (152-in.)-long rods and shipped to ANL in individual tube containers. The interior surfaces of the shipping cask and cover were found to be somewhat contaminated, and the inside of the secondary (2R) container was extensively contaminated. The nylon caps, used to close the ends of the individual fuel-rod sections, were brittle and cracked; some of the caps had fallen off, and particles of fuel had entered the secondary container. The contaminated condition of the containers has necessitated considerable unanticipated handling of the fuel rods with a resultant delay in the program. All the fuel-rod sections and their containers have been introduced into the Alpha-Gamma Hot-Cell Facility (AGHCF) in Building 212. One of the fuel-rod sections is being used to develop fuel-recovery techniques, to make preliminary DEH test runs, and to characterize

the fuel. The other 11 fuel-rod sections will have to be sealed in clean tubes and transferred to the storage safe in the hot cell where the DEH system is located.

Background information concerning the irradiated Robinson fuel has been sought from personnel in the Nuclear Fuel Division of Westinghouse Electric Corporation-Power Systems (Westinghouse supplied the fuel to the Carolina Power and Light Co.). Westinghouse has been unwilling to release any archive irradiated pellets representative of the Robinson fuel because only a few such pellets exist. They have shown an interest in the fission-product release program and a willingness to exchange technical information. At present, information about the as-fabricated microstructure that is pertinent to the interpretation and evaluation of the characteristics and microstructures of the irradiated fuel has not been obtained.

The BO5 fuel assembly underwent a thermal transient at ANC while the bundle was vertical during removal from the cask.[17] The temperatures attained in the upper half of the fuel rods for the times noted are not likely to have had a significant effect on the distribution or behavior of fission products in the fuel. However, this aspect of the history of the fuel will be considered when the fuel is used in the fission-product release program.

D. Fuel Characterization (S. M. Gehl and L. R. Kelman, MSD)

The fission-gas and volatile fission-product release from LWR fuels during steady-state and transient operations is strongly dependent on the amount and morphology of the fission products and on their distribution with respect to available escape paths from the fuel. Extended networks of interconnected porosity and cracks provide the only effective escape paths during the short times involved in temperature excursions following reactor accidents. The fuel-characterization effort in this program consists of quantitative determinations of the amount and distribution of fission gases, quantitative microstructural analysis, and qualitative determinations of the fission-product distribution. The fuel will be examined before and after DEH-transient testing. The characterization studies provide basic input data and permit verification of the SST fuel-behavior code.

1. Fission-product Characterization (S. M. Gehl, R. N. Blomquist, M. G. Seitz, and D. S. Butler, MSD)

Axial gamma scans for gross fission-product activity and for the ^{137}Cs and ^{106}Rh isotopes have been performed on rod F-7 of the Robinson fuel to determine the relative distribution of these isotopes in the DEH test specimens. Figure II.11 shows the axial profile of average gamma activities of fuel pellets, normalized from the count-rate data of the gross gamma scan. The gross activity profile is nearly flat from 0.8 to 3.0 m (32 to 118 in.), the distances being measured from the bottom of the rod. The activity decreases

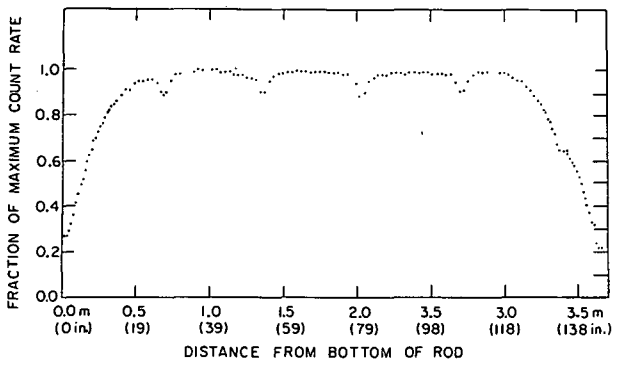

Fig. II.11. Axial Profile of Average-fuel-pellet Gamma Activities from Robinson Fuel Rod F-7 from Assembly B2, Normalized from Gamma-scan Gross Count-rate Data. Neg. No. MSD-62082.

in the upper and lower portions of the rod. The broad depressions are the result of localized low neutron fluxes caused by structural members in the subassembly.

Figure II.12 compares the gross activity trace with traces of ^{137}Cs and ^{106}Rh isotopes for part of rod F-7. Sharp depressions at regular intervals in the gross activity mark the positions of the pellet interfaces. Separation of the pellet fragments gives rise to the irregularly spaced sharp depressions. The isotopic traces show the same features as the gross scan, but exhibit more apparent noise, since the count rates are lower. No evidence for axial redistribution of the volatile fission products has been found in the isotopic traces. Table II.4 lists the observed gamma emission lines and the isotopes they represent.

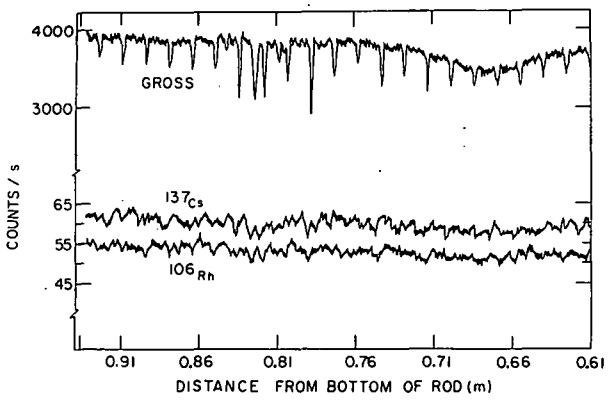

Fig. II.12

Comparison of Gross and Isotopic Activity Traces for Part of Rod-7. ANL Neg. No. MSD-62079.

TABLE II.4. Characteristic Gamma Emission from Robinson Fuel

Energy, MeV	Isotope	Energy, MeV	Isotope
0.097	^{144}Ce	0.765	^{95}Nb
0.113	^{144}Ce	0.796	^{134}Cs
0.134	^{144}Ce	0.871	^{106}Rh
0.513	^{106}Rh	0.985	Unidentified
0.563	^{134}Cs	1.038	^{134}Cs
0.570	^{134}Cs	1.050	^{106}Rh
0.605	^{134}Cs	1.123	^{106}Rh
0.624	^{106}Rh	1.168	^{134}Cs
0.662	^{137}Cs (^{137m}Ba)	1.271	Unidentified
0.695	^{144}Pr	1.365	^{134}Cs (sum)
0.724	^{95}Zr	1.490	^{144}Pr
0.757	^{95}Zr	1.552	^{106}Rh

During the present quarter, we received from ANC[18] axial-flux shape information obtained with the INCORE System near the Robinson fuel assembly; fuel rods from the Robinson assembly are being used in all WRSR-supported safety-related programs on LWR-irradiated fuel. The correlation between our axial gamma-activity profiles and the INCORE neutron-flux measurements is good; the major difference is that the gamma-activity traces have a flatter central plateau.

2. Burnup Analysis (S. M. Gehl, MSD)

Three samples, representing regions of high, intermediate, and low fission-product activity, were cut from rod F-7 and sent to the Analytical Laboratories at ANL-West for ^{148}Nd burnup determination. Results of the analysis are expected by November 1975. These burnup values will be used, along with the axial fission-product activity and neutron-fluence curves, to infer the axial burnup profile in the Robinson fuel. If necessary, the relative radial burnup distribution will be determined by microprobe analysis for neodymium.

3. Microstructural Characterization (S. M. Gehl, C. Ronchi, C. H. Gebo, and L. R. Kelman, MSD)

The initial microstructural characterization of the Robinson fuel consisted of a broad survey of the features of interest. The results presented in this section must be regarded as preliminary, because a small sample of the structure was examined and some of the specimen-preparation and -examination techniques are still under development.

A polished transverse section 35 in. from the bottom of rod F-7 is shown in Fig. II.8. In-reactor densification has occurred in the central portion of the rod. An outer ring, which occupies ~20% of the cross-sectional area, shows higher porosity. The mean grain intercept was ~6 μm in the central region and ~3 μm in the outer ring. The boundary between the high- and low-porosity zones is not a circular trace, but rather a scalloped or cusped outline. The cusps are projections of the densified region along radial cracks. Figure II.13a is a higher-magnification view of one of the cusps. A replica scanning-electron micrograph of the etched surface (Fig. II.13b) shows that the cusped regions have larger grains than the surrounding lower-density area. This restructuring suggests that the fuel temperature was locally higher along the length of the radial cracks.

The radial profiles of pore size and volume fraction cannot be discussed quantitatively at this time because our metallographic technique for this fuel has not been optimized to give a true representation of the polish plane. Inspection of the structure at high magnification reveals that some pull-out has occurred in the unrestructured fine-grained outer ring of the section, but not in the coarse-grained central region; pullout leads to high apparent

pore volume fractions. Replica electron microscopy of fracture surfaces (Figs. II.14 and II.15) has been used to verify that the qualitative conclusions drawn in the preceding paragraphs are valid, in particular that the pore volume fraction is higher in the periphery than in the central region. A quantitative characterization of the porosity is being delayed until the metallographic technique has been improved. Precise immersion-density measurements of the irradiated fuel are being performed to serve as standard values for calibrating the polish.

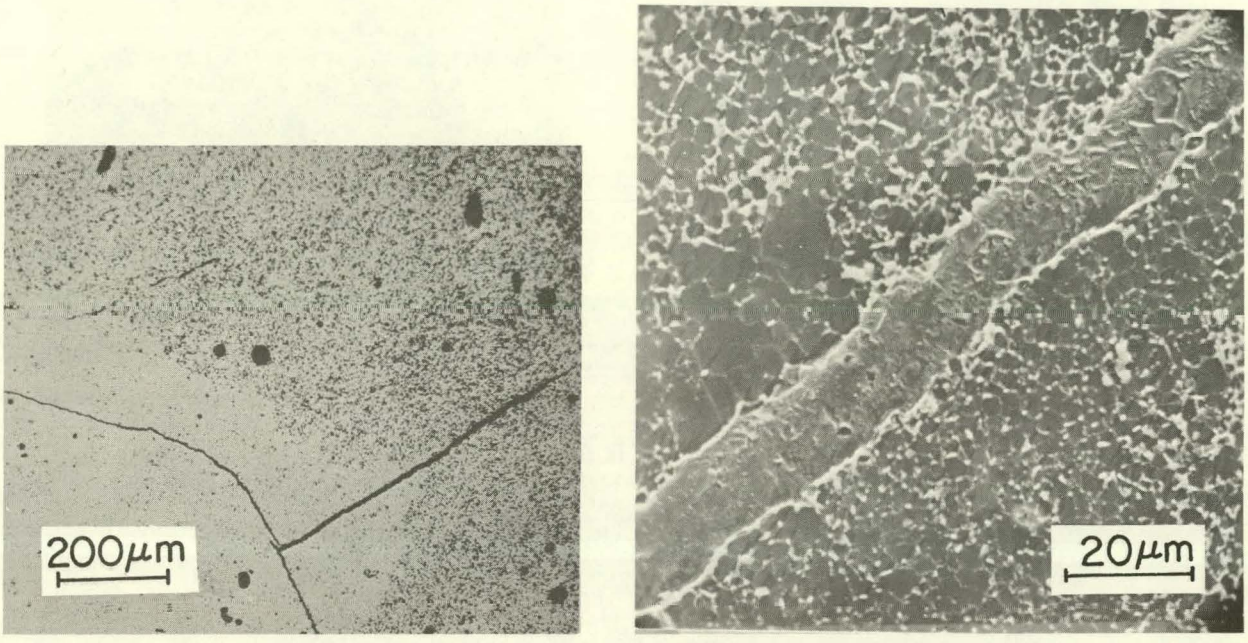

(a) (b)

Fig. II.13. Microstructural Evidence That Cusps Are Projections of Densified Region along Radial Cracks. (a) Cusp-shaped structural zone around crack shown in Fig. II.8. (b) The replica scanning micrograph of the same region magnified reveals that grain growth occurred with marked fuel densification. Neg. Nos. MSD-185590 and -200933.

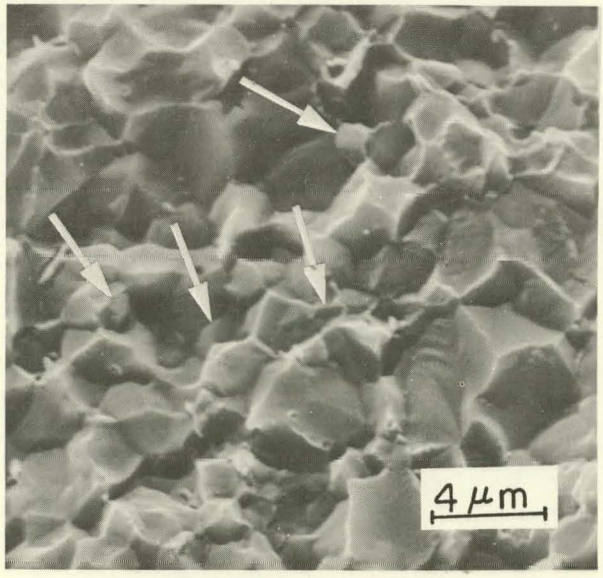

Fig. II.14

Fractograph (SEM Replica) of Outer Fuel Ring Where No In-reactor Densification Occurred. The fracture patterns, predominantly intergranular, show that coarse pores (arrows) are present on the grain boundaries. Neg. No. MSD-200930.

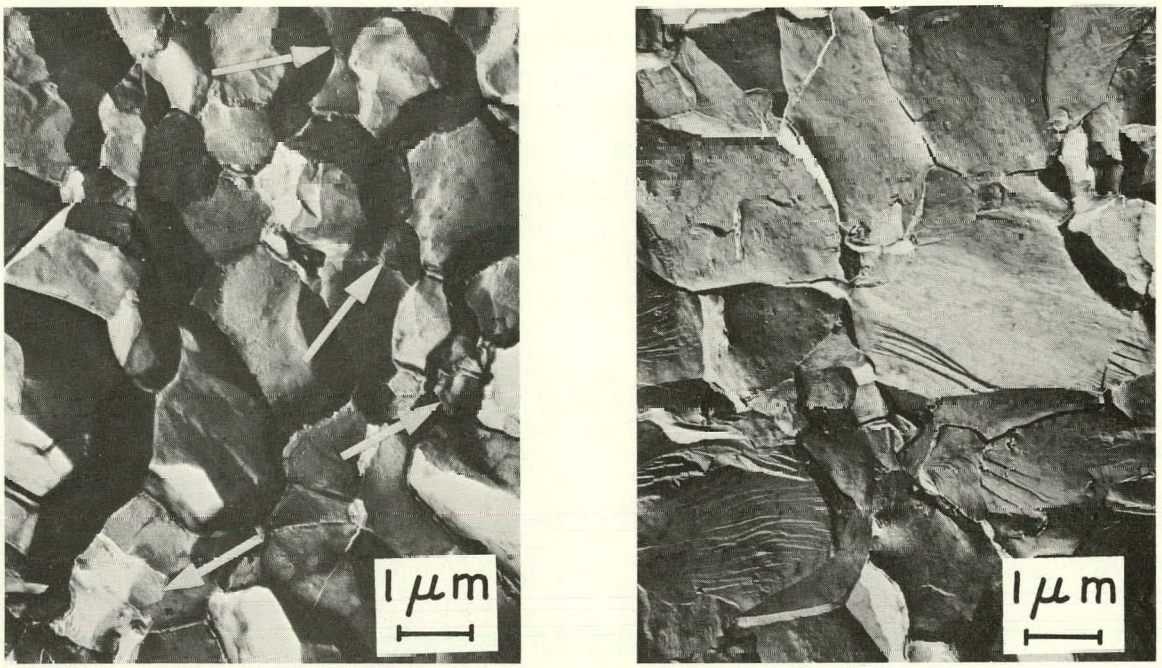

(a) (b)

Fig. II.15. Fracture Surface at Periphery (a) and in Central Zone (b) of Fuel Cross Section (Replica transmission-electron micrographs). The intergranular fracture pattern (a) shows that coarse pores (arrows) are present on the grain boundaries. Neg. Nos. MSD-191702 and -191706.

The crack network in Fig. II.8 is typical of LWR-irradiated fuel. The cracks appear to form a continuous network that subdivides the individual pellets into a number of fragments. This observation is confirmed by the fuel-recovery studies. At one position on the periphery of the fuel, a fragment has been wedged outward. This piece probably is in contact with the cladding at a location not in the plane of polish.

A system of coarse porosity is also visible in the Fig. II.8. These pores range in size from 30 to 250 μm and occupy a volume fraction of ~0.03. Their origin has not been determined; however, they may be the result of pore-former additions during the fabrication of the pellets. The topography of the pore surfaces after etching is shown in Fig. II.16. Each pore shares its boundary with a large number of grains.

The low-burnup microstructure on a section 2 in. from the bottom of rod F-7 (Fig. II.17) shows a gradual decrease in pore volume fraction from edge to center and not the abrupt change observed in Fig. II.8. The cusped effect and the coarse porosity are absent in the low-burnup material. Areas are observed, however, that contain a high pore fraction and small (~10-μm) mean pore intercept. These patches of porosity are about the same size as the pores in the high-burnup microstructure and are distributed with approximately the same spatial frequency. Whether the coarse pores evolved

in some way from the patches or whether either of these features is an artifact of the specimen-preparation technique has not been determined.

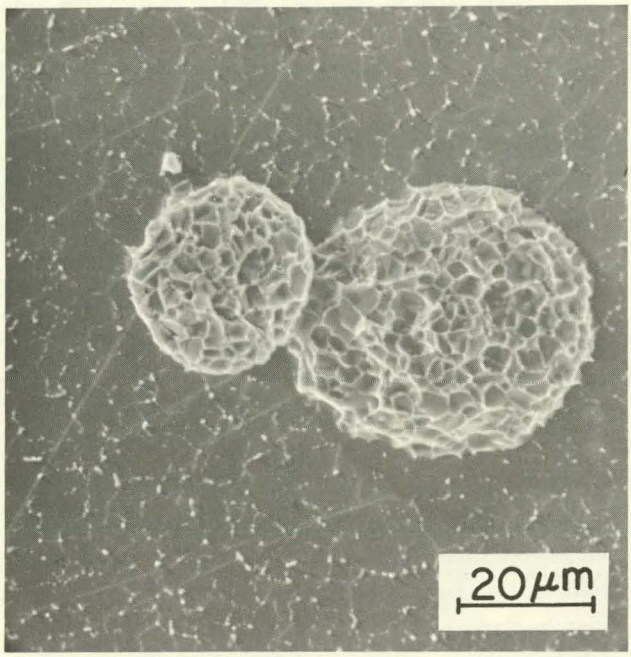

Fig. II.16

Replica Scanning Micrographs of Macropores in Densified Region of Robinson Fuel. Their surfaces visibly extend over a few hundred grains. These features were probably present in the as-fabricated pellets. Neg. No. MSD-200936.

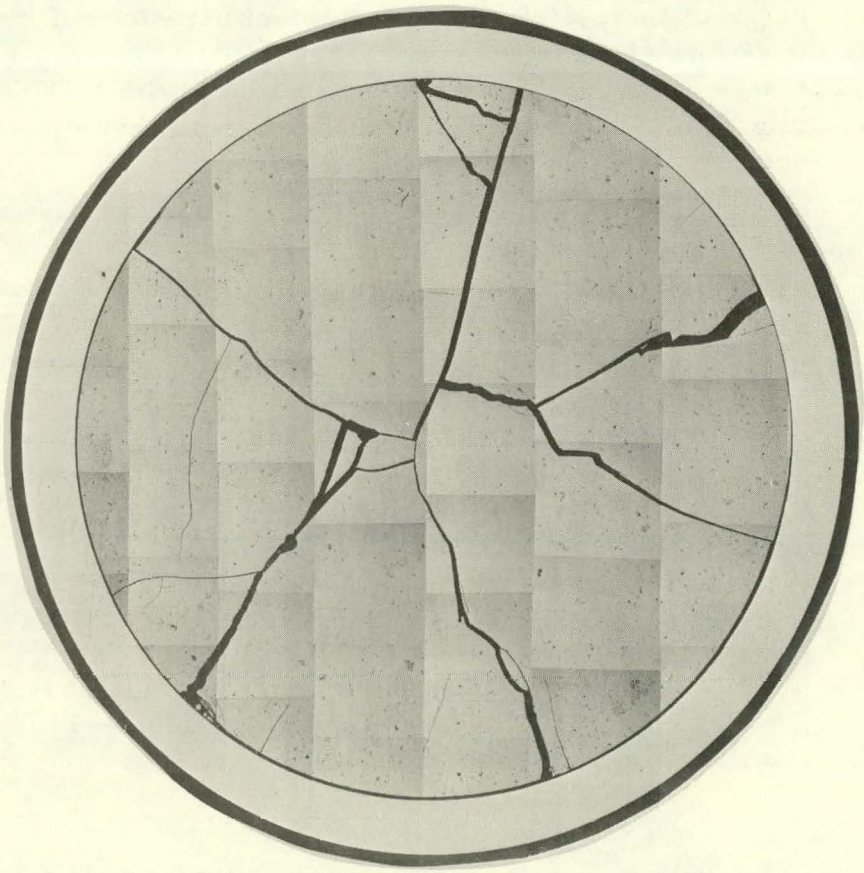

Fig. II.17

As-polished Microstructure of Low-burnup Pellet ~2 in. from Bottom of Robinson Fuel Rod F-7. Mag. 12X. Neg. No. MSD-185586.

Interpretation of many of the details of the irradiated microstructure, including the coarse porosity and the porous patches, depends on our ability to reconstruct the appearance of the corresponding features in fresh (unirradiated) fuel. This process will require considerable effort in the coming months, especially since direct information about the as-fabricated microstructure has not been obtained to date.

Replica electron microscopy of fracture surfaces was also used to study smaller details of the high-burnup microstructure. Fracture surfaces were produced by drawing a vibratory engraving tool across a polished section.[19] Two-stage carbon replicas were prepared using the technique described in Ref. 19, with the following modifications: (a) Germanium was used to shadow the replicas, and (b) the specimen was not rotated during shadowing. Before the plastic layer was dissolved, the replicas were examined in the SEM. A typical microstructure from the porous outer ring is shown in Fig. II.14. The fracture is predominantly intergranular, and several of the intergranular pores intersected by the fracture surface are indicated by arrows.

After the plastic layer was dissolved, the replicas were mounted on copper grids and examined in the transmission-electron microscope. Low-magnification micrographs (Fig. II.15) show that the fracture mode is intergranular in the periphery of the fuel pellet and transgranular in the central region. Evidence of porosity is prevalent in the peripheral region, but not in the center of the pellet. At higher magnifications, fission-gas bubbles are visible on the grain boundaries (Fig. II.18) and in the grain interiors (Fig. II.19). Bubbles as small as 100 Å can be resolved with this replica technique. A rough estimate of the bubble density obtained from these micrographs gives a value

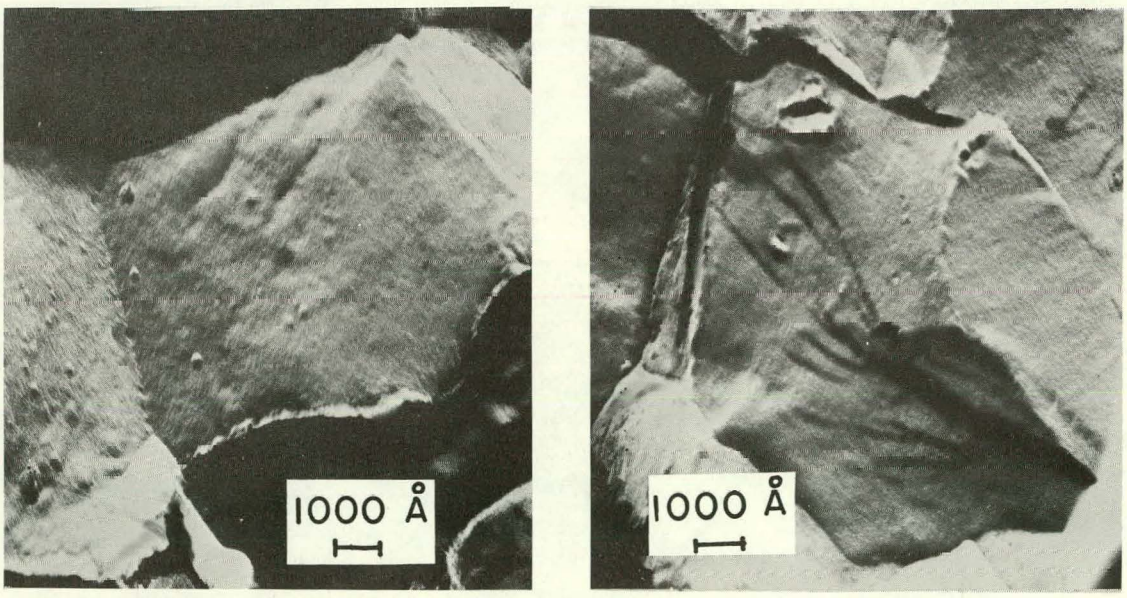

(a) (b)

Fig. II.18. Intergranular Fracture Surface in Periphery of Fuel Showing Fission-gas Bubbles of 100–200-Å Size on Grain Boundaries. Neg. Nos. MSD-191713 and -191718.

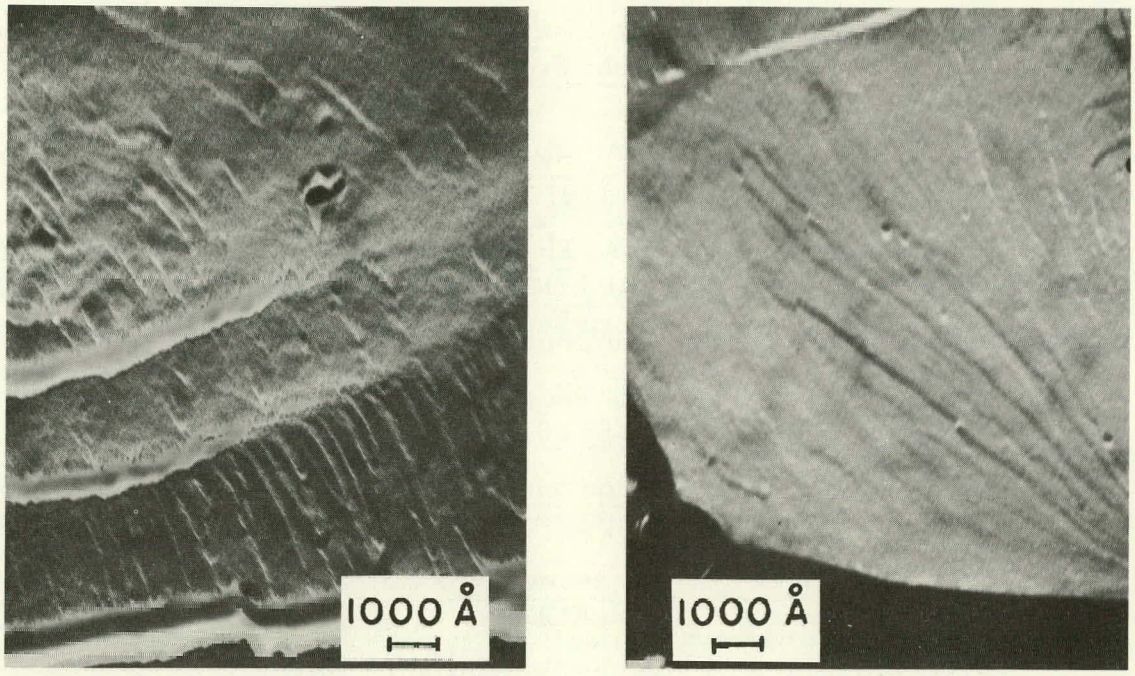

(a) (b)

Fig. II.19. Fission-gas Bubbles of 100–200-Å Size on a Transverse Fracture Surface in the Central Fuel Region (Replica transmission-electron micrographs). Neg. Nos. MSD-191707 and -191714.

of 10^{10} to 10^{11} bubbles/mm^3. This range may actually overestimate the true value, since a fracture surface is a biased estimator of a pore structure. However, the apparent bubble density is typical of steady-state irradiation.

References

1. J. Rest, SST: A Computer Code to Predict Fuel Response and Fission-product Release from Light-water-reactor Fuels during Steady-state and Transient Conditions, to be published in Trans. Am. Nucl. Soc.

2. J. Rest, A User's Guide for the SST LWR Fuel-element Code, unpublished work.

3. J. Rest, ANL, letter to R. DiSalvo, NRC-RSR (Sept 26, 1975).

4. L. T. Laats and P. E. MacDonald, NRC-OECD Halden Project Fuel Behavior Test Program: Experimental Data Report for Test Assemblies IFA-226 and IFA-239, Aerojet Nuclear Corporation ANC (Mar 1975).

5. R. B. Poeppel, "An Advanced Gas Release and Swelling Subroutine," Proc. Conf. on Fast Reactor Fuel Element Technology, Am. Nucl. Soc., Hinsdale, Ill., pp. 311-326 (1971).

6. L. C. Michels and R. B. Poeppel, Influence of Grain Boundaries on Fission Gas Release in Mixed-Oxide Fuels, Trans. Am. Nucl. Soc. 15(1), 199-200 (June 1972).

7. J. A. Turnbull and M. O. Tucker, Swelling in UO_2 under Conditions of Gas Release, Phil. Mag. 30, 47 (1972).

8. W. B. Beeré and G. L. Reynolds, The Morphology and Growth Rate of Interlinked Porosity in Irradiated UO_2, J. Nucl. Mater. 47, 51 (1973).

9. S. J. Rothman, ANL, private communication (Sept 1975).

10. K. Maschke, H. Overhof, and P. Thomas, A Note on Percolation Probabilities, Phys. Stat. Sol. (b) 60, 563 (1973).

11. A. Hölt and H. J. Matzke, Fission-enhanced Self-diffusion of Uranium in UO_2 and UC, J. Nucl. Mater. 48, 157 (1973).

12. R. M. Cornell, An Electron Microscope Examination of Matrix Fission-gas Bubbles in Irradiated Uranium Dioxide, J. Nucl. Mater. 38, 319 (1971).

13. J. A. Turnbull and C. A. Friskney, unpublished work.

14. H. J. C. Kouts, NRC/RES, letter to R. W. Barber, ERDA, FY 1976 Initial RES Program Letter No. 7 for ANL (June 30, 1975).

15. J. T. Dusek, ANL, private communication.

16. J. T. A. Roberts, B. J. Wrona, D. Fischer, and J. A. Buzzell, Observations of Irradiated Fuel Behavior Under Simulated Accident Heating Conditions, Nucl. Tech. 27, 267-272 (Oct 1975).

17. P. E. MacDonald, ANC, letter to L. R. Kelman, ANL (July 30, 1975), transmittal of report Thermal Transients of the Carolina Power and Light Fuel Bundle in Air, KRP-4-75 (July 14, 1975).

18. P. E. MacDonald, ANC, letter to L. R. Kelman, ANL, transmittal of report CPL Assembly B05 Axial Flux Measurements, MacD-66-75 (Sept 11, 1975).

19. L. C. Michels and G. M. Dragel, Preparation of Replicas for Electron Microscopy of Irradiated Ceramic Fuels, ANL-7790 (Apr 1971).

III. MECHANICAL PROPERTIES OF ZIRCALOY CONTAINING OXYGEN

H. M. Chung, A. M. Garde, and T. F. Kassner, MSD

Information is being obtained on the uniaxial and biaxial mechanical properties of oxygen-contaminated Zircaloy to establish a more quantitative cladding-embrittlement criterion applicable to postulated loss-of-coolant-accident (LOCA) situations in light-water reactors. The mechanical-property data for as-received Zircaloy will also contribute baseline information to fuel-element modeling codes.

In the present reporting period, additional data have been obtained on the uniaxial tensile properties of as-received Zircaloy that include the effects of texture and several heat treatments. This information and the microstructural evaluations of the mechanical-test specimens have been used to identify the factors that contribute to superplastic deformation in the material. Initial results on the uniaxial tensile properties of homogeneous Zircaloy-4 alloys with up to ~1.0 wt % oxygen are also reported.

Several rupture tests have been conducted on Zircaloy-4 fuel-clad tubing in the as-received, oxidized-annealed (0.37 wt % oxygen), and oxidized (ZrO_2/α/β composite) conditions to determine the adequacy of the test procedures and the diametral strain-time readout instrumentation. Based upon this work, additional equipment to accomplish the biaxial testing program on oxygen-contaminated Zircaloy fuel cladding will be constructed.

The oxidation and homogenization procedures that are used to produce homogeneous α-Zircaloy mechanical-test specimens are also reported. As a consequence of the Zircaloy-oxygen alloy annealing experiments to produce the mechanical-test specimens, data have been obtained on the diffusion coefficient for oxygen in α-Zircaloy at temperatures of 900-1300°C.

A. Mechanical Properties of As-received Zircaloy-4

1. Uniaxial Strain and SEM Fractograph Results

The effect of temperature and strain rate on the uniform and total strain of Zircaloy-4 was previously reported.[1] Since then, we have conducted additional tensile tests to check and better define the maxima and minima in strain-temperature diagrams. Figure III.1 represents the revised version of strain-temperature plots. Note that, at the three strain rates, a maximum in total strain occurs in the temperature interval 800-850°C, i.e., in the two-phase region near the α-phase boundary, which increases as the strain rate decreases. For a strain rate of 3.3×10^{-4} s^{-1}, failure did not occur after 285% strain and no concentrated neck was observed in the deformed gauge region. The test was terminated because the specimen length exceeded the uniform temperature zone in the furnace. The larger total strains at lower strain rates are consistent

with the well-documented fact that superplasticity is enhanced at slower strain rates. Note that the maxima at 800-850 and at ~1000°C and the minimum at 900-950°C in Fig. III.1 resemble the hoop-strain-versus-temperature data obtained on internally pressurized tubes.[2-5] Although the correlation between uniaxial and biaxial mechanical properties is not simple, the same microstructural factors may be responsible for the strain-temperature behavior in the two cases.

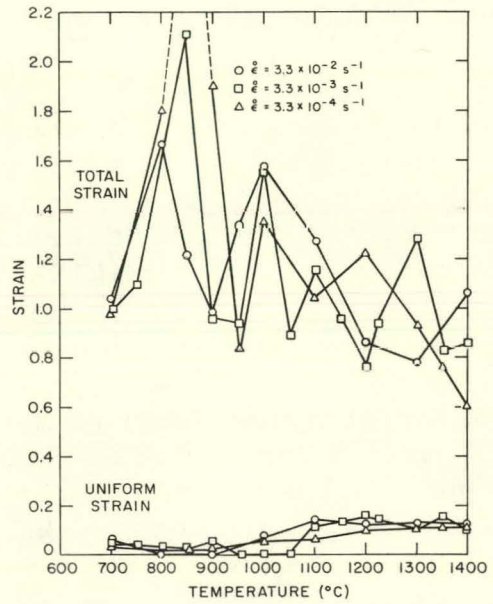

Fig. III.1

Uniform Strain and Total Strain for Zircaloy-4 Specimens as a Function of Deformation Temperature at Three Strain Rates. ANL Neg. No. 306-75-199.

The microstructures of the specimens deformed at 800-850°C were dependent on strain rate. Since the specimens cannot be quenched to room temperature in the Instron furnace, changes in the microstructure during cooling must also be considered. At 800°C and a strain rate of 3.3 x 10^{-2} s^{-1}, the deformed region of the specimen had elongated grains. Recovery and recrystallization are expected to occur above ~800°C, and the elongated shape implies that recrystallization was incomplete. Two factors may be responsible for the elongated grains: (a) the dislocation structure that was produced at this high strain rate, and (b) the short test period that was not sufficient for continuous dynamic recrystallization during deformation. Superplastic deformation is enhanced when recrystallization results in an equiaxed fine-grain structure that is maintained during deformation. Since an equiaxed grain structure was not maintained during deformation at 800°C and $\dot{\epsilon}$ = 3.3 x 10^{-2} s^{-1}, the extent of superplasticity was less pronounced.

At 850°C and $\dot{\epsilon}$ = 3.3 x 10^{-3} s^{-1}, the deformed region exhibited completely recrystallized equiaxed α-grains surrounded by a β film at the grain boundaries; e.g., see Fig. III.21 of Ref. 1. Moreover, the deformed region had a smaller grain size (~7 μm) than the starting material (~11 μm). Because of the fine equiaxed structure, substantial superplasticity occurred at this strain rate. As the strain rate continues to decrease, the extent of superplasticity increases, because the recrystallization rate can keep pace with the slower deformation rate.

Two factors that may aid recovery and recrystallization are an inhomogeneous α phase, due to its comparatively low oxygen diffusion coefficient, and possible sinks for dislocations at the α-β interface. Once new equiaxed α grains are recrystallized, their growth is restricted by the presence of β and χ* phases within the original α grains. The new α grains may deform and recrystallize again during subsequent deformation. Thus, dynamic recrystallization occurs continuously during deformation, and the recrystallized grain size is stabilized and kept fine by the presence of the β and χ phases. Since the χ phase is present at all temperatures below 870°C, the χ phase per se cannot be responsible for superplasticity in Zircaloy.

The above argument requires the presence of β particles within the original α grains before deformation and a β-volume fraction of ~0.1 in the material, since, at smaller volume fraction, most of the β is only at the α-grain boundaries. This explains the observation that the maximum superplastic effect is observed at ~50°C above the α-phase boundary in the two-phase region. As discussed later, the effect of oxygen on the superplasticity in Zircaloy is consistent with this argument.

Scanning-electron-microscopy (SEM) fractographs of specimens fractured at temperatures corresponding to the maxima and minimum in the curves of total elongation versus temperature in Fig. III.1 provide additional insight into the deformation behavior. The SEM fractograph (Fig. III.2) of a specimen fractured at 800°C and a strain rate of 3.3×10^{-2} s^{-1} exhibits tensile dimples characteristic of a ductile failure. A large ductility is evident from the depth of the dimples and the sharpness of the dimple ridges.

Fig. III.2. SEM Fractograph of Zircaloy-4 Specimen Fractured under Superplastic Conditions of 800°C and $\dot{\epsilon} = 3.3 \times 10^{-2}$ s^{-1}. Mag. ~1000X. ANL Neg. No. 306-75-123.

Figure III.3 is a fractograph of a specimen fractured at 950°C and a strain rate of 3.3×10^{-3} s^{-1}. This temperature corresponds to the minimum in the curve of total elongation versus temperature in Fig. III.1. The photograph was taken viewing down on the fracture edge, which is the line joining the two arrows. The fractograph also shows an α particle on the fracture edge that failed in a brittle manner (evidenced by the characteristic river pattern inside the black region), whereas the surrounding β phase failed in a ductile

*The χ phase exists below 870°C[6] and has the approximate composition of 5-9 wt % Fe, 0-2 wt % Cr, 1.5 wt % Sn, and the balance is Zr.[7] As-received Zircaloy in the cold-rolled and the annealed condition contains a small volume fraction of randomly distributed χ-phase particles ~1 μm in size.

manner (manifested by the white tear ridge). Such particles were observed all along the fracture edge. From phase-diagram considerations, the structure of the material at this temperature would consist of a large fraction of β phase with a low oxygen content and a small fraction of α phase containing ~1.5 wt % oxygen. This structure would be equivalent to a distribution of hard particles (α) in a soft matrix (β). When this type of structure is strained, the hard particles would be expected to fail in a brittle manner, which initiates total fracture.

Fig. III.3

SEM Fractograph of Zircaloy-4 Specimen Fractured at 950°C, $\dot{\epsilon} = 3.3 \times 10^{-3}$ s^{-1}. Fracture edge is the line joining the arrows. Mag. 2000X. ANL Neg. No. 306-75-127.

2. Effect of Hold Time before Deformation on Tensile Elongation in Zircaloy-4

The experimental procedures for determining the tensile properties of Zircaloy in the present program involve a short (10-min) hold time at the various test temperatures before the test was started. Figure III.4 shows the effect of increasing the hold time from 10 to 120 min before deformation on the total elongation of Zircaloy-4 specimens for temperatures between 850 and 1000°C. The additional hold time does not have a significant effect on the total strain at 900 and 950°C; however, the strain decreased considerably at 850 and 1000°C. The decrease in the total elongation at 1000°C is probably due to the grain coarsening that becomes significant at this temperature. At 900 and 950°C, grain growth becomes less important, and the deformation behavior is not influenced by the longer hold time. The SEM fractograph (Fig. III.5) of the sample fractured at 950°C after a 2-h hold time is similar to Fig. III.3 for the same temperature and strain rate, except for the shorter hold time. The line joining the arrows represents the fracture edge, which contains two broken α-phase particles.

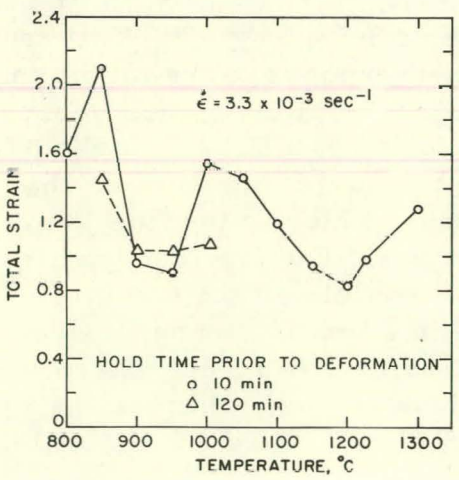

Fig. III.4. Effect of Hold Time before Deformation on Total Strain of Zircaloy-4. ANL Neg. No. 306-75-200.

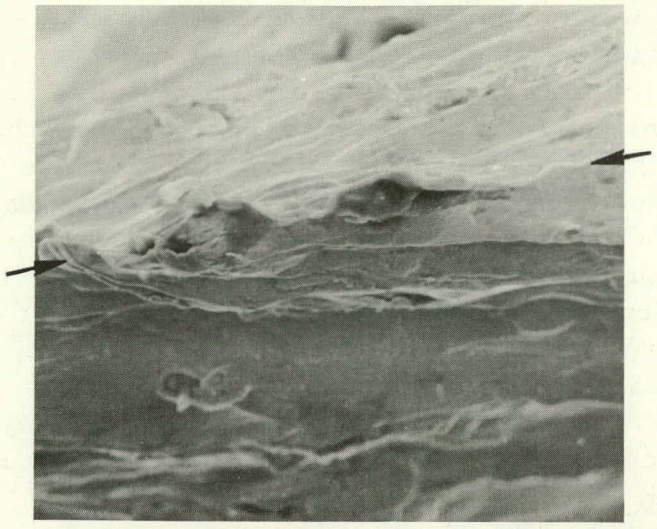

Fig. III.5

SEM Fractograph of Zircaloy-4 Specimen Fractured at $\dot{\epsilon} = 3.3 \times 10^{-2}$ s^{-1} after 2-h Hold Time at 950°C. Fracture edge is the line joining the arrows. Mag. 500X. ANL Neg. No. 306-75-131.

Metallographic examination of the specimens tested at 850°C revealed that the α grains in the deformed region of the specimen with a 10-min hold time were completely recrystallized and equiaxed, whereas the grains in the specimen with the 120-min hold time were elongated and only partly recrystallized.

To examine the microstructure before the start of deformation, specimens were quenched from high temperature after various hold times. A metallographic examination of these specimens reveals that the 2-h hold time at 850°C caused the χ- and β-phase material within the α grains to coalesce and move toward the grain boundaries. The absence of soft β-phase particles within the α grains would decrease the extent of recovery and recrystallization and therefore reduce the total elongation in the material.

To determine the role of β-phase material within the original α grains on the recrystallization and the stabilization of recrystallized α grains, we conducted the following experiment. The as-received Zircaloy was prestrained to $\epsilon = 0.003$ at 700°C, heated to 850°C, held for 2 h, and then strained to fracture. As a result of the small prestrain at 700°C, the large total strain behavior was reestablished even after the 2-h hold time; i.e., the specimen fractured at $\epsilon = 2.00$. Prestraining at 700°C introduced additional defects and dislocations in the structure. When this specimen was heated to the two-phase region, more β phase precipitated within the α grains as a result of the additional nucleation sites. During the 2-h hold time at 850°C, β-phase coalescence (and also the χ phase present) was difficult because of the additional defects introduced during prestraining at 700°C. Since a substantial amount of the β and χ phases remained within the original α grains, this specimen exhibited superplastic deformation similar to the specimen with the 10-min hold time at 950°C without low-temperature prestrain.

3. Effect of Texture on the Uniaxial-elongation Behavior of Zircaloy-4

Scoping tests were conducted to determine the effect of texture in Zircaloy on the tensile-elongation behavior at 850°C, the temperature at which

maximum superplastic deformations were observed. The texture of the as-received Zircaloy sheet indicated that the concentration of basal poles was ~30° from the radial direction and tilted toward the transverse direction. The longitudinal and transverse specimens were parallel and perpendicular to the rolling direction of the sheet, respectively. Figures III.6 and III.7 show the effect of texture on the uniform and total strain of Zircaloy specimens at temperatures between ambient and 1400°C. Since high-temperature β phase has a body-centered-cubic crystal structure, texture effects are expected to be less significant above 1000°C. At lower temperatures, texture does not appear to have a significant effect on the uniform strain (see Fig. III.6); however, the maximum in the total strain at ~850° is less pronounced for the transverse specimens. This observation implies that prism slip is important during superplastic deformation at 850°C, since the grains in the longitudinal specimens are more favorably oriented for such slip.

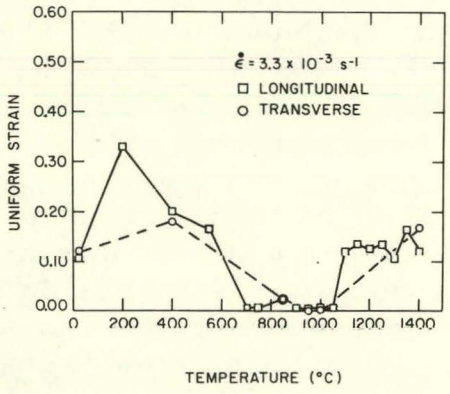

Fig. III.6. Temperature Dependence of Uniform Strain of Longitudinal and Transverse Zircaloy-4 Specimens. ANL Neg. No. 306-75-190.

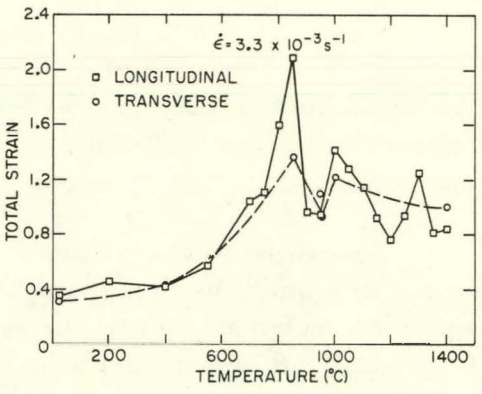

Fig. III.7. Effect of Temperature on Total Strain of Longitudinal and Transverse Zircaloy-4 Specimens. ANL Neg. No. 306-75-194.

Figure III.8 shows the variation of the second-stage work-hardening exponent of Zircaloy as a function of temperature for the longitudinal and transverse specimens. As in Ref. 1, the stress-strain data for the specimens with longitudinal texture were analyzed by the Crussard-Jaoul method based on the

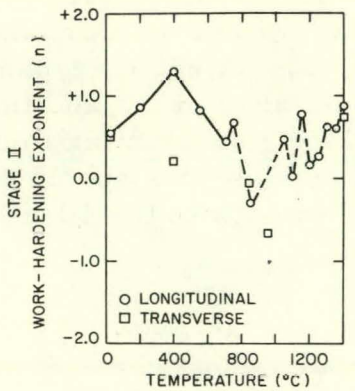

Fig. III.8

Temperature Dependence of Second-stage Work-hardening Exponent of Longitudinal and Transverse Zircaloy-4 Specimens. ANL Neg. No. 306-75-192.

empirical equation $\sigma = \sigma_0 + k\epsilon^n$. At 400°C, the value of n for longitudinal and transverse specimens is significantly different. This is probably due to favorable grain orientations for prism slip in the longitudinal specimens and dynamic strain aging.

4. Effect of Microstructural Morphology on the Tensile Properties of α-Zircaloy

Figure III.9 shows the effect of α-phase morphology on the engineering stress-strain behavior of Zircaloy-4 at 400°C. Without the high-temperature anneals at 850 and 1000°C, the microstructure of the as-received material is completely equiaxed α. This material has an ultimate tensile strength (UTS) of ~150 MPa and a total strain of 0.42. After a 20-min anneal at 850°C and cooling to 400°C, the structure will contain ~10% α in the acicular form, and the remainder will be equiaxed. Introduction of this small fraction of α' raises the UTS to ~160 MPa and lowers the total strain to ~0.34. After a 20-min anneal at 1000°C, the entire microstructure at 400°C will be acicular α'; the UTS increases to ~190 MPa, and the ductility drops to ~0.2 total strain. Thus, apart from oxidation effects, the β→α' microstructural transformation also tends to decrease the ductility in Zircaloy that has undergone a high-temperature excursion into the β-phase field.

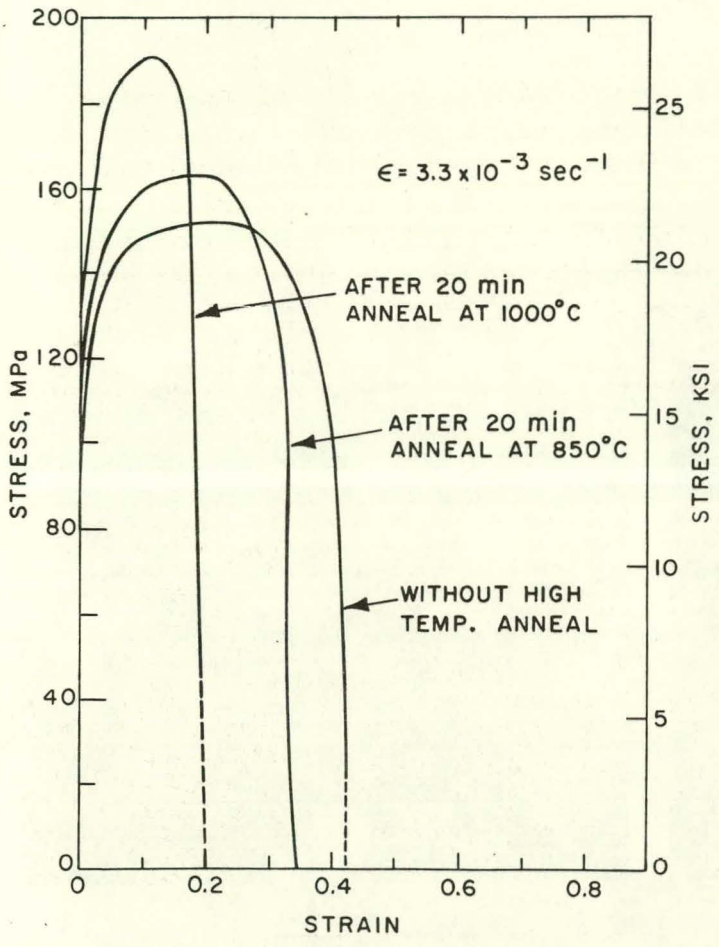

Fig. III.9. Effect of α-phase Morphology on Engineering-stress/Engineering-strain Curve of Zircaloy-4 at 400°C. Neg. No. MSD-61851.

The lower curve in Fig. III.10 shows the total strain of samples that were heated to 1000°C and then cooled at 200°C/min through the two-phase region to the deformation temperatures. A comparison of these data with the upper curve for equiaxed α-phase material indicates that the α-phase morphology has a pronounced effect on the total elongation. This is particularly evident between 800 and 850°C, in the two-phase region, where the large superplastic elongations were not observed for the transformed α' material.

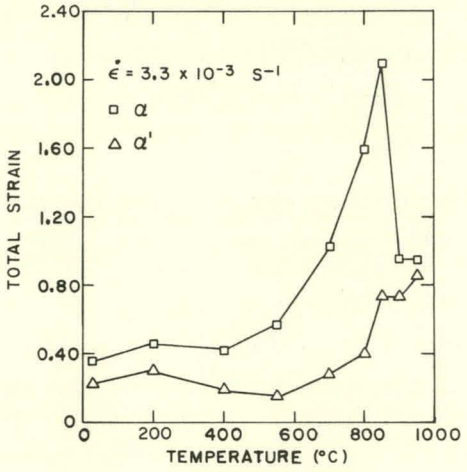

Fig. III.10

Influence of α-phase Morphology on Total Strain of Zircaloy-4 at Temperatures between Ambient and 950°C. ANL Neg. No. 306-75-195.

Figures III.11 and III.12 show SEM fractographs of the as received and annealed (20 min at 1000°C) specimens, respectively, that were fractured at 400°C. The as-received specimen (Fig. III.11) showed the typical equiaxed dimples that failed as a result of normal stress; the fracture surface was perpendicular to the tensile axis. The fracture region of the acicular α' material (Fig. III.12) showed elongated dimples that failed as a result of shear stress; the fracture surface was ~45° to the tensile axis.

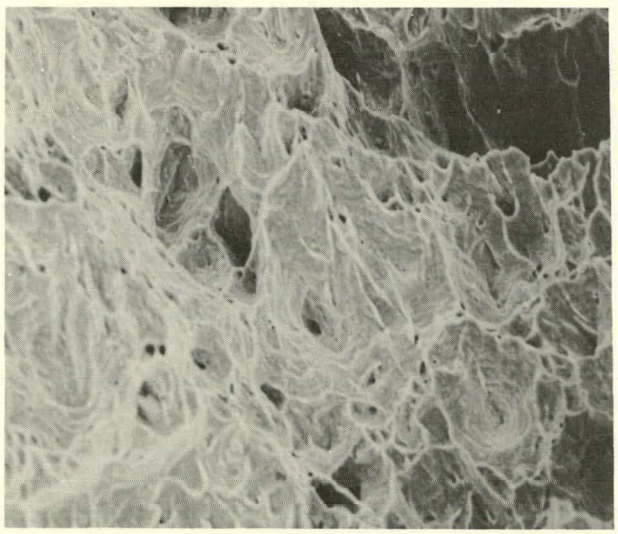

Fig. III.11. SEM Fractograph of As-received Zircaloy-4 Specimen Fractured at 400°C, $\dot{\epsilon}$ = 3.3 x 10^{-3} s^{-1}. Mag. 500X. ANL Neg. No. 306-75-119.

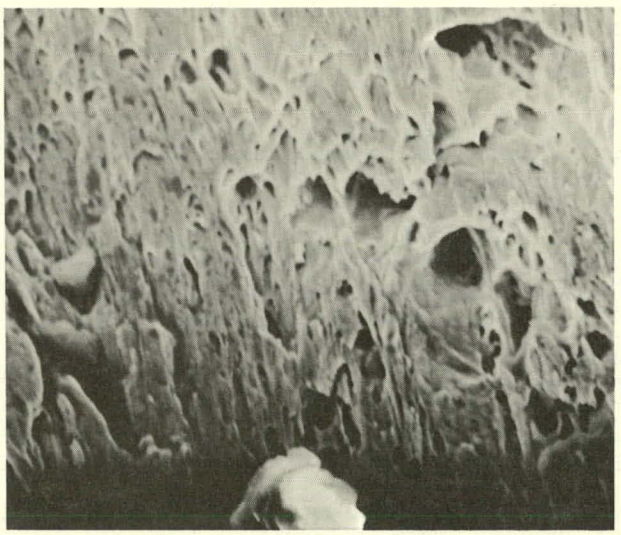

Fig. III.12. SEM Fractograph of Zircaloy-4 Specimen Cooled from β-phase Field and Fractured at 400°C, $\dot{\epsilon}$ = 3.3 x 10^{-3} s^{-1}. Mag. 1000X. ANL Neg. No. 306-75-125.

5. Grain-size Dependence of the Flow Stress of β-Zircaloy-2

Information on the kinetics of grain growth in Zircaloy was given in the previous quarterly report.[1] Considerable grain growth can occur during

oxidation, homogenization of the oxidized specimens, and the short hold time before deformation at temperatures above ~1000°C. The effect of grain size on the flow stress of as-received Zircaloy-2 was therefore determined at 990 and 1100°C. The results in Figs. III.13 and III.14 show that the flow stress for coarse-grain material, i.e., grain size >200 μm, is almost independent of grain size. Additional information will be obtained for Zircaloy with a grain size <50 μm.

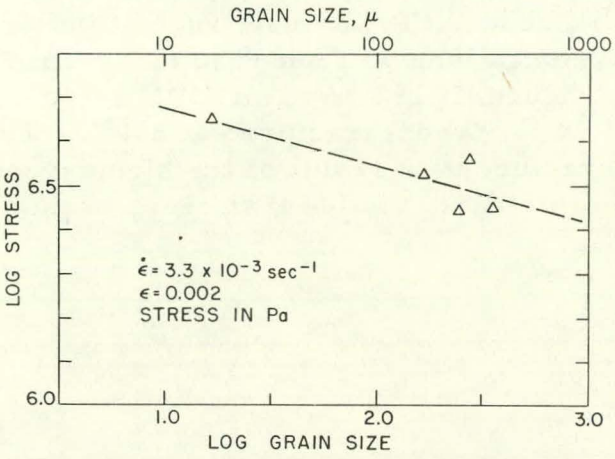

Fig. III.13. Grain-size Dependence of Flow Stress of Zircaloy-2 at 990°C. Neg. No. MSD-61846.

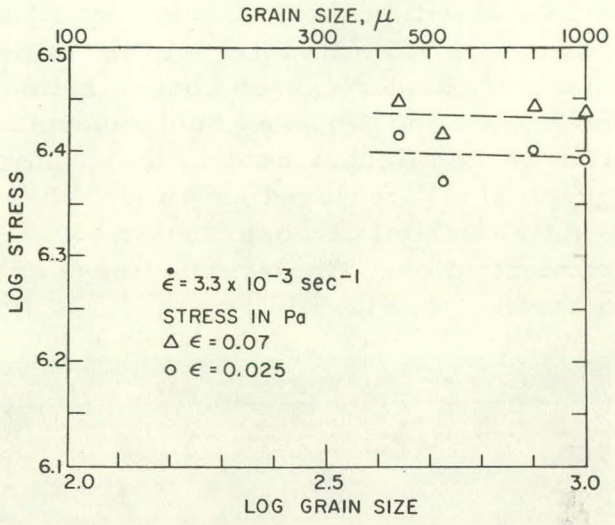

Fig. III.14. Variation of Flow Stress with Grain Size of Zircaloy-2 at 1100°C. Neg. No. MSD-61845.

B. Effect of Oxygen on the Tensile Properties of Zircaloy-4

The effect of oxygen concentration on the tensile properties of homogeneous Zircaloy-4/oxygen alloys is also being investigated at temperatures between 700 and 1400°C. Figure III.15 shows that an increase in the oxygen concentration from 0.11 to 0.5 wt % shifted the peak in the total strain from ~850 to 900°C, although the height of the peak was not affected significantly. This type of behavior can be rationalized in terms of the Zircaloy-oxygen phase diagram in Ref. 1. Zircaloy containing ~0.11 wt % oxygen has a sufficient volume fraction of β phase at 850°C to have β-phase particles within the α grains that contribute to superplastic deformation. Since the temperature of the α-phase boundary increases as the oxygen concentration of the alloy increases, the alloy with 0.5 wt % oxygen will have a smaller volume fraction of β phase at 850°C. The β-phase material

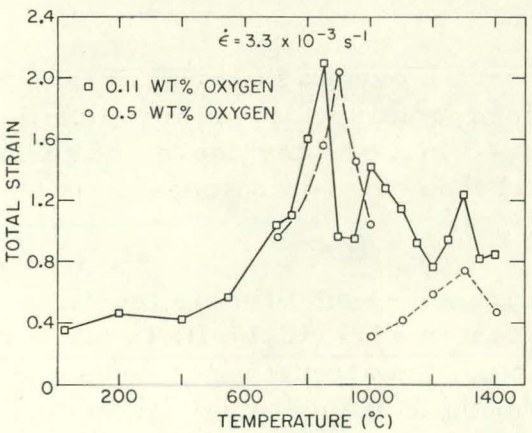

Fig. III.15. Effect of Oxygen on Temperature Dependence of Total Strain of Zircaloy-4. ANL Neg. No. 306-75-198.

within the α grains is not present in sufficient quantity to stabilize the recrystallized α grains; therefore superplastic elongations are not observed. However, at 900°C, the alloy containing 0.5 wt % oxygen has a volume fraction of β similar to that in the material with 0.11 wt % oxygen at 850°C, and both materials exhibit superplastic behavior at the respective temperatures. Furthermore, the β-phase volume fraction in the 0.5 wt % oxygen alloy at 1000°C is similar to that in the as-received material (0.11 wt %) at 950°C, and both alloys have considerably lower ductilities because of the presence of the hard α-phase material within the β matrix. Small additions of oxygen to Zircaloy appear to cause a shift in the total strain-temperature curve to higher temperatures; however, higher oxygen concentrations will reduce the intrinsic ductility of both the α and β phases, and superplastic elongations will not result, irrespective of the microstructural morphology. Figure III.16 shows an SEM fractograph of a Zircaloy-4 specimen, with 2.3 wt % oxygen, fractured at 850°C. The α phase exhibits transgranular cleavage fracture as a result of the high oxygen concentration. The river patterns are more clearly visible than those in the α particle in Fig. III.3.

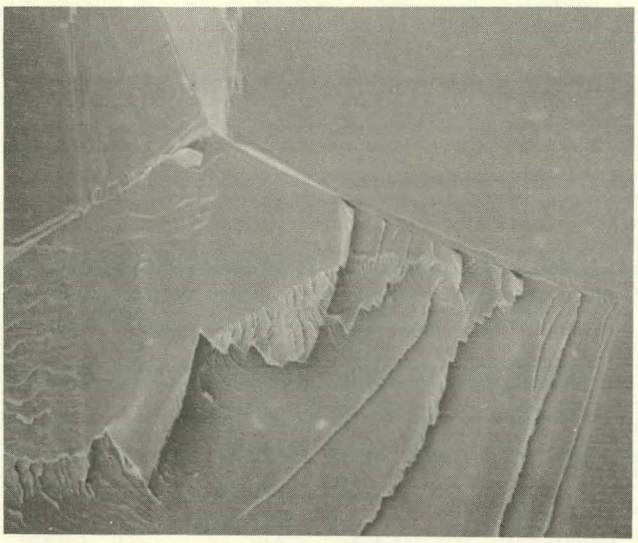

Fig. III.16

SEM Fractograph of Zircaloy-4 Specimen with 2.3 wt % Oxygen Fractured at 850°C, $\dot{\epsilon} = 3.3 \times 10^{-3}\ s^{-1}$. Mag. 200X. ANL Neg. No. 306-75-132.

The data points in Fig. III.15 for the 0.5 wt % oxygen material at temperatures between 1000 and 1400°C were obtained from specimens in which the oxidation and homogenization procedures resulted in a greater degree of grain growth. The total strain at 1000°C for material from the two batches is quite different.

The effect of oxygen concentration in Zircaloy-4 on ultimate tensile strength and the uniform and total strain is shown in Figs. III.17-III.19 for temperatures of 1200, 1300, and 1400°C. As expected, the strength increases and the ductility decreases as the oxygen concentration in the material increases. Grain growth is considerable at these temperatures; i.e., in some instances, a single grain encompassed the width and thickness of the fracture region of the specimens. Therefore, different grain sizes and orientations may contribute to the complex dependence of the tensile properties on oxygen concentration.

The effect of oxygen on the work-hardening behavior of Zircaloy-4 at three strain rates is shown in Tables III.1-III.3. More positive values of n and k are related to a higher work-hardening rate; more negative values of n and k are related to a greater extent of dynamic recovery. The results in Tables III.1-III.3 indicate that a higher strain rate tends to increase both the work-hardening rate in the initial stage (larger values of n and k) and the dynamic recovery in the later stage of deformation (smaller values of n and k).

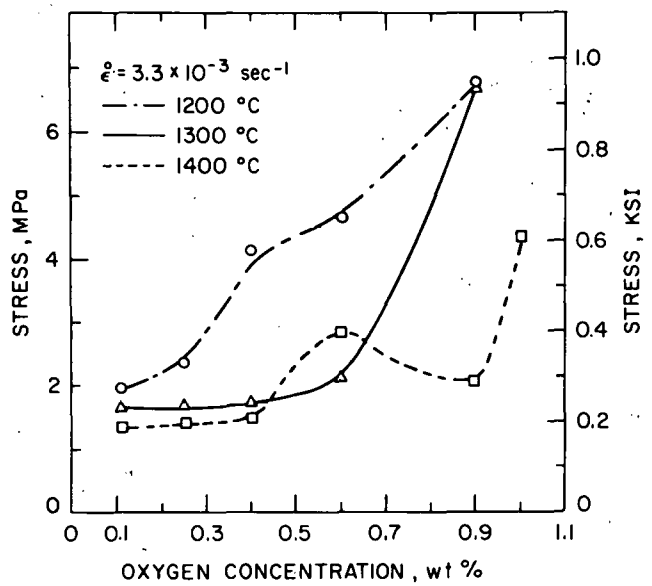

Fig. III.17

Variation of Ultimate Tensile Strength of Zircaloy-4 with Oxygen Concentration at 1200, 1300, and 1400°C. Neg. No. MSD-61848.

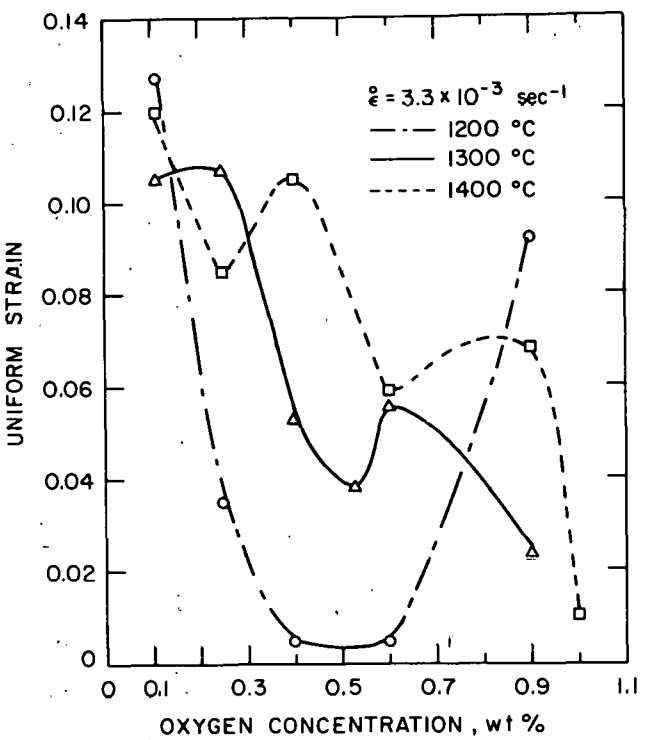

Fig. III.18

Oxygen-concentration Dependence of Uniform Strain of Zircaloy-4 at 1200, 1300, and 1400°C. Neg. No. MSD-61849.

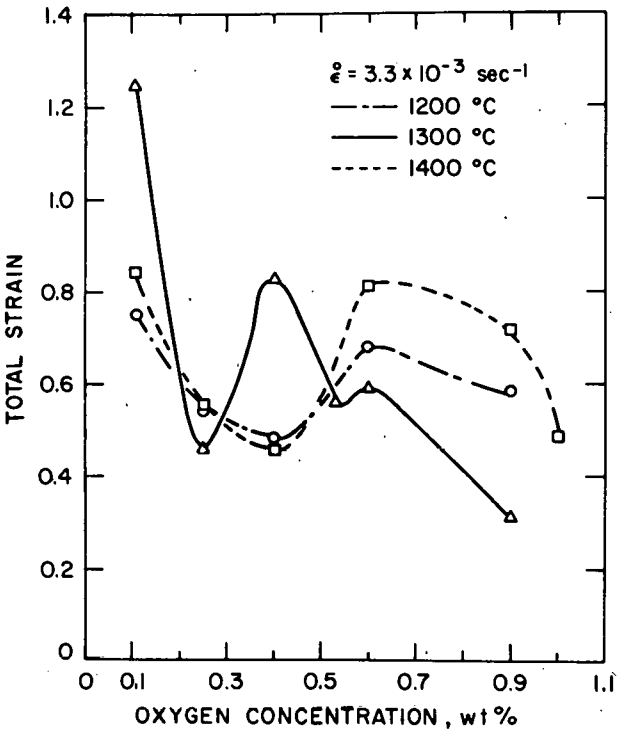

Fig. III.19

Effect of Oxygen Concentration on Total Strain of Zircaloy-4 at 1200, 1300, and 1400°C. Neg. No. MSD-61850.

TABLE III.1. Least-squares Work-hardening Constants for Zircaloy-4/Oxygen Alloys, $\dot{\epsilon} = 3.3 \times 10^{-3}$ s^{-1}

Temp, °C	Oxygen, wt %	Stage Number	Strain Interval	n	k, Pa
1000	0.25	1	0.0004-0.0024	0.71	2.3×10^{8}
		2	0.0028-0.0090	-2.20	-2.6×10^{0}
	0.40	1	0.0004-0.0028	0.78	1.2×10^{8}
		2	0.0032-0.0150	-0.59	-4.5×10^{4}
1100	0.25	1	0.0004-0.0016	0.21	2.4×10^{7}
		2	0.0020 0.0050	-0.82	-2.8×10^{7}
	0.39	2	0.0004-0.0700	0.21	1.5×10^{6}
1200	0.24	1	0.0004-0.0050	0.26	2.3×10^{6}
		2	0.0060-0.0250	-0.46	-3.1×10^{4}
	0.40	1	0.0004-0.0020	0.68	9.6×10^{7}
		2	0.0024-0.0060	-3.50	-1.7×10^{-4}
	0.59	1	0.0004-0.0020	0.75	1.1×10^{7}
		2	0.0020-0.0050	-0.56	-2.9×10^{3}
	0.89	1	0.0004-0.0020	0.75	1.1×10^{8}
		2	0.0024-0.0700	-0.12	-3.0×10^{6}
1300	0.39	2	0.0004-0.0140	0.92	6.1×10^{6}
		3	0.0150-0.0500	0.11	1.5×10^{6}
	0.60	2	0.0004-0.0500	0.14	2.1×10^{6}
	0.92	2	0.0004-0.0040	0.82	1.8×10^{8}
		3	0.0050-0.0200	-1.50	-4.2×10^{2}
1400	0.27	2	0.0012-0.0150	1.10	1.2×10^{7}
		3	0.0200-0.0700	-0.31	-1.4×10^{5}
	0.39	2	0.0004-0.0040	0.87	1.4×10^{7}
		3	0.0050-0.0900	0.19	1.5×10^{6}
	0.90	2	0.0004-0.0060	0.93	3.4×10^{7}
		3	0.0070-0.1300	0.20	3.9×10^{6}

TABLE III.2. Least-squares Work-hardening Constants for Zircaloy-4/Oxygen Alloys, $\dot{\epsilon} = 3.3 \times 10^{-4}\ s^{-1}$

Temp, °C	Oxygen, wt %	Stage Number	Strain Interval	n	k, Pa
1000	0.25	1	0.0004-0.0028	0.53	6.0×10^{7}
		2	0.0032-0.0150	-1.30	-6.1×10^{2}
	0.32	1	0.0004-0.0016	0.56	7.4×10^{7}
		2	0.0020-0.0130	-1.10	-1.2×10^{3}
	0.41	1	0.0004-0.0028	0.06	2.2×10^{7}
		2	0.0032-0.0150	-1.20	-7.4×10^{2}
1100	0.25	1	0.0004-0.0020	0.50	2.1×10^{7}
		2	0.0024-0.0050	-2.20	-5.1×10^{-1}
	0.31	1	0.0004-0.0020	0.15	9.8×10^{6}
		2	0.0024-0.0040	-3.90	-6.9×10^{-6}
	0.42	1	0.0004-0.0032	0.73	1.6×10^{7}
		2	0.0036-0.0100	-1.10	-2.7×10^{2}
1200	0.23	1	0.0008-0.0080	1.00	2.9×10^{7}
		2	0.0090-0.0450	-0.30	-1.2×10^{5}
	0.59	1	0.0004-0.0028	0.44	7.0×10^{6}
		2	0.0032-0.0050	-2.30	-1.4×10^{-1}
1300	0.24	1	0.0004-0.0040	1.06	2.5×10^{7}
		2	0.0040-0.0700	0.00	9.9×10^{7}
	0.55	1	0.0004-0.0016	0.86	1.5×10^{7}
		2	0.0020-0.0300	0.05	6.3×10^{5}
	0.87	1	0.0004-0.0050	0.79	5.3×10^{7}
		2	0.0060-0.0300	-0.85	-4.8×10^{3}
1400	0.31	1	0.0004-0.0130	1.05	3.7×10^{6}
		2	0.0140-0.0500	0.28	4.7×10^{5}
	0.80	1	0.0004-0.0020	0.56	1.0×10^{7}
		2	0.0024-0.0070	-1.40	-3.6×10^{1}
	0.99	1	0.0004-0.0050	0.57	1.7×10^{7}
		2	0.0060-0.0120	-2.40	-5.3×10^{0}

TABLE III.3. Least-squares Work-hardening Constants for Zircaloy-4/Oxygen Alloys, $\dot{\epsilon} = 3.3 \times 10^{-5}\ s^{-1}$

Temp, °C	Oxygen, wt %	Stage Number	Strain Interval	n	k, Pa
1000	0.23	1	0.0004-0.0028	0.85	5.1×10^{7}
		2	0.0032-0.0060	-0.97	-1.3×10^{3}
	0.43	1	0.0004-0.0024	0.63	6.7×10^{7}
		2	0.0028-0.0500	-0.16	-1.4×10^{6}
1100	0.43	1	0.0004-0.0032	0.76	3.4×10^{7}
		2	0.0036-0.0250	-0.72	-8.7×10^{3}
1200	0.43	1	0.0004-0.0036	0.84	2.1×10^{7}
		2	0.0040-0.0070	-1.30	-1.1×10^{2}
1300	0.79	1	0.0004-0.0032	0.83	2.6×10^{7}
		2	0.0036-0.0300	-0.37	-5.9×10^{4}
	0.94	1	0.0004-0.0040	0.86	3.5×10^{7}
		2	0.0050-0.0450	-0.50	-2.7×10^{4}
1400	0.31	1	0.0004-0.0150	1.05	1.9×10^{6}
		2	0.0200-0.1100	0.46	6.2×10^{5}
	1.00	1	0.0004-0.0040	0.96	1.0×10^{8}
		2	0.0050-0.0250	-0.21	-6.8×10^{5}

Figures III.20-III.24 show the effect of strain on the strain-rate sensitivity of Zircaloy-4 containing different oxygen concentrations in the range of 0.11-1.0 wt % for temperatures between 700 and 1400°C. Near the low-temperature peak in the curve of total elongation versus temperature, i.e., 850°C in Fig. III.1, small additions of oxygen do not decrease the strain-rate sensitivity of Zircaloy. The m values in Fig. III.20 for an alloy with 0.5 wt % oxygen are essentially the same as those for the as-received material with

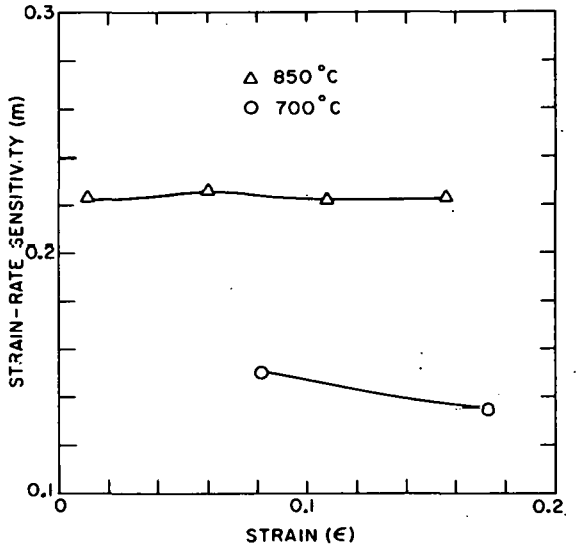

Fig. III.20. Strain Dependence of Strain-rate Sensitivity of Zircaloy-4 with 0.5 wt % Oxygen at 700 and 850°C. Strain-rate change between 3.3 x 10^{-4} and 3.3 x 10^{-3} s^{-1}. ANL Neg. No. 306-75-196.

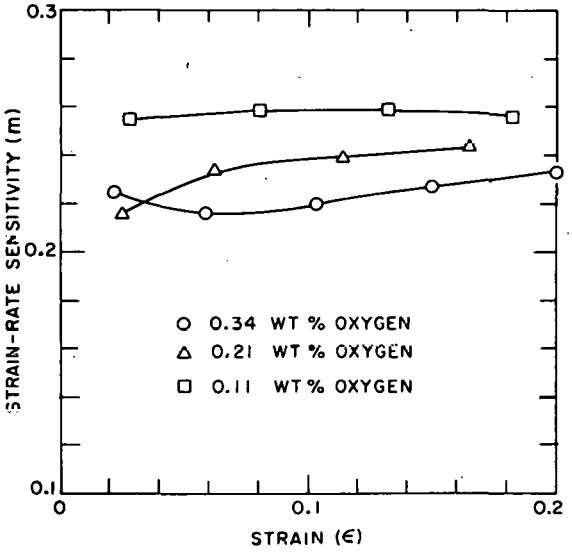

Fig. III.21. Effect of Strain on Strain-rate Sensitivity of Zircaloy-4 at 1000°C with 0.11, 0.21, and 0.34 wt % Oxygen. Strain-rate change between 3.3 x 10^{-4} and 3.3 x 10^{-3} s^{-1}. ANL Neg. No. 306-75-197.

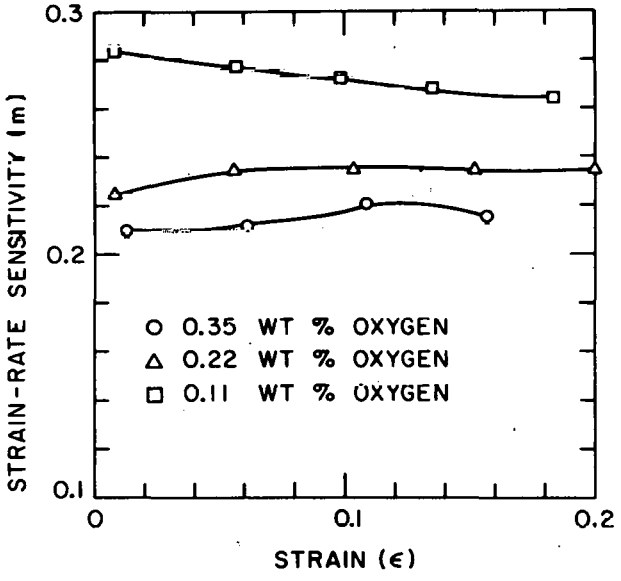

Fig. III.22

Variation of Strain-rate Sensitivity of Zircaloy-4 with Strain at 1200°C with 0.11, 0.22, and 0.35 wt % Oxygen. Strain-rate change between 3.3 x 10^{-4} and 3.3 x 10^{-3} s^{-1}. ANL Neg. No. 306-75-193.

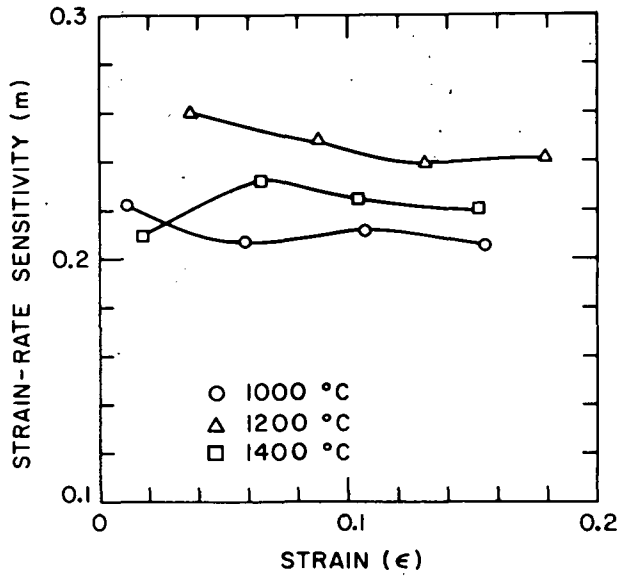

Fig. III.23

Effect of Strain on Strain-rate Sensitivity of Zircaloy-4 with 0.25 wt % Oxygen at 1000, 1200, and 1400°C. Strain-rate change between 3.3×10^{-5} and 3.3×10^{-4} s^{-1}. ANL Neg. No. 306-75-191.

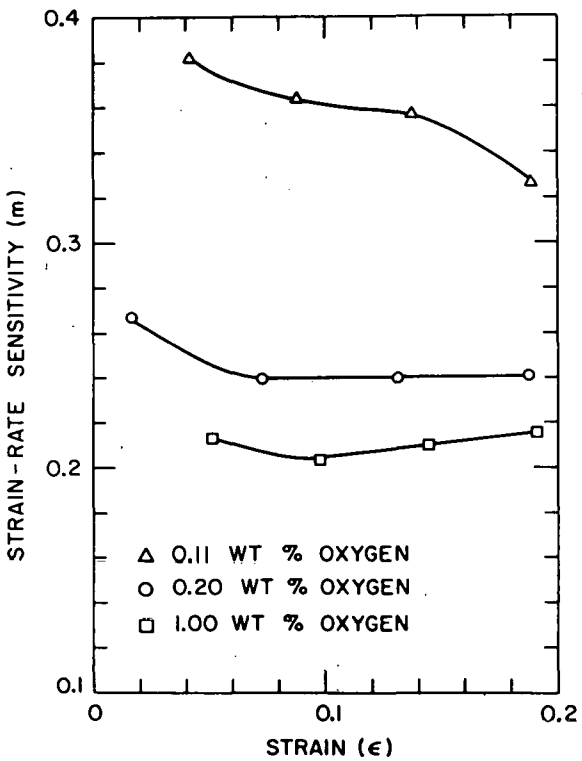

Fig. III.24

Strain Dependence of Strain-rate Sensitivity of Zircaloy-4 at 1400°C with 0.11, 0.2, and 1.0 wt % Oxygen. Strain-rate change between 3.3×10^{-4} and 3.3×10^{-3} s^{-1}. ANL Neg. No. 306-75-189.

0.11 wt % oxygen (see Fig. III.17 in Ref. 1). Similar to the behavior of as-received material, the strain-rate sensitivity of Zircaloy containing 0.5 wt % oxygen is not strain-dependent at 850°C (near the strain-temperature peak), but decreases as the strain increases at 700°C (away from the superplastic elongation peak).

At higher temperatures (≥1000°C), an increase in the oxygen concentration decreases the strain-rate sensitivity to the extent that the superplastic

elongation behavior is diminished or eliminated. Grain growth during homogenization of the oxygen-charged specimens may also contribute to the decrease in elongation. Figure III.25 shows the oxygen dependence of the strain-rate sensitivity parameter m for temperatures of 1200, 1300, and 1400°C. These results are consistent with Zircaloy tensile data obtained in an air environment[8] in which oxidation during the test eliminated the superplastic elongation behavior at the higher temperatures.

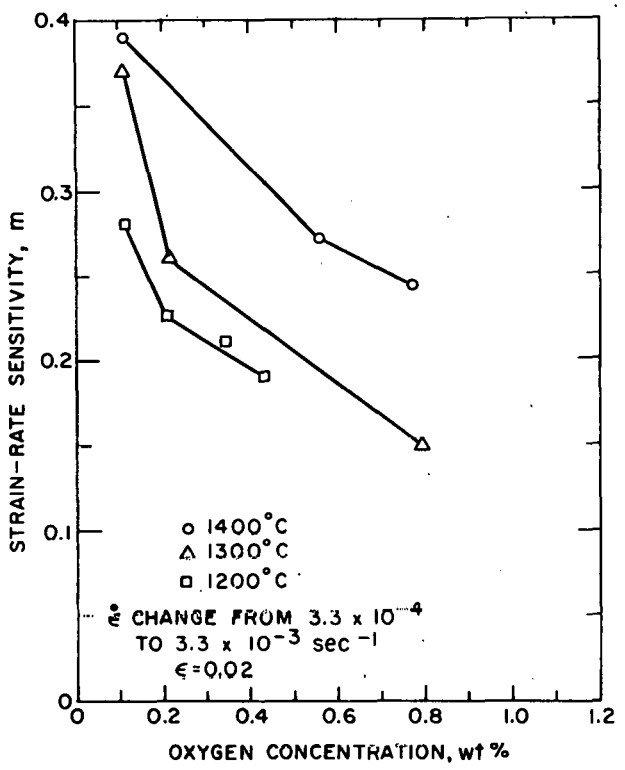

Fig. III.25. Oxygen-concentration Dependence of Strain-rate Sensitivity of Zircaloy-4 at 1200, 1300, and 1400°C. Neg. No. MSD-61844.

C. Diametral Expansion and Rupture Behavior of Zircaloy-4 Fuel Cladding

The biaxial deformation and rupture behavior of Zircaloy-4 fuel cladding with a range of oxygen concentrations and $ZrO_2/\alpha/\beta$ phase thicknesses are being investigated. The biaxial test program will involve temperature- and pressure-transient loading conditions, including simulated LOCA and power-coolant-mismatch (PCM) situations as well as short-time stress-rupture tests. The mechanical-property data and microstructural information on the fuel cladding will be correlated with similar results being obtained from uniaxial tensile tests. The biaxial-deformation results will provide input data for an elastic-plastic finite-element deformation code that is being modified to predict the diametral strain and rupture behavior of Zircaloy cladding after various degrees of oxidation.

1. Tube-rupture Test Conditions and Test Matrix

The biaxial testing program will be conducted in an inert gas or vacuum environment that precludes oxidation during the deformation process. The five types of biaxial test conditions (Fig. III.26) include (I) uncontrolled temperature-transient test (power input rate controlled), (II) controlled temperature-transient test, (III) isothermal pressure-transient test, (IV) stress-rupture test, and (V) simulated LOCA test (controlled temperature and pressure transient). For a constant rate of power input into the specimen, i.e., case I, the heating rate decreases as the material undergoes the $\alpha \rightarrow \beta$ phase transformation in a high-temperature burst test. A rapid-feedback-control system for the power supply will be used to achieve the linear heating rate in case II. The

isothermal tests (III and IV) are expected to be useful in the interpretation of the deformation behavior, since the microstructural effects that result from the transient heating conditions will be eliminated. The latter data will be used to develop a correlation between the high-temperature uniaxial and biaxial mechanical-property data as well as to interpret the stress-strain data from the more complex load conditions in the LOCA simulation tests, i.e., case V.

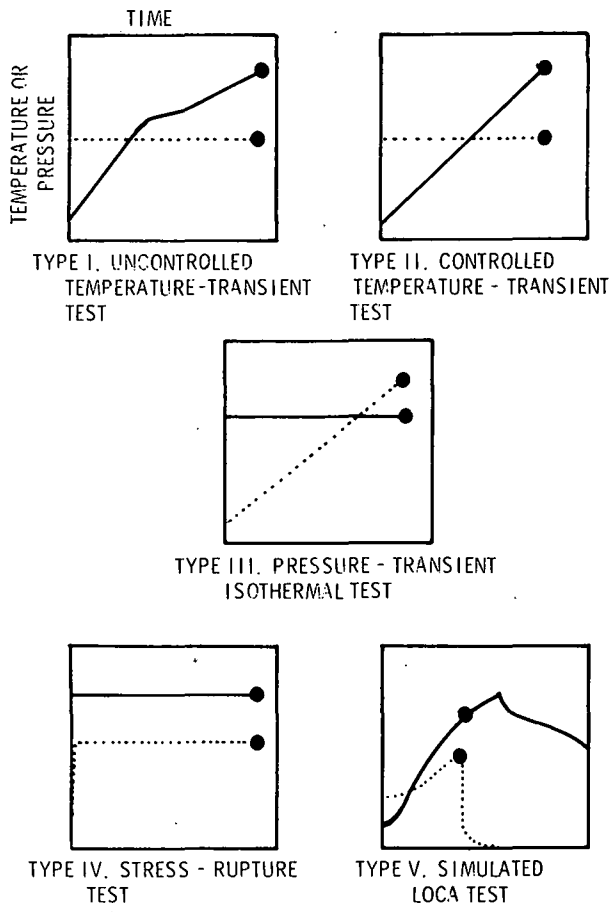

Fig. III.26. Types of Temperature- and Pressure-transient Conditions That Will Be Used in Zircaloy Tube-burst Tests. ANL Neg. No. 306-75-215.

Tables III.4-III.6 give the test matrices for the controlled temperature-transient, isothermal pressure transient, and stress-rupture tests on Zircaloy-4 fuel cladding with different oxygen concentrations and $ZrO_2/\alpha/\beta$ phase distributions. The test conditions were selected to encompass the range of temperatures, pressures, and heating rates that are applicable to LOCA situations and to provide a basis of comparison with published results on the transient tube-burst properties of Zircaloy cladding.

2. Zircaloy-4 Tubing and Specimen Geometry

The Zircaloy-4 fuel cladding that will be used in the tube-burst measurements was fabricated by Sandvik Special Metals Corp., Kennewick, Washington. The material, 0.430 ± 0.002-in. OD by 0.025-in.-wall thickness, was 80% cold-worked and stress-relieved at 500°C for 4 h. The reported surface roughness for the OD and ID are 20 and 25 μin., respectively, for Lot 7FD11 and 19 μin. for both surfaces in Lot 7FD12. The chemical composition of the two lots of tubing is shown in Table III.7.

A schematic of the tube-burst specimen is shown in Fig. III.27. The Zircaloy tubing was cut into 6-in. lengths, and both ends were welded to 0.50-in. OD Zircaloy-2 sleeves that fit into the stainless steel Swageloks. The high-purity alumina rod and the Zircaloy or brass end plugs minimized the gas volume that was released during rupture of the specimen.

TABLE III.4. Test Matrix for Controlled Temperature-transient Tube-burst Tests on As-received and Oxidized Zircaloy-4 Fuel Cladding[a]

Initial Pressure, psig	Heating Rate, °C/s				
	5	10	20	50	100
50	A, AA	-	A, 3H-5H	5H	-
100	5H, 7H C1	A, 5H 7H, C1	A, C1 2H-7H	A, C1 5H, 7H	A, C1 5H, 7H
200	A	-	A, AA XH	-	-
300	2H, 5H 7H	2H, 5H 7H	2H, 5H 7H	2H, 5H 7H	2H, 5H 7H
400	-	-	A, AA XH	-	A
500	5H, 10H	5H, 10H	5H, 10H	5H, 10H	5H, 10H
600	A	-	A, AA XH	5H	-
700	C2	-	C2 A, AA	-	C2
1000	A, AA C3	-	XH, C3	5H	A, AA C3
2250	A	-	A, AA XH	5H	-

[a]Definition of symbols:

A = As-received tube; stress-relieved at 500°C for 4 h.
AA = As-received tube; recrystallized at 677°C for 45 min.
XH = Oxidized and homogenized tube with uniform oxygen concentration of X/10 wt % (i.e., 2H, 3H, 4H, ... - 0.2, 0.3, 0.4, ... wt % oxygen, respectively)
C1 = ZrO_2/α composite tube with oxygen concentration gradients in the α-phase.
C2 = $ZrO_2/\alpha/\beta$ composite with oxygen gradients in the β phase.
C3 = $ZrO_2/\alpha/\beta$ composite with no oxygen gradient in the β phase; specimens partially annealed.

TABLE III.5. Test Matrix for Isothermal Pressure-transient Tube-burst Tests on As-received and Oxidized Zircaloy-4 Fuel Cladding[a]

Temperature, °C	Pressurizing Rate, psi/sec			
	5	25	50	100
700	-	-	A, 2H 5H	C1
800	-	-	2H, 5H	C1
850	A, 2H 5H	A, 5H	A, 2H 5H	5H
900	-	-	A, 2H 5H	-
1000	-	MH	A, MH	C2, C3
1050	A, MH	A, MH	A, MH	C2, C3
1100	-	-	A, MH	-
1300	-	-	A, MH	-

[a]Definition of symbols:

A = As-received tube; stress-relieved at 500°C for 4 h.
C1 = ZrO_2/α composite tube with oxygen concentration gradients in the α phase.
C2 = $ZrO_2/\alpha/\beta$ composite with oxygen gradients in the β phase.
C3 = $ZrO_2/\alpha/\beta$ composite with no oxygen gradient in the β phase; specimens partially annealed.
MH = Oxidized and homogenized tube with uniform oxygen concentration of M/10 wt %; β phase martensitically transformed to the acicular α' phase by cooling from the annealing temperature in the β-phase field.

TABLE III.6. Test Matrix for Stress-rupture Tests on As-received and Oxidized Zircaloy-4 Fuel Cladding[a]

Temperature, °C	Internal Pressure, psig					
	50	100	200	300	500	1000
700	-	-	-	-	A, C1	A, C1 2A, 5H
800	-	-	-	-	A, C1	A, C1 2H, 5H
850	A	-	-	-	A, 2H 5H	-
900	A	-	-	-	-	-
1000	A, MH	MH	A, MH	MH	A, MH	A, MH
1050	A	-	-	-	-	-
1100	-	A, MH	-	-	A, MH	MH
1200	-	A, MH	-	-	A, MH	-
1300	A, MH	A, MH	-	-	-	-

[a]Definition of symbols:

A = As-received tube; stress-relieved at 500°C for 4 h.
C1 = ZrO_2/α composite tube with oxygen concentration gradients in the α phase.
XH = Oxidized and homogenized tube with uniform oxygen concentration of X/10 wt % (i.e., 2H, 3H, 4H, ... = 0.2, 0.3, 0.4, ... wt % oxygen, respectively).
MH = Oxidized and homogenized tube with uniform oxygen concentration of M/10 wt %; β phase martensitically transformed to the acicular α' phase by cooling from the annealing temperature in the β-phase field.

TABLE III.7. Chemical Composition of Zircaloy-4 Tubing Used in Burst Tests

Element	wt %	Element	ppm	Element	ppm	Element	ppm
Sn	1.50	O	1300	Al	38	Hf	44
Fe	0.20	N	34	Ca	<10	Ti	<25
Cr	0.12	H	19	Co	<10	W	<25
		C	110	Cu	17	Mo	<25
		B	0.2	Ni	<35	Ta	<100
		C1	<5	Si	83	V	<25

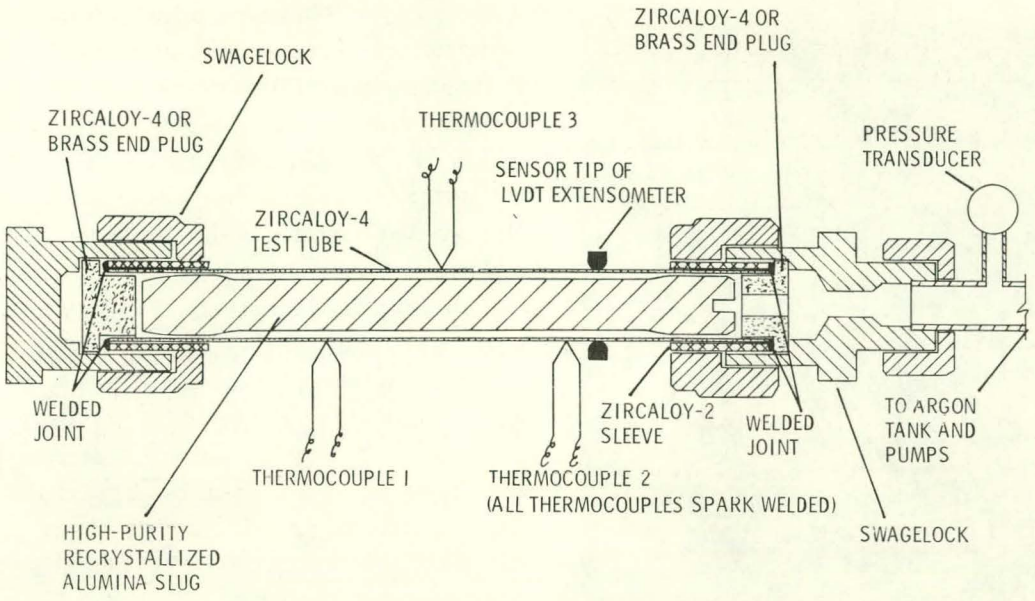

Fig. III.27. Schematic of Zircaloy Tube-burst Specimen. ANL Neg. No. 306-75-205.

3. Description of the Tube-burst Apparatus

The tube-burst apparatus consisted of a standard bell-jar vacuum chamber, a gas-handling system to pressurize the specimen, and a power supply for direct-electrical heating of the tube. Figure III.28 shows the chamber that contains the Zircaloy tube, an array of thermocouples and pressure transducers, and the power-supply electrodes. The upper end of the specimen and the Swagelok fitting were allowed to move freely in the axial direction. During a test, the chamber was evacuated by a mechanical pump to a pressure of $\sim 2 \times 10^{-2}$ torr. Argon was used to internally pressurize the specimen.

In the initial experiments, rapid heating of the specimen was achieved by an alternating-current power supply without an external control system. The temperature distribution in the axial direction was determined from 1-mil-diameter Chromel-Alumel thermocouples that were spark welded to the tube at various locations. The central ~3-in. portion of the specimen could be maintained within ~5°C for temperatures up to a 1000°C. However, heating-rate changes occurred because of the $\alpha \rightarrow \beta$ phase transition and the anomalous temperature dependence of resistivity of Zircaloy and zirconium[9] containing high-oxygen concentrations.

Linear-variable-differential-transducer (LVDT) diametral extensometers are used to continuously monitor the strain in the uniform-temperature zone of the specimen. The signals from the extensometers, thermocouples, and a pressure transducer are recorded on a multichannel high-speed visicorder. A high-speed (1000-frame/s) camera is also used to record the axial and diametral expansions of the tube during the burst test.

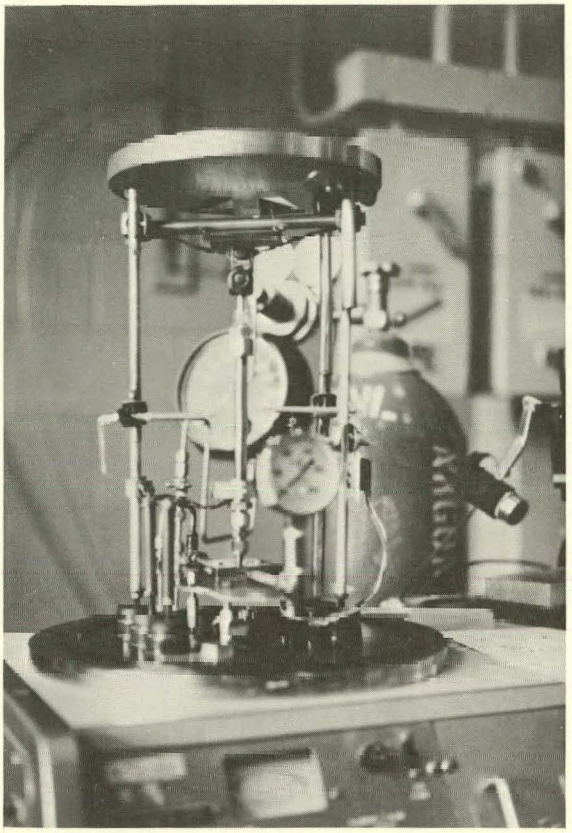

Fig. III.28. Tube-burst Apparatus. ANL Neg. No. 306-75-229.

Based upon the results of the initial tube-burst experiments, the following modifications to the apparatus will be made: (a) A rapid-feedback-control system for the power supply will be built to program the heating rate in the experiments, (b) a capability for a linear increase in the pressure will be incorporated into the pressurization system, (c) a laser light source will be used to obtain sharper images and permit the camera to operate at a higher speed, and (d) a multiple-imaging system that incorporates the use of mirrors will be devised to record the diametral expansion from two additional directions.

4. Results of the Initial Tube-rupture Tests

To establish the test procedures and identify any problems with the tube-burst apparatus, tests were conducted on specimens in the as-received, oxidized-homogenized (0.37 wt % oxygen), and ZrO_2/α composite (oxygen gradient in the α phase) conditions. An initial heating rate of 110°C/s and an internal argon pressure of 570 psig were used. After rupture, examination of the tube included (a) a photograph of the rupture region, (b) a measurement of the circumferential strain at a number of axial locations, (c) an examination of the necking and radial strain distribution from a cross section of the tube in the rupture region, (d) a series of measurements of the diametral strain from the onset of bulging to rupture from individual frames of the film from the high-speed camera, and (e) an examination of the microstructure of the material by optical and electron microscopy. The circumferential strain (C_c) was calculated from

$$C_c = \frac{(C_L - W) - \pi D_0}{\pi D_0}, \qquad (1)$$

where D_0 is the original outside diameter of the tube, W is the width of the rupture, and C_L is the circumference of the tube--determined from measurements on cellophane tape that had been pressed on the surface of the specimens.

Figure III.29 shows the rupture regions of the as-received, oxidized-homogenized, and ZrO_2/α composite specimens that had measured burst temperatures of 909, 1015, and 903°C, respectively. The temperature and pressure

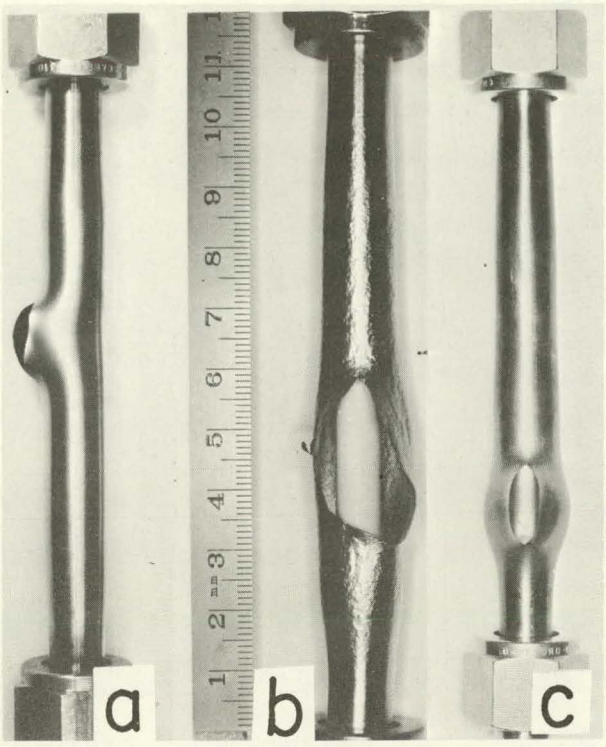

Fig. III.29. Rupture Areas of Zircaloy-4 Tubes in (a) As-received, (b) Oxidized-Homogenized with 0.37 wt % Oxygen, and (c) ZrO_2/α Composite Conditions after Transient Heating. ANL Neg. No. 306-75-209.

for each specimen are plotted as a function of time in Fig. III.30, and the circumferential strain as a function of axial position is shown in Fig. III.31.

The cross sections of the three specimens in the rupture area are shown in Fig. III.32. The as-received and the ZrO_2/α composite specimens exhibited a smooth change in the radial strain and a single-necked region; the oxidized specimen with α' acicular grains and a uniform oxygen concentration of 0.37 wt % had several thinned regions in addition to the rupture region. The microstructures in Figs. III.33 and III.34 represent the necked and adjacent thicker regions, respectively, in the cross section of the oxidized and homogenized specimen shown in Fig. III.32b. Examination of the undeformed regions of this specimen revealed a few α' colonies in which the habit plane of the lenticular α' grains was parallel to the tangential stress, as shown in Fig. III.35. From these observations, it appears that necking occurs preferentially in locations in which the lenticular α' grains are aligned nearly parallel to the tangential stress. However, the α' colonies apparently were more ductile than the structure shown in Fig. III.34. The maximum circumferential strain in the rupture area of the specimen was ~0.33; however, in some cases, the apparent tangential strain of the elongated region of the parallel α' colony was >2.0. Under polarized light, the highly strained α' grains in Fig. III.36 reveal small equiaxed α subgrains, indicating that grain refinement and recrystallization occurred in this region.

Similar α'-plate orientations are evident in Figs. III.37 and III.38 for the necked and unnecked regions in a uniaxial tensile specimen that was held in the β-phase region at 1000°C, cooled at ~100°C/min to 700°C, and strained to failure at this temperature. Necking primarily occurs in regions in which the α' grain structure is parallel to the load direction rather than in regions of random grain orientations. These observations support earlier speculation[1] that the α' basketweave structure should have comparatively good strength properties.

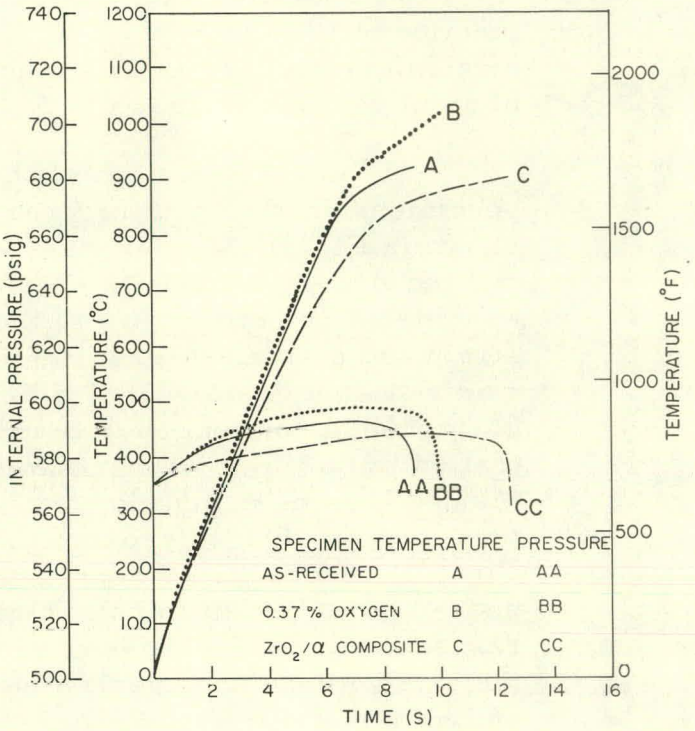

Fig. III.30

Temperature and Internal Pressure as a Function of Time during Rupture Tests on Zircaloy Specimens Described in Fig. III.29. ANL Neg. No. 306-75-224.

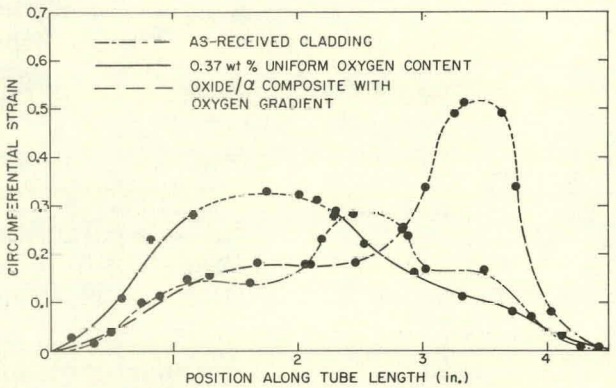

Fig. III.31

Circumferential Strain as a Function of Axial Location for Specimens Described in Figs. III.29 and III.30. The rupture areas are shown by the dashed lines. ANL Neg. No. 306-75-217.

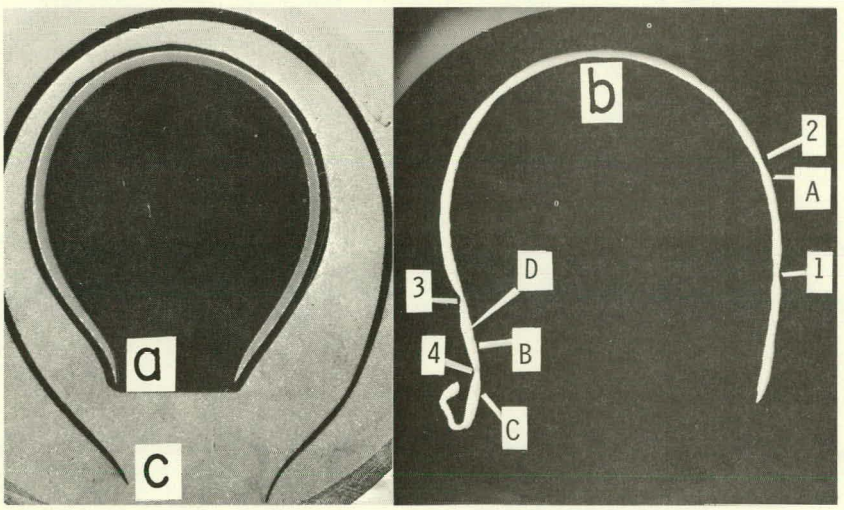

Fig. III.32

Cross Sections of Rupture Areas of Three Specimens Shown in Fig. III.29. (a) As-received specimen. (b) Oxidized-homogenized specimen (Mag. ~2.7X). (c) ZrO_2/α composite specimen (Mag. ~3.1X). ANL Neg. No. 306-75-208.

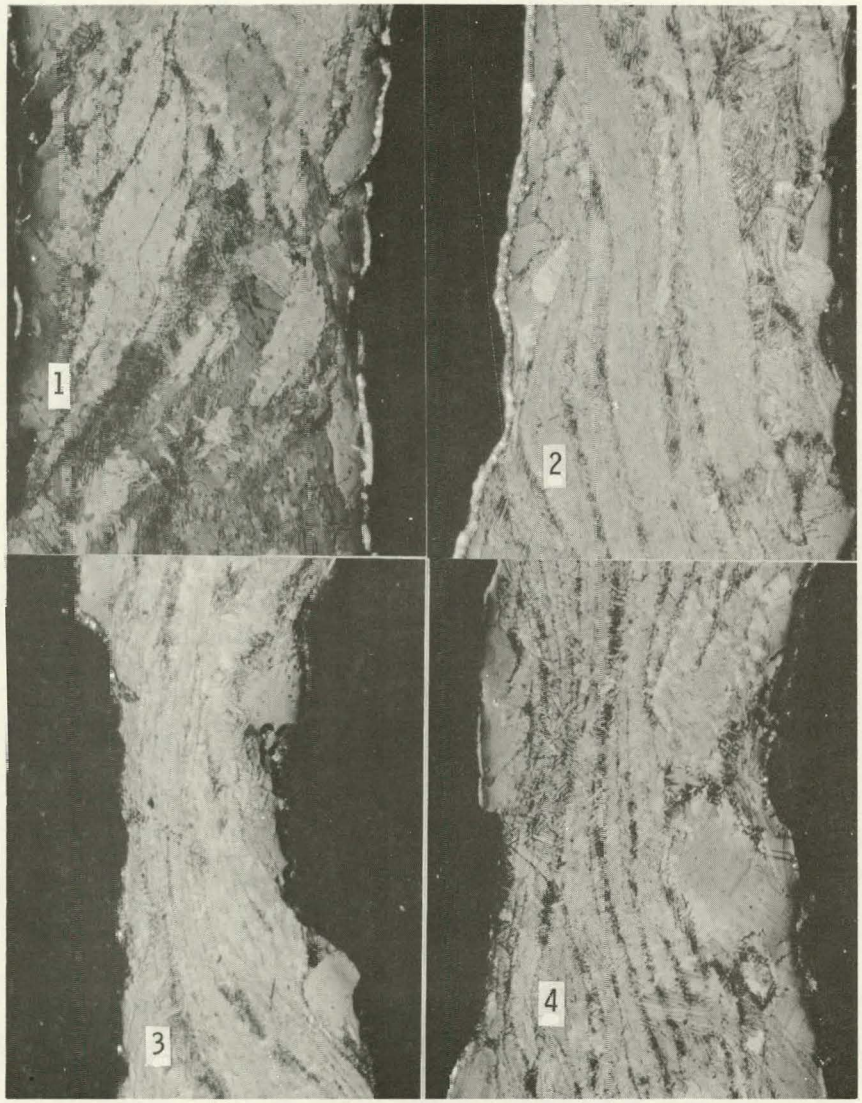

Fig. III.33. Microstructures of Necked Regions in Fig. III.32b That Show Elongated α' Grains Aligned Parallel to Hoop Stress. Etched and anodized. Polarized light. Mag. ~150X. ANL Neg. No. 306-75-228.

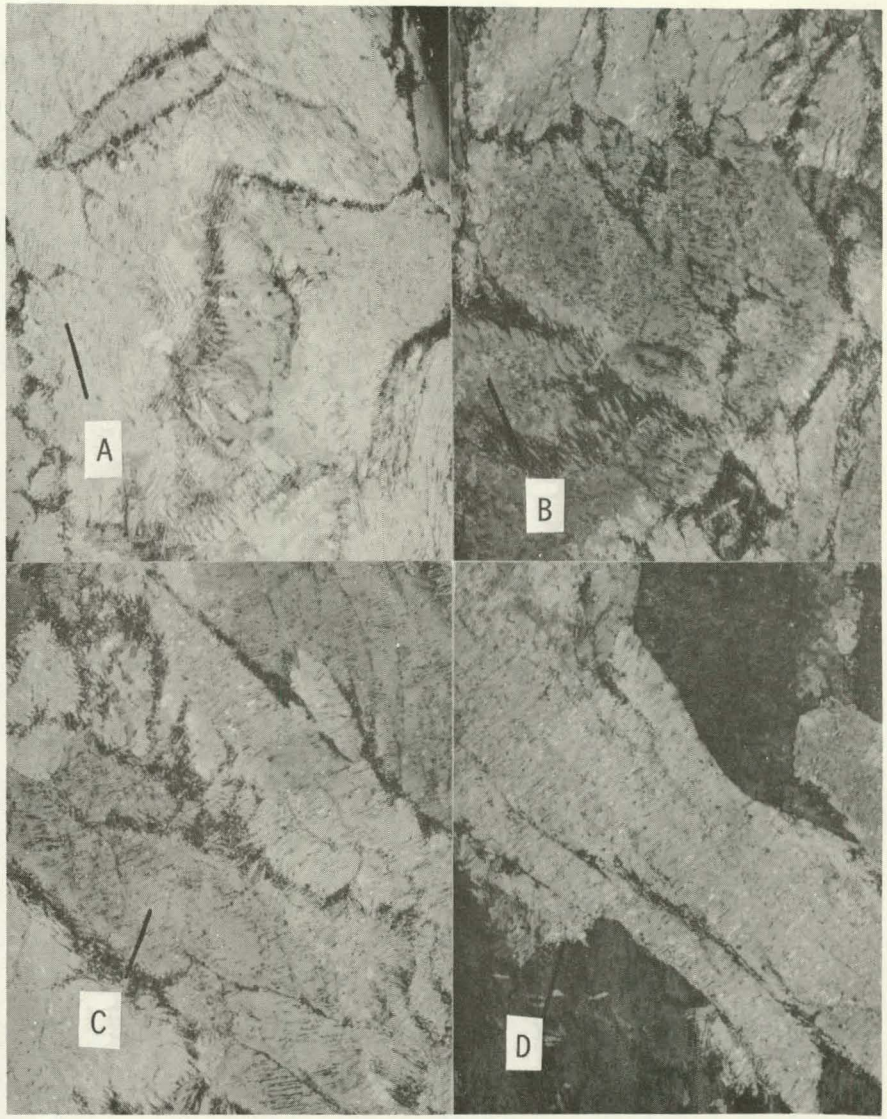

Fig. III.34. Microstructures of Regions Adjacent to Necks in Fig. III.32b That Show Unaligned Lenticular α' Plates. The direction of the hoop stress is indicated by the lines. Etched and anodized. Polarized light. Mag. ~150X. ANL Neg. No. 306-75-201.

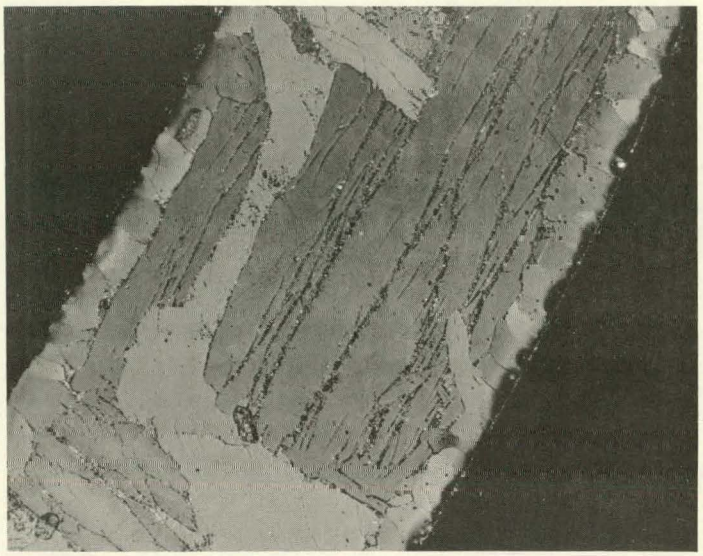

Fig. III.35

Microstructure of Undeformed Region of Oxidized and Homogenized Specimen Described in Figs. III.29–III.32 That Shows Lenticular α' Plates in an Orientation Conducive to Neck Formation. Etched and anodized. Polarized light. Mag. ~90X. ANL Neg. No. 306-75-219.

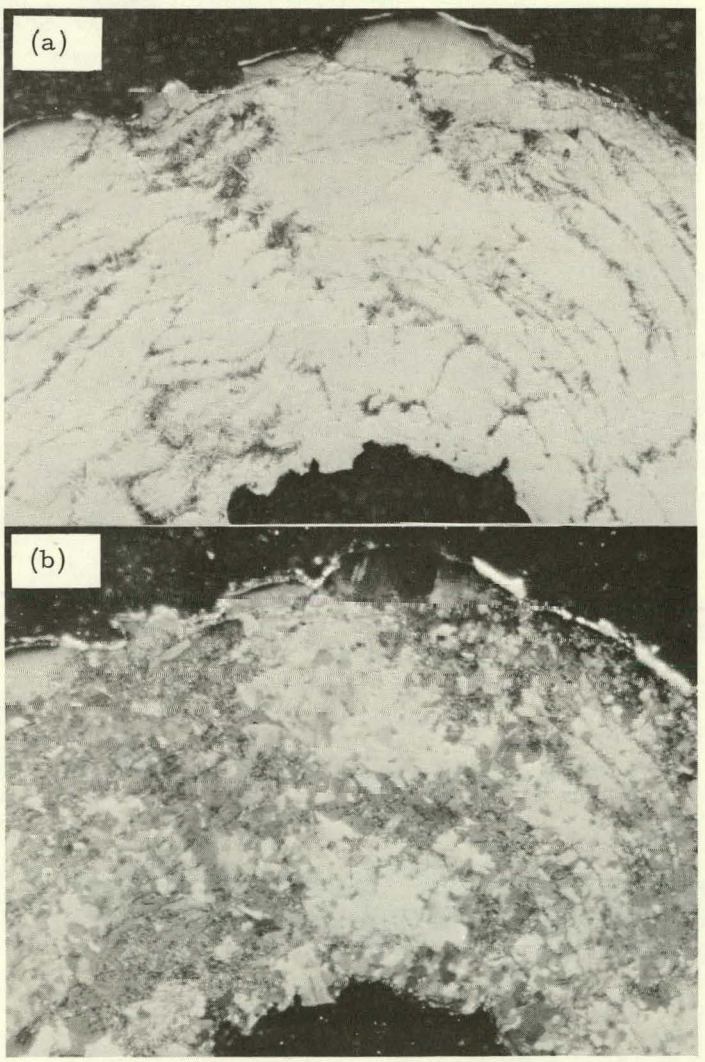

Fig. III.36

Microstructures of Oxidized and Homogenized Zircaloy-4 Specimen Containing 0.37 wt % Oxygen after Biaxial Rupture at 1015°C. Etched and anodized. Mag. ~180X. (a) Bright field, showing elongated previous α' grains. (b) Polarized light, showing recrystallized equiaxed α grains within previous α' grains. ANL Neg. No. 306-75-212.

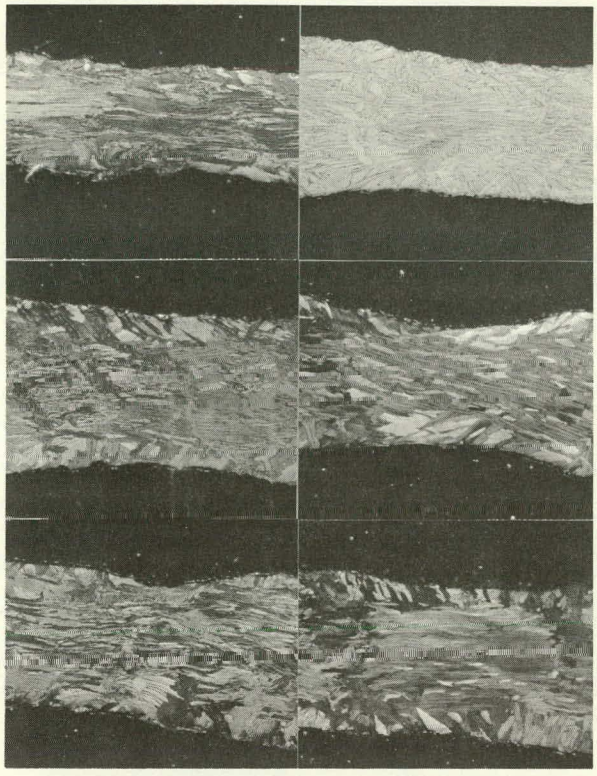

Fig. III.37. Microstructures of Necked Areas in a Zircaloy-4 Uniaxial Tensile Specimen Deformed at 700°C That Show Elongated $\beta \rightarrow \alpha'$ Transformed Grains Parallel to Load Direction. Etched and anodized. Polarized light. Mag. ~39X. ANL Neg. No. 306-75-211.

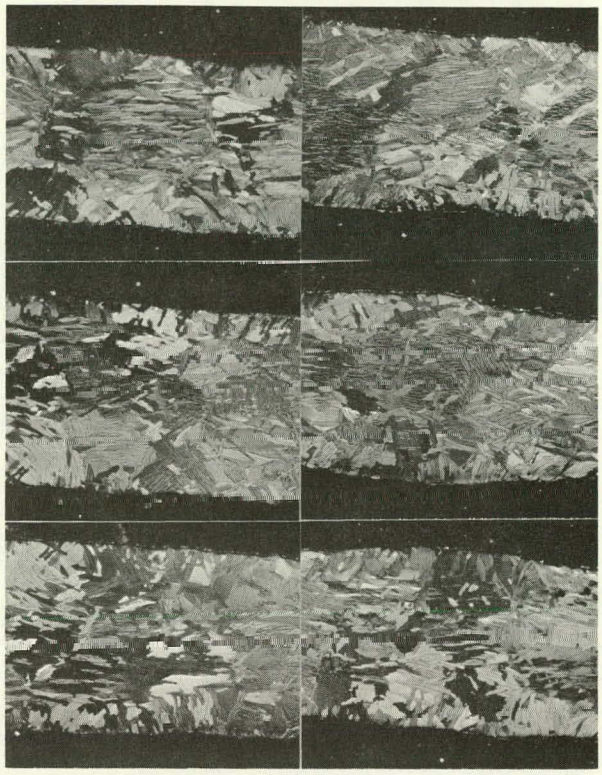

Fig. III.38. Microstructures of Unnecked Regions of Zircaloy-4 Tensile Specimen That Show Relatively Random Orientation of α' Grains with Respect to Load Direction. Etched and anodized. Polarized light. Mag. ~39X. ANL Neg. No. 306-75-210.

5. Evaluation of the Onset of Plastic Instability in Internally Pressurized Zircaloy Cladding

An understanding of the deformation process near the onset of plastic instability is essential to the development of a failure criterion for internally pressurized Zircaloy cladding. Several of the instability criteria proposed for thin-walled tubes under a biaxial state of stress[10-12] were compared with the experimental data obtained from the specimens shown in Fig. III.29.

The commonly accepted criterion of $dP = 0$, where P is the internal pressure, can be obtained from the pressure-transient curves in Fig. III.30. This criterion indicates the instability occurred ~2-3 s before rupture; however, examination of individual frames from the high-speed camera film revealed that uniform deformation extends considerably beyond this point. Figure III.39 shows individual frames of the oxidized and homogenized Zircaloy-4 tube at 0.004-s intervals. The image on the left of each photograph is a reflection from a mirror located behind the specimen.

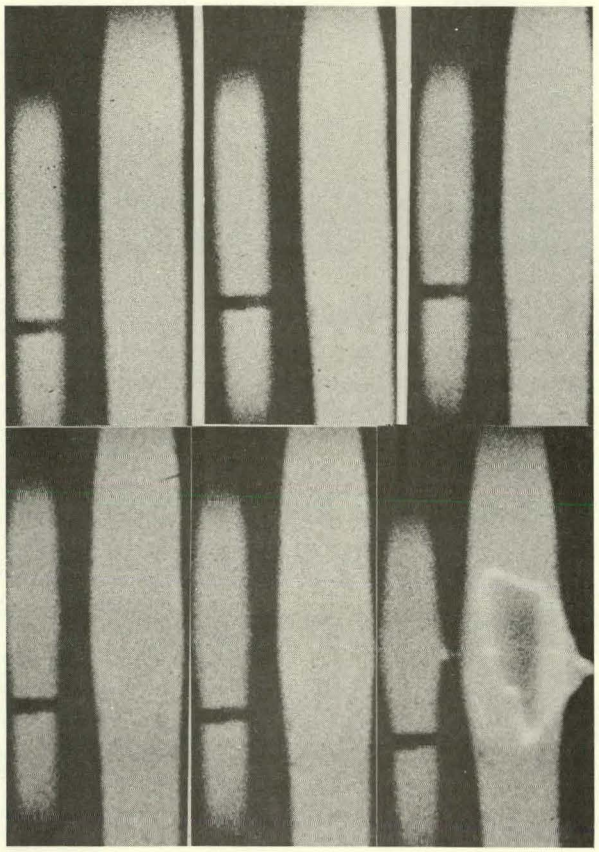

Fig. III.39. High-speed Movie Frames Taken during Deformation of Oxidized and Homogenized (0.37 wt % Oxygen) Zircaloy-4 Tube. The time interval between frames was 0.004 s. The photographs, from upper left to lower right, are 20, 10, 3, 2, 1, and 0 frames before rupture. Smaller tubes are mirror images at ~160° with respect to the main image. ANL Neg. No. 306-75-226.

Figure III.40 shows plots of the axial distribution of diametral strain that were constructed from four of the frames in Fig. III.39. Figure III.40 indicates that plastic instability occurred in the interval between 0.08 and 0.008 s before rupture. Hardy[4] also concluded that the dP = 0 criterion is met well before the onset of local ballooning of the fuel cladding.

Figure III.41 is a plot of the normalized tube diameter D/D_0, as a function of time, for the region of maximum local ballooning. The diametral strain rate, which was approximated from the slope of the diametral-strain plot, is also shown. The latter curve indicates that the strain rate is very high near the onset of instability.

Franklin[12] derived an instability relation for internally pressurized tubes, based upon the more accepted criterion

$$\frac{\delta \dot{A}}{\delta A} = 0, \qquad (2)$$

where A is the cross-sectional area of the tube at any instant during deformation, $\dot{A}$ is the rate of decrease of the cross-sectional area A, and δ refers to the difference between the parameters in the necked and unnecked regions of the specimen at the same time increment. The biaxial stability relation is

$$\frac{\delta \dot{\epsilon}_\theta + \delta \dot{\epsilon}_z}{\delta \epsilon_\theta + \delta \epsilon_z} \leq \dot{\epsilon}_\theta + \dot{\epsilon}_z \text{ (plastically stable)}, \qquad (3)$$

where ϵ_θ and ϵ_z are the tangential (hoop) and axial strains, respectively. If we consider the approximation that the axial strain and strain rate are negligible, when compared with corresponding quantities in the tangential direction, the stability relation can be written as

$$\frac{\delta \dot{\epsilon}_\theta}{\delta \epsilon_\theta} \lesssim \dot{\epsilon}_\theta, \qquad (4)$$

and, in terms of radial displacements, Eq. 4 becomes

$$\frac{\delta \dot{r}}{\dot{r}} \lesssim 2 \frac{\delta r}{r}. \tag{5}$$

To apply this stability criterion to the curves in Fig. III.41, we can define a normalized diametral strain parameter as

$$\epsilon_d = \frac{D}{D_0} = \frac{r}{r_0}, \tag{6}$$

and, combining Eqs. 5 and 6, we obtain

$$\delta \ln \dot{\epsilon}_d \lesssim 2\delta \ln \epsilon_d. \tag{7}$$

If we compare two axial locations on the tube separated by an infinitesimally small distance during the time increment dt, Eq. 7 can be written as

$$\frac{d \ln \dot{\epsilon}_d}{dt} \lesssim 2 \frac{d \ln \epsilon_d}{dt}, \tag{8}$$

and numerical values of both quantities can be computed from the curves in Fig. III.41. The solid and dashed lines in Fig. III.42 correspond to the terms on the left and right sides, respectively, of Eq. 8. The intersection of the two curves at ~0.038 s defines the onset of plastic instability in the tube, which is in reasonable agreement with the experimental results shown in Fig. III.39.

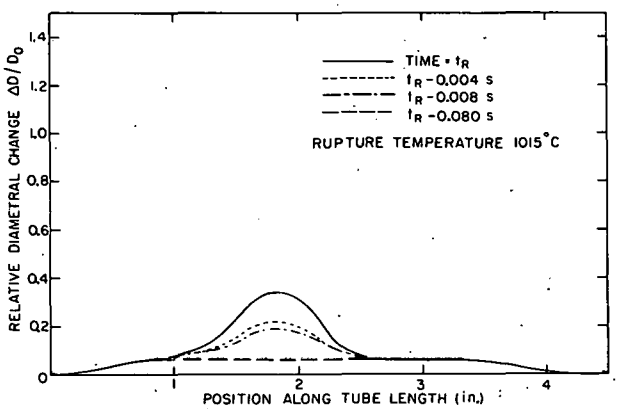

Fig. III.40. Diametral-strain Distribution in Zircaloy-4 Cladding Tube Described in Fig. III.39 near Onset of Plastic Instability and Rupture. ANL Neg. No. 306-75-214.

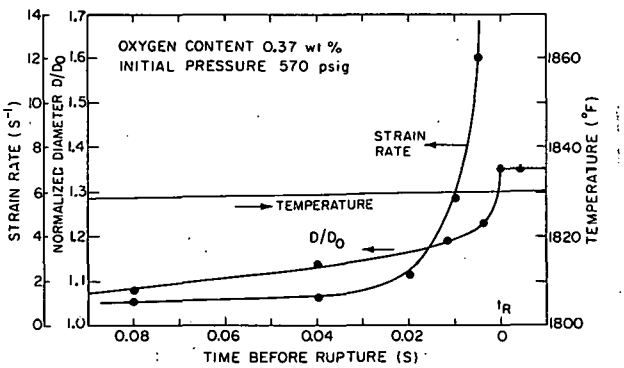

Fig. III.41. Diametral Strain, Strain Rate, and Temperature at Burst Region of Zircaloy-4 Specimen Shown in Fig. III.39, as a Function of Time near Onset of Plastic Instability. ANL Neg. No. 306-75-204.

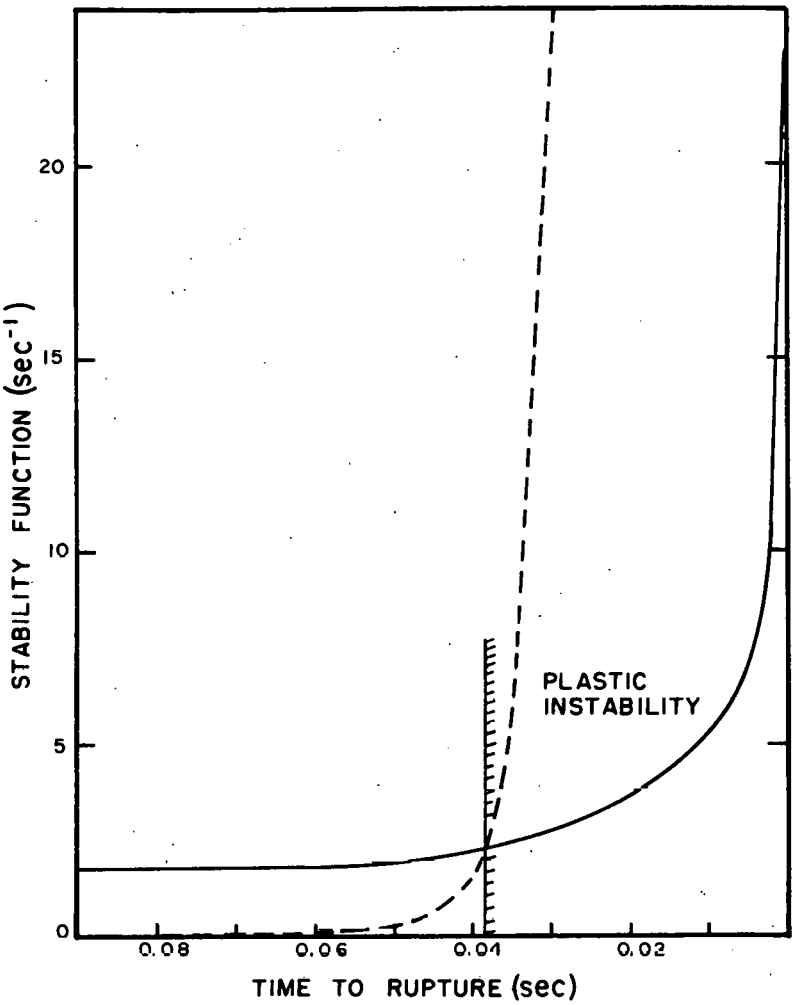

Fig. III.42. Stability Functions Calculated from Eq. 8 and Data in Fig. III.41 for Zircaloy-4 Rupture Specimen Described in Figs. III.39-III.41. ANL Neg. No. 306-75-225.

D. Determination of Oxygen Diffusion Coefficient in α-phase Zircaloy at High Temperature

The diffusion coefficient of oxygen in α-Zircaloy at temperatures above 900°C is an important parameter in the kinetics of oxidation, oxygen redistribution, and phase transformations--processes that can influence the strength and ductility of Zircaloy fuel cladding in postulated LOCA situations. Although the oxygen diffusivity in β-phase Zircaloy is essential in calculating oxygen-concentration gradients in the load-supporting β phase in fuel cladding during LOCA situations, the α-phase oxygen diffusivity is important in computing the α/β phase-boundary penetration and in determining the fractional β-phase thickness. A number of investigators have determined the oxygen diffusivity in α-phase zirconium and Zircaloy[13-19] at lower temperatures, but the measurements of Mallet et al.[20] are the only available data at temperatures above 900°C

The computer model developed for calculating isothermal oxidation and homogenization kinetics of finite-thickness Zircaloy material[1] was used to

investigate systematically the effect of uncertainties in several parameters on the kinetics of ZrO_2/α and α/β phase-boundary migration during oxidation and homogenization anneals. Recent information on the diffusion coefficient for oxygen in β-Zircaloy[21] and oxygen concentrations at the phase boundaries from the pseudobinary Zircaloy-oxygen system[1] were used in the computations. However, the results indicate that the kinetics of α/β phase-boundary migration was most sensitive to the oxygen diffusivity in α-Zircaloy. This implies that oxygen diffusion in α-Zircaloy is the rate-limiting step in the migration of the α/β interface.

The computer model was used in conjunction with the experimental measurements of α/β phase-boundary locations after various isothermal annealing times to obtain oxygen-diffusivity values at temperatures between 900 and 1300°C. After each annealing period, the sample was accurately weighed to ensure that oxygen contamination had not occurred since the computations were performed for a boundary condition that corresponds to an overall oxygen conservation within the specimen. Figures III.43-III.46 show the computed curves for the ZrO_2/α and α/β phase-boundary positions for different oxygen-diffusivity values and experimental data points. The α-phase oxygen-diffusivity value at each temperature was determined from the calculated curve that best fit the experimental data. The diffusion coefficients obtained in this manner are plotted against reciprocal temperature in Fig. III.47 along with the results of other investigators.[13-20] The present data are somewhat lower than the results of Mallet et al.[20] and yield an activation energy of ~51 kcal/mole, compared with the former value of ~41 kcal/mole.

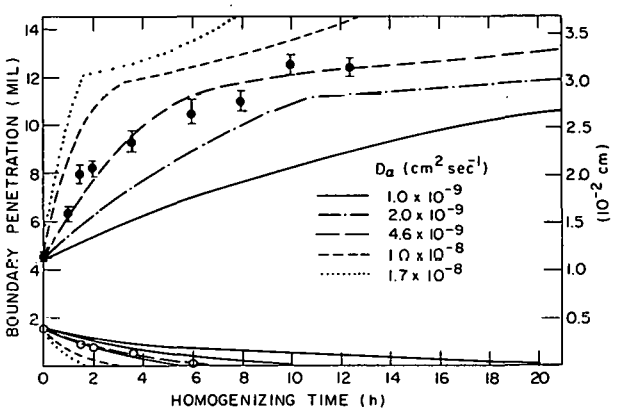

Fig. III.43. Comparison of Experimental and Calculated Locations of ZrO_2/α and α/β Phase Boundaries as a Function of Annealing Time in Vacuum at 1000°C. An oxygen diffusion coefficient of 4.6 x 10^{-9} cm^2 s^{-1} in α-Zircaloy provides the best fit to the experimental data for the ZrO_2/α (lower curve) and α/β (upper curve) phase-boundary locations. ANL Neg. No. 306-75-221.

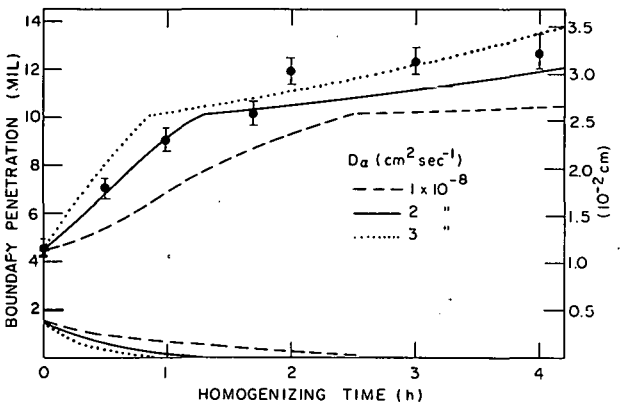

Fig. III.44. Comparison of Experimental and Calculated Locations of ZrO_2/α and α/β Phase Boundaries as a Function of Annealing Time in Vacuum at 1100°C. An oxygen diffusion coefficient of 2.3 x 10^{-8} cm^2 s^{-1} in α-Zircaloy provides the best fit to the experimental data for the ZrO_2/α (lower curve) and α/β (upper curve) phase-boundary locations. ANL Neg. No. 306-75-213.

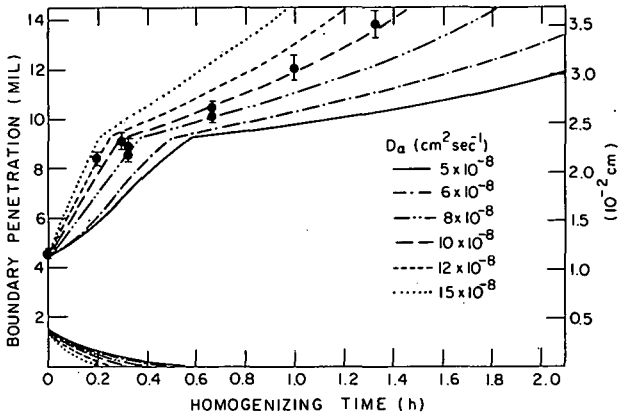

Fig. III.45. Comparison of Experimental and Calculated Locations of ZrO_2/α and α/β Phase Boundaries as a Function of Annealing Time in Vacuum at 1200°C. An oxygen diffusion coefficient of 1×10^{-7} cm^2 s^{-1} in α-Zircaloy provides the best fit to the experimental data for the ZrO_2/α (lower curve) and α/β (upper curve) phase-boundary locations. ANL Neg. No. 306-75-223.

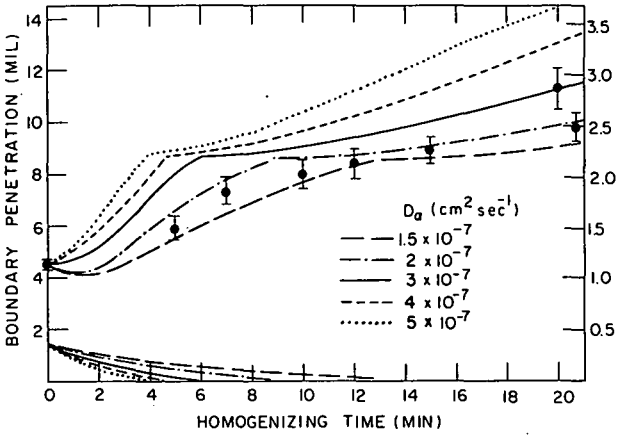

Fig. III.46. Comparison of Experimental and Calculated Locations of ZrO_2/α and α/β Phase Boundaries as a Function of Annealing Time in Vacuum at 1300°C. An oxygen diffusion coefficient of 2×10^{-7} cm^2 s^{-1} in α-Zircaloy provides the best fit to the experimental data for the ZrO_2/α (lower curve) and α/β (upper curve) phase-boundary locations. ANL Neg. No. 306-75-222.

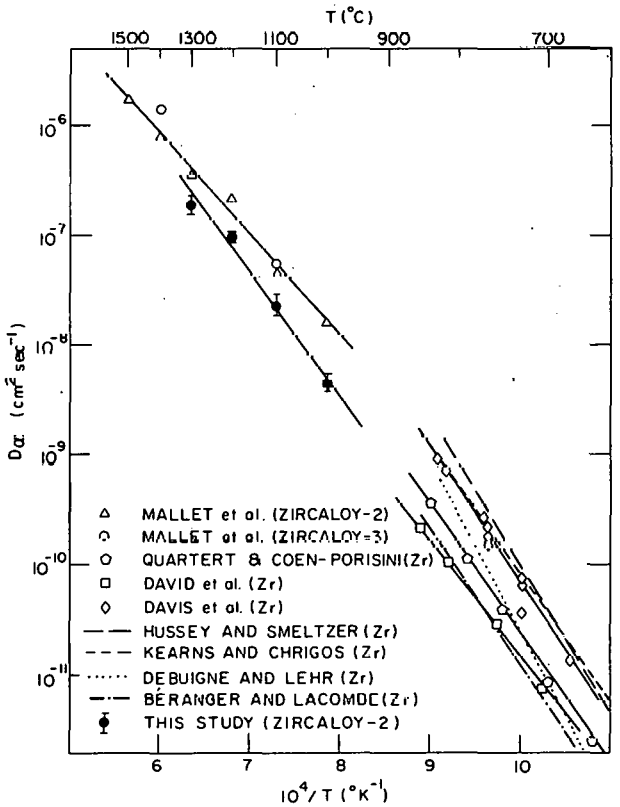

Fig. III.47

Temperature Dependence of Diffusion Coefficient of Oxygen in α-phase Zircaloy Obtained from Results in Figs. III.43-III.46. Results of other investigators[13-21] are shown for comparison. ANL Neg. No. 306-75-216.

Note that empirical relationships, which do not require values for oxygen diffusivity in α-Zircaloy, may be satisfactory for describing α/β phase-boundary penetration during transient oxidation conditions. However, diffusivity values are required in an analysis of oxygen redistribution that can occur during cooling through the $\beta \rightarrow \alpha'$ transition at different rates.

E. Preparation of α-phase and Composite Zircaloy-Oxygen Alloys

The following factors must be considered in an experimental method for producing α-phase and composite mechanical-test specimens: (1) the phases present, (2) the oxygen concentration gradient, (3) the grain size and morphology, (4) the extent of the redistribution of alloying elements such as oxygen, iron, and chromium during cooling, and (5) the density and distribution of second-phase particles. Because of the comparatively small oxygen diffusivity in α-Zircaloy, the preparation of α-phase mechanical-property specimens with different oxygen concentrations and gradients will involve long annealing periods. It is therefore desirable to maximize the efficiency of specimen preparation by calculating the optimum oxidation and homogenization conditions, i.e., the times and temperatures.

1. Equiaxed α-phase Specimens with Low Oxygen Concentrations

When oxidation or homogenization of Zircaloy specimens is undertaken above ~900°C, part of the specimen inevitably transforms to β phase and rapid grain growth occurs. In this case, the final α-grain size is controlled by the size of the previous β grains. To avoid the problem, the oxidation and homogenization processes must be performed at temperatures below the $\alpha/(\alpha + \beta)$ phase boundary.

The computer code (see Sec. D) was used to determine the optimum times and temperatures (see Table III.8) for oxidation and homogenization to produce equiaxed α specimens containing 0.2-1.5 wt % oxygen. The expected average grain size, obtained by extrapolating results from the 20- to 35-day anneals at 800°C, is also reported. During the long homogenization periods, second-phase particles migrate and coalesce preferentially at grain boundaries. Although the maximum size of the precipitates in as-received Zircaloy-4 was ~1-2 μm, precipitates as large as ~6-8 μm were observed after 21 days at 815°C in an alloy containing 0.5 wt % oxygen.

2. Equiaxed α-phase Specimens with High Oxygen Concentrations

Since α-phase specimens with oxygen concentrations >2 wt % will be extremely brittle, the effect of larger grain size on the mechanical properties may be comparatively small. Thus, except for a few specimens that will be produced by oxidation and homogenization at 800°C, most of the specimens will be prepared by an optimum combination of oxidation and homogenization anneals at higher temperatures. This will afford a reduction in

annealing time from 60-100 days to <24 h. The production schemes for oxygen concentrations of 2, 2.5, 3, 4, and 5 wt % are shown in Figs. III.48-III.52. The oxidation and homogenization conditions are given in the insets, which also show the concentration profiles at several times, including the one for completion of the diffusion anneal.

TABLE III.8. Summary of Oxidation and Homogenization Conditions Required to Produce α-phase Specimens with Uniform Oxygen Concentrations[a]

C, wt %	T_C, °C	t_c, min	T_H, °C	t_H^o, h	t_H, days	G, μm
0.2	700	1.5	800	8.4	27.4	35
0.3	700	5.0	800	11.3	32.5	37
0.4	700	12.0	800	14.2	36.6	39
0.5	800	6.0	800	16.8	38.7	40
0.6	800	9.6	800	19.7	40.7	41
0.7	800	13.7	800	22.6	42.0	41
0.9	800	18.8	800	25.9	44.1	42
1.0	800	31.2	800	33.4	45.3	42
1.1	800	38.8	800	37.9	47.2	43
1.2	800	46.9	800	42.7	47.8	43
1.3	800	56.0	800	48.2	49.3	43
1.4	800	65.6	800	54.5	50.3	44
1.5	800	76.4	800	61.7	51.6	44

[a] C = desired uniform oxygen concentration; T_C = oxidation temperature; t_c = oxidation time; T_H = homogenization temperature; t_H^o = homogenization time required to eliminate oxide layer; t_H = time of 99% homogenization; and G = expected final average grain size.

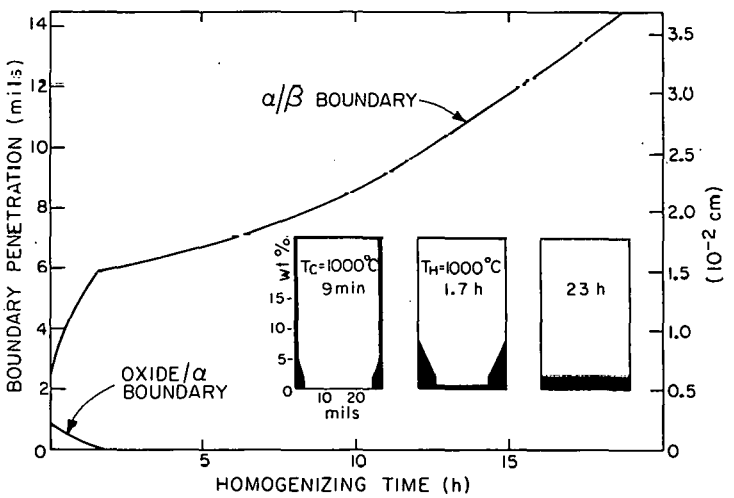

Fig. III.48

Calculated ZrO_2/α and α/β Phase-boundary Locations during Homogenization of Composite Specimen Containing 2 wt % Oxygen in Vacuum at 1000°C. ANL Neg. No. 306-75-227.

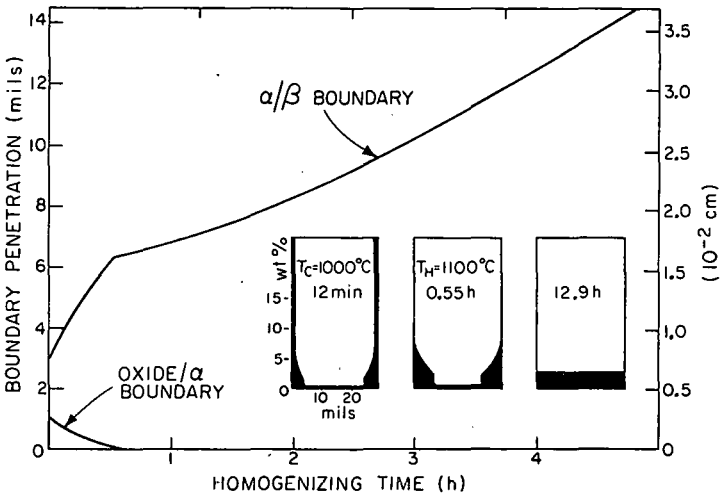

Fig. III.49

Calculated ZrO_2/α and α/β Phase-boundary Locations during Homogenization of Composite Specimen Containing 2.5 wt % Oxygen in Vacuum at 1100°C. ANL Neg. No. 306-75-220.

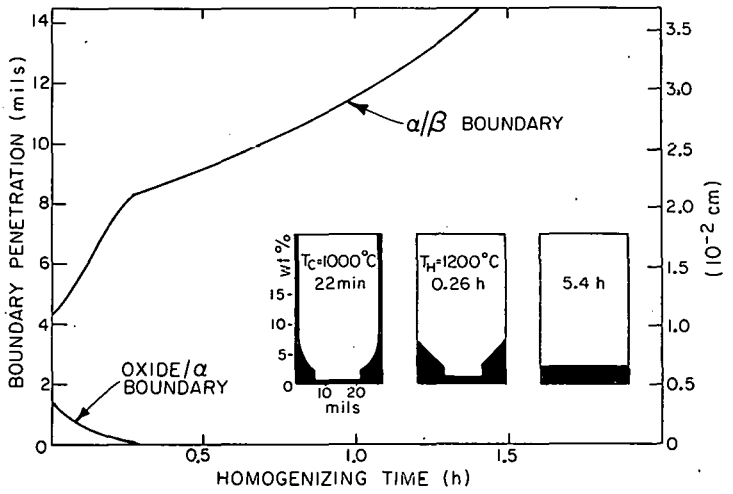

Fig. III.50

Calculated ZrO_2/α and α/β Phase-boundary Locations during Homogenization of Composite Specimen Containing 3 wt % Oxygen in Vacuum at 1200°C. ANL Neg. No. 306-75-206.

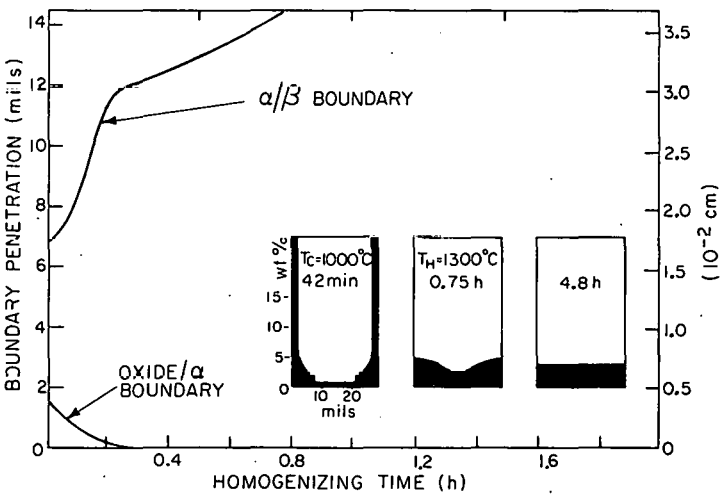

Fig. III.51

Calculated ZrO_2/α and α/β Phase-boundary Locations during Homogenization of Composite Specimen Containing 4 wt % Oxygen in Vacuum at 1300°C. ANL Neg. No. 306-75-207.

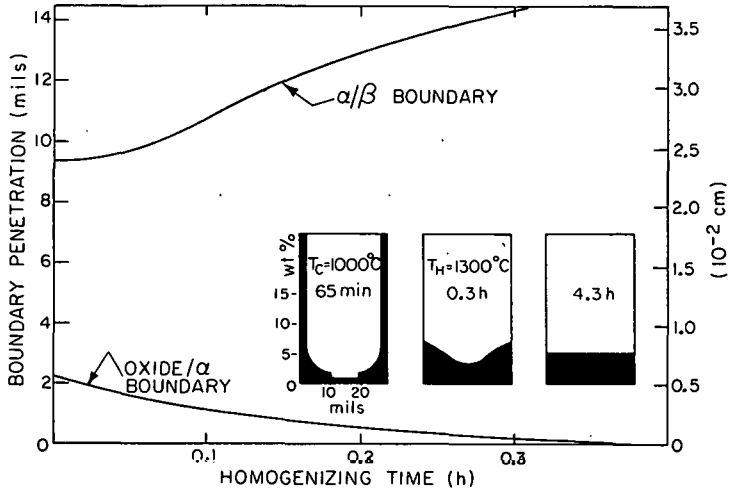

Fig. III.52

Calculated ZrO_2/α and α/β Phase-boundary Locations during Homogenization of Composite Specimen Containing 5 wt % Oxygen in Vacuum at 1300°C. ANL Neg. No. 306-75-218.

3. $ZrO_2/\alpha/\beta$ Composite Specimens

The fractional thickness of the oxide, α, and β phases after oxidation at a given temperature are interdependent. However, if oxidation is combined with a partial homogenization before actual deformation, it is possible to achieve a range for the relative thicknesses of the three phases. The fractional thickness of the β phase in the composite specimen is of most interest. The curves for isothermal homogenization in Figs. III.48-III.52 can serve as a guide in adjusting the values during a short annealing period at a given test temperature. For example, to conduct a uniaxial tensile test on an α/β composite specimen with a fractional β-phase thickness of 0.5 at 1000°C, the procedure would involve (a) oxidation for 9 min at 1000°C, (b) vacuum annealing at 1000°C for ~7.5 h, and (c) deforming the specimen at 1000°C with a minimum hold time. A composite specimen with an oxygen gradient in the central β-phase region at temperatures above 1200°C will be difficult to test, because the high oxygen diffusivity will result in virtual saturation of the β phase during the first several minutes at temperature. Therefore, simultaneous oxidation and deformation at high strain rates offer a practical solution to this problem.

References

1. Light-water-reactor Safety Research Program: Quarterly Progress Report, April-June 1975, Sec. III, "Mechanical Properties of Zircaloy Containing Oxygen," ANL-75-58 (Sept 26, 1975).

2. D. O. Hobson, M. F. Osborne, and G. W. Parker, Comparison of Rupture Data from Irradiated Fuel Rods and Unirradiated Cladding, Nucl. Tech. 11, 479 (1971).

3. D. O. Hobson and P. L. Rittenhouse, Deformation and Rupture Behavior of Light-water Reactor Fuel Cladding, ORNL-4727 (Oct 1971).

4. D. G. Hardy, High Temperature Expansion and Rupture Behavior of Zircaloy Tubing, Topical Meeting on Water-reactor Safety, Salt Lake City, Utah, March 26-28, 1973, G. A. Freund Compiler, pp. 254-273.

5. C. C. Busby and K. B. Marsh, High Temperature Deformation and Burst Characteristics of Recrystallized Zircaloy-4 Tubing, WAPD-TM-900 (Jan 1970).

6. G. Östberg, Metallographic Study of Isothermal Transformation of Beta Phase in Zircaloy-2, Jernkontorets Ann. 145, 119 (1963).

7. G. Östberg, Determination of the Composition of the Second Phase in Zircaloy, J. Nucl. Mater. 7, 103 (1962).

8. M. Bŏcek, Kernforschungszentrum Karlsruhe, Institute für Material und Festkörperforschung, West Germany, private communication (May 1975).

9. G. Hörz, M. Hammel, and H. Kanbach, Electrical Resistivity of β-Zirconium-Oxygen Solid Solutions as a Function of Oxygen Concentration and Temperature, J. Nucl. Mater. 55, 291 (1975).

10. W. T. Lankford and E. Saibel, Some Problems in Unstable Plastic Flow Under Biaxial Tension, Trans. AIME 171, 562 (1947).

11. F. L. Yaggee and Che-Yu Li, Failure Mechanisms for Internally Pressurized Thin-Wall Tubes and Their Relationship to Fuel-Element Failure Criteria, ANL-7805 (Dec 1972).

12. D. Franklin, Theory of Plastic Instability in Thin-Wall Tubes, Acta. Met. 20, 839 (1972).

13. M. Davis, K. R. Montgomery, and J. Standring, The Diffusion Coefficient for Oxygen in Alpha-Zirconium, J. Inst. Metals 89, 172 (1961).

14. J. J. Kearns and J. N. Chrigos, The Use of Microhardness in the Determination of the Diffusivity of Oxygen in Alpha Zirconium, WAPD-TM-306 (Feb 1962).

15. J. Debuigne and P. Lehr, Etude de l'Oxydation du Zirconium non Allié et de la Diffusion de l'Oxygène dans la Couche d'Oxyde et dans le Métal, Rev. Met. Memoires 60, 911 (1963).

16. R. J. Hussey and W. W. Smeltzer, The Mechanism of Oxidation of Zirconium in the Temperature Range 400°-850°C, J. Electrochem. Soc. 111, 1221 (1964).

17. G. Beranger and P. Lacombe, Contribution a l'Etude de la Cinetigue de l'Oxydation du Zirconium α et de la Diffusion de l'Oxygene dans le Metal Sous-Jacent a l'Oxyde, J. Nucl. Mater. 16, 190 (1965).

18. D. Quartet and F. Coen-Porsini, Utilization of the Ion Analyzer for the Study of Oxygen Diffusion in Solids and Its Application to Zirconium, J. Nucl. Mater. 36, 20 (1970).

19. D. David, G. Amsel, P. Boisot, and G. Beranger, A Study of the Diffusion of Oxygen in Alpha-Zirconium by Means of Nuclear Microanalysis, J. Electrochem. Soc. 122, 388 (1975).

20. M. W. Mallet, W. M. Albrecht, and P. R. Wilson, The Diffusion of Oxygen in Alpha and Beta Zircaloy-2 and Zircaloy-3 at High Temperatures, J. Electrochem. Soc. 106, 181 (1959). See also BMI-1154 (1957).

21. Light-water-reactor Safety Research Program: Quarterly Progress Report on Reactor Safety Programs, Sec. IV, "Zirconium Metal-water Oxidation Kinetics," ORNL-TM-5021 (Sept 1975).

APPENDIX

Kinetics of Fission Gas and Volatile Fission-product Behavior under Transient Conditions in LWR Fuel (Claudio Ronchi*)

Recent intensified emphasis in reactor-safety requirements for light-water reactors (LWR's) has given added impetus to studies of the behavior of fuel under conditions anticipated in hypothetical reactor accidents.

Fission-product swelling and release are two important aspects in the development of a reactor accident, and their understanding and description represent one of the basic steps in the accident analysis.

Therefore, the fission-gas behavior code GRASS has recently been adapted to describe in-reactor transient situations. However, extension and fitting of the steady-state formalism to these specific cases require a careful evaluation of the basic assumptions of the model, and furthermore, experiments are needed to verify both the input and output parameters of the code.

Some problems that arise from the application of GRASS to transient conditions are discussed and solutions suggested here. In particular, an extension of the model is proposed that will take into account the behavior of a wider variety of features so that the analytical results can be closely correlated with the microstructural changes produced during irradiation and during in-reactor and direct-electrical-heating (DEH) simulated transients.

A model for volatile fission-product behavior is proposed that will enable both steady-state and transient release to be evaluated.

1. Limit of Validity of the GRASS Basic Equations in Transient Conditions

a. Probability of Fission-gas Bubble Coalescence

The model calculates fission-gas swelling based on successive coalescence processes between bubbles, starting from a system of equations that describe the time rate of change of the bubble concentrations; i.e.,

$$\dot{c}_k = \sum_{i+j=k} (P_{ij} c_i c_j) - \sum_{j \neq k} (P_{kj} c_k c_j) - P_{kk} c_k c_k, \qquad (1)$$

where c_k is the concentration of the bubbles containing k atoms. The tensor P^{ij} represents the encountering probability of two bubbles of i and j atoms. This is calculated on the basis of a diffusion model[1] and is given by

*Visiting Scientist from EURATOM, European Transuranium Institute, Karlsruhe, Germany.

$$P_{ij} = 4\pi D_{ik} R_{ik} \left(1 + \frac{R_{ik}}{\sqrt{\pi D_{ik} t}}\right), \tag{2}$$

where

t = time,

$D_{ik} = D_i + D_k$ (D_i and D_k = bubble diffusion coefficients),

and

$R_{ik} = R_i + R_k$ (R_i and R_k = bubble radii).

Equation 2 is the extension of the capture probability of a diffusing species j by a precipitation center i to the case where i is also subjected to Brownian motion. The precipitation equation used in Ref. 1 was

$$\frac{\partial c_j}{\partial t} = D\Delta^2 c_j, \tag{3}$$

with

$c_j = c_0$ for $t = 0$ $r > R_{ij}$,

$c_j = 0$ for $t > 0$ $r = R_{ij}$,

which gives, from its solution integral,

$$\left|\vec{J}\right|_\Sigma = 4\pi R_{ij}^2 D \left(\frac{\partial c_j}{\partial r}\right)_{R_{ij}} = 4\pi D R_{ij} \left(1 + \frac{R_{ij}}{\sqrt{\pi D t}}\right) c_0. \tag{4}$$

Equation 3 is approximately correct only for the case in which the concentration of the species i is so low that the effect of the surrounding precipitation centers is negligible or in which no large variations of the concentrations of i and j occur during the time step considered (e.g., in steady-state conditions). But this is certainly not true for a temperature transient where strong bubble concentration variations occur in relatively short times. In this case, a more correct formulation of Eq. 3 must be made by taking into account that each center of precipitation i has a finite sphere of influence which has a radius R_s with

$$\tfrac{4}{3}\pi R_s^3 = \frac{1}{c_i}. \tag{5}$$

Hence, in Eq. 3, the additional boundary condition

$$\frac{\partial c_j}{\partial r} = 0 \quad \text{at } r = R_s \quad \text{for } t > 0 \tag{6}$$

must be included. The expression of J now becomes[2]

$$|\vec{J}|_{\Sigma} \approx 4\pi D R_{ij} c_0 \exp(-t/\tau_0) + \epsilon(t), \tag{7}$$

with

$$r_0 = R_s^3/3R_{ij}D. \tag{8}$$

For $t \to \infty$, Eq. 7 fundamentally deviates from Eq. 3; J tends now to zero, and this is the logical consequence of the fact that the concentration of j in a finite nonzero sphere of influence decreases more rapidly than in a zero sphere of influence.

However, in the assumed mathematical formalism it is important that, in each integration step required to solve Eq. 1, the coefficients P_{ik} do not vary with time (or, in other words, that no implicit variation of c_k occurs during the integration step). Now Eq. 7 furnishes a criterion for the selection of the amplitude Δt of the integration step to obtain a certain precision δ

$$\frac{\Delta t}{\tau_0} \leq \delta. \tag{9}$$

Relationship 9 must be verified only for the highest-density bubble population (usually single gas atoms); for the other size classes the condition is satisfied "a fortiori."

b. Bubble-growth Regime in Short Times

In the steady-state model, the assumption that fission-gas bubbles are constantly in equilibrium with the surrounding lattice is reasonable, considering the long times involved. In transient situations this hypothesis is questionable. Gas-precipitation (or bubble-encountering) processes define a metastable initial state for the bubbles, which subsequently grow at a finite rate toward their equilibrium size. The growth stage (coalescence process) is physically characterized by a net flow of lattice vacancies through the bubble surface under the driving force of the stress field generated by the nonequilibrium configuration. The driving force $\overline{F}$ is expressed as

$$\overline{F} = \Omega^v \frac{\partial \sigma_{rr}}{\partial r}, \tag{10}$$

where $\partial\sigma_{rr}/\partial r$ is the radial stress gradient, and Ω^v is the lattice volume. When the concentration of vacancies is in thermodynamical equilibrium, the rate of increase of the bubble radius is

$$\frac{dR}{dt} = \frac{D_v^{self}}{kT}\left(\frac{\partial\sigma_{rr}}{\partial r}\right)_{r=R}\Omega^v, \tag{11}$$

where D_v is the self-diffusion coefficient of the lattice vacancies. Since σ_{rr} is given by

$$\sigma_{rr} = -\frac{\mu\, dV}{\pi}\, r^{-3}, \tag{12}$$

where μ is the shear modulus and dV is the volume difference from the equilibrium configuration, it follows that

$$\left(\frac{\partial\sigma_{rr}}{\partial r}\right)_{r=R} = \frac{3\mu\, dV}{\pi} R^{-4}. \tag{13}$$

For a coalescence event between two bubbles with radii R_0 and R_1 and containing a perfect gas, dV is

$$dV = V_0 \quad V(t) = \tfrac{4}{3}\pi\left[(R_0^2 + R_1^2)^{3/2} - R^3(t)\right]. \tag{14}$$

From Eq. 13, one sees that the driving force for the bubble coalescence growth decreases proportionally to the volume deviation from the equilibrium size and is inversely proportional to the fourth power of the bubble radius. Since dV is roughly proportional to R^2, the bubble-growth rate should decrease with R^{-2}. However, the order of magnitude of R is mainly determined by D_v, and this quantity must be evaluated as a function of local fuel stoichiometry.

c. Inclusion of the Growth-rate Equations in GRASS for Transient Calculations

In the GRASS formalism, the bubble population is subdivided into several classes, each characterized by the number of atoms contained in the individual bubbles. Each bubble radius is calculated by applying a suitable equation of state for the gas. Inclusion of Eq. 11 in GRASS will complicate this calculation, and simplifications must be made to maintain a reasonably short computer calculation time. The following path gives a possible solution of the problem:

(1) An integration step Δt must first be defined for Eq. 1, according to the criterion described by Eq. 9.

(2) For each bubble class n that has N elements and an equilibrium radius R_0^n, the population increment ΔN is considered, as a result of the coalescence events, in Δt. The subclass Δn formed by ΔN elements has an initial mean radius determined by the average of the different coalescence processes; i.e.,

$$\bar{R}^{\Delta n} = \sum_{i+k=n} \left(\frac{P_{ik} R_{ik}}{\Sigma P_{ik}} \Delta t + \dot{R}_{ik} \frac{\Delta t}{2} \right), \tag{15}$$

with

$$R_{ik} = (R_i^3 + R_k^3)^{1/3}$$

where $\dot{R}_{ik}$ is calculated from Eqs. 11 and 13. Thus, an average radius can be calculated for the class n with $N + \Delta N$ elements

$$R_1^n = (NR_0^n + \bar{R}^{\Delta n} \Delta N)/(N + \Delta N). \tag{16}$$

(3) During the next integration step Δt, the average radius R_1^n will increase according to the rule

$$R_1^{n'} \approx R_1^n + \dot{R}_1^n \Delta t. \tag{17}$$

Meanwhile, new bubbles are produced in the class n by coalescences that occur in the second time step, so that the average radius R_2^n will be given again by Eq. 16, where $R_1^{n'}$ is substituted for R_0^n. Iterative calculation of Eqs. 15 and 16 enables the nonequilibrium radius R_k^n to be determined for each n as a function of the transient time t_k.

2. Fission-gas Release and Intergranular Pore Behavior

One assumption made in GRASS is that the bubbles or gas atoms arriving at the grain edges are directly released from the fuel column. This hypothesis is only true if the pores on the grain edges are completely interconnected or if they are sufficiently mobile to carry the gas to a central hole in a relatively short time. These conditions are reasonably met in LMFBR fuels, but not in standard LWR pellets, where the low operating temperatures and the in-reactor sintering processes lead to a relatively high retention of gas in the sintered pores. The amounts of fission gas and volatile fission products trapped in the intergranular macroporosity (with sizes above ~1 μm) are believed to be largely responsible for the burst processes that occur during fuel temperature excursions. A more detailed treatment of the intergranular behavior of the fission products is therefore required in LWR fuel modeling.

a. Definition and Evaluation of the Pore-interlinkage Parameter

In recent years, an effort has been made to establish a correlation between pore interlinkage and fuel structural features. However, this work has brought few practical advantages, because the geometrical models assumed were generally rather complicated and eventually of little significance in concrete applications. Therefore we think that more simple models, which take into account the actual statistical distribution of the structural features, are more reliable and convenient in release calculations. The most general approach to the definition of the concept of interlinkage is that of the mathematical percolation theory. Assuming a certain space distribution of "sites" connected with "bonds" randomly distributed with a concentration

$$P = \frac{\text{number of bonds}}{\text{number of sites}},$$

interlinkage is thought to occur when a finite probability can be calculated for an infinite chain of bonds starting from a given site.

Based on the macroscopic parameter P, it can be shown[3] that the probability that a site has n bonds is given by

$$P_n = e^{-P} \sum_{k}^{\infty} \frac{P^k}{k!}, \tag{18}$$

with

$$\sum_{n}^{\infty} P_n = P,$$

and the number of chains with N bonds is given by

$$\bar{n}(N, P) = \left(\sum_{n} \frac{P_n}{\sum_{n'} P_{n'}} \cdot \sum_{n'' \neq n} P_{n''} \right)^N. \tag{19}$$

The percolation condition is thus

$$\bar{n}(N, P) \to \epsilon > 0 \quad \text{for } N \to \infty, \tag{20}$$

which is verified for every

$$P \geq 1.569 \ldots,$$

i.e., when each site has to accommodate 1.6 or more bonds on the average, with its neighbors. In our case, the problem is to find a practical way of evaluating P for pores in a sintered medium. Assuming that the pores are distributed as spheres of radius r_p among grains of radius r_g, the average number of bonds per pore can be calculated as

$$P = \tfrac{1}{2}Nn_p + n_g N_p/N_g, \tag{21}$$

where n_p and n_g are the concentrations of pores and grains, respectively, N_p is the coordination number for a compact arrangement of pores ($N_p \approx 12$), and N_g is the coordination number of an arrangement of spheres of radius r_g around spheres of radius r_p. We can estimate N_g approximately from lattice geometry as

$$N_g \approx \frac{\pi}{2} \frac{1}{1 - \sqrt{1 - [g/(1+g)]^2}} \tag{22}$$

with

$$g = \frac{r_g}{r_p}.$$

In Eq. 21, n_p and n_g can be expressed as a function of the fractional porosity F and the parameter g, obtaining

$$P = \tfrac{1}{2}N_p \left\{ 1 + (F^{-1} - 1) \frac{2N_p}{\pi} \frac{\left[1 - \sqrt{1 - \left(\frac{g}{1+g} \right)^2} \right]}{g^3} \right\}^{-1}, \tag{23}$$

which enables P to be calculated from the two experimental parameters F and g and from the geometrical factor N_p. A first crude assumption would be to consider the condition $P > 1.56$ as the abrupt limit for intergranular release through percolation. Actually, P is a function of erratic structural parameters, depending on the local fuel condition and heterogeneity. Therefore, a statistical distribution around an average value of P must be assumed. In this case, one obtains

$$\text{pore interlinkage fraction} = F_\infty = \frac{1}{\sigma\sqrt{2\pi}} \int_{P_c=1.57}^{\infty} \exp[-(x - P)^2/2\sigma^2]dx, \tag{24}$$

where σ must be calculated from the experimental histograms of r_p, r_g, and F,

$$\sigma = \sqrt{\left(\frac{\partial P}{\partial r_b}\sigma_{r_p} + \frac{\partial P}{\partial r_g}\sigma_{r_g}\right)^2 + \left(\frac{\partial P}{\partial F}\sigma_F\right)^2}, \tag{25}$$

where the measures of r_p and r_g are assumed to be correlated and F to be orthogonal. Finally, we obtain

$$\sigma = \sqrt{B^2 g^2 \left(\sigma^f_{r_g} - \sigma^f_{r_p}\right)^2 + \frac{A^2}{F^2}\left(\sigma^f_F\right)^2}, \tag{26}$$

where the σ^f's of r_g, r_p, and F are fractional and P is absolute. A and B are given by

$$A = \frac{N_p^2}{\pi g^3}\left[1 - \sqrt{1 - \left(\frac{g}{1+g}\right)^2}\right]\left\{1 + \frac{F^{-1} - 1}{g^3}\,\frac{2N_p}{\pi}\left[1 - \sqrt{1 - \left(\frac{g}{1+g}\right)^2}\right]\right\}^{-2}$$

and

$$B = -\frac{N_p^2(F^{-1} - 1)}{\pi g^4(1+g)}\left[g\left(1 - \frac{1}{\sqrt{1+2g}}\right) - \left(1 - \frac{\sqrt{1+2g}}{1+g}\right)(3+4g)\right]$$

$$\cdot\left[1 + (F^{-1} - 1)\frac{2N_p}{\pi}\,\frac{1 + g - \sqrt{1+2g}}{g^3(1+g)}\right]^2. \tag{27}$$

b. Extension of GRASS with a Percolation Model for Release and Swelling

With the local fraction of open porosity known, a more precise description of intergranular swelling and release can be made. The following path must be maintained in the computer code:

(1) An initial distribution of pore and grain size is taken as input. This distribution must be measured by an accurate quantitative ceramographic analysis of the starting material.

(2) Suitable subroutines for grain growth and in-reactor sintering must calculate the modification of the initial structural parameters during the irradiation time.

(3) The pores are considered as partial traps for the gas. The fraction of gas released will be F_∞; the fraction retained in the pores will be $1 - F_\infty$.

(4) The gas trapped increases the pore volume according to the simple equation of state

$$nRT = \tfrac{4}{3}\pi r_p^3 \sigma_h, \tag{28}$$

where σ_h is the external hydrostatic stress. The capillarity forces can be neglected in the pore size range.

(5) Only the open porosity fraction F_∞ must be considered as recoverable by hot pressing and in-reactor sintering. Equation 24 establishes a limit for the densification of fuel as a function of the structural feature parameters.

3. Volatile Fission-product Kinetics

a. Steady-state Irradiation

Analytical models for volatile-fission-product (VFP) behavior can be constructed, starting from hypotheses of varying complexity and assuming more or less restrictive conditions, that will lead to different degrees of sophistication of the analytical treatment. However, the degree of sophistication required for the description of VFP behavior is directly dependent on our knowledge of the basic physical and chemical processes related to VFP behavior. Considering our insufficient knowledge of in-reactor VFP mechanisms for diffusion and precipitation, all models currently used are based on simple diffusion equations, and the diffusion constants are usually fitted, starting from experimental determinations of release. These models provide calculations of both the release rate and a gross concentration profile of the fission products without taking into account segregation or precipitation in grain boundaries or pores.

With our objective of describing the transient behavior of the VFP, an effort must be made to obtain a more detailed treatment of the distribution of the retained amounts during steady-state irradiation. This requires the adjustment of additional parameters, and for this purpose the DEH experiments should furnish sufficient data.

The first diffusion stage that occurs after a fission product has been formed is its migration to the next grain boundary, where its free energy and diffusion enthalpy change. The diffusion from a spherical grain of a fission product i is described by Fick's equation

$$\frac{\partial N_i}{\partial t} = D_i \Delta^2 N_i + \beta_i - \lambda_i N_i, \qquad i = 1, \ldots, n, \tag{29}$$

where λ_i is the decay constant (a correction for neutron absorption can be introduced in λ) and β_i is the production rate, which, in principle, depends on the

concentration of the predecessors. Unless particular cases are considered, Eq. 29 must be simultaneously solved for a given decay chain. However, the mathematical formalism is not affected by this interdependence, and the treatment will be performed for the single isotope i only. As the boundary condition for Eq. 29, we assume

$$N_i = u_i \quad \text{at } r = a \text{ (grain radius).}$$

The number of atoms arriving at the grain surface in the unit time, if $\lambda \gg (\pi^2/a)\, D_i$ and $t \gg \lambda$, is[4]

$$\frac{dm}{dt} = -4\pi a^2 D_i \left(\frac{\partial N_i}{\partial r}\right)_{r=a} = 4\pi a^2 D_i \frac{\lambda_i}{a}\left(\frac{\beta_i}{\lambda_i} - u\right)\frac{a}{2\sqrt{D_i\lambda_i}}$$

$$= 4\pi a^2 \sqrt{D_i\lambda_i}\left(\frac{\beta_i}{\lambda_i} - u_i\right). \tag{30}$$

The VFP's on the grain boundary have two possible escape mechanisms: diffusion along the grain boundary to the outer pellet surface and percolation flow through the porosity channels via vapor or liquid phase. For the first release mechanisms, the diffusion rate can be calculated following an idea of Turnbull and Friskney.[5] They have proposed to couple the grain-boundary diffusion with the single grain-release rate, using a source term derived from Eq. 30, in the form

$$\beta^1 = \frac{dm}{dt}\left(4\pi a^2 \frac{\delta}{2}\right)^{-1} F_{gp} = \frac{2F_{gp}}{\delta}\left(\frac{\beta_i}{\lambda_i} - u_i\right)\sqrt{D_i\lambda_i}, \tag{31}$$

where $4\pi a^2\delta/2$ is the volume of the grain boundary, assuming a thickness δ. F_{gp} represents the fraction of gas arriving at the grain-grain interface (excluding the grain-pore interface):

$$F_{gp} \approx \frac{\sigma_g}{\sigma_g + \sigma_p},$$

where the σ's are the specific surfaces of pores and grains. The resultant equation for grain-boundary diffusion in a cylindrical pellet is

$$D_i^{gb}\left(\frac{\partial^2 u_i}{\partial r^2} + \frac{1}{r}\frac{\partial u}{\partial r}\right) + \frac{D^{gb}Q_i^*}{RT^2}\frac{dT}{dr}\frac{\partial u}{\partial r} + \frac{2\sqrt{D_i\lambda_i}}{\delta}\left(\frac{\beta_i}{\lambda_i} - u_i\right) - \lambda_i u_i = \frac{\partial u_i}{\partial t}, \tag{32}$$

with the boundary conditions

$$u_i = 0 \quad \text{at } r = R \text{ (R = pellet radius),}$$

$$\frac{\partial u_i}{\partial r} = 0 \quad \text{at } r = 0 \text{ (cylindrical symmetry assumed),}$$

and

$$u_i = 0 \quad \text{at } t = 0 \quad \text{for } 0 \le r \le R.$$

D_i^{gb} is the grain-boundary diffusion coefficient of i for the VFP, and Q_i^* is the heat of transport. Equation 32 can be written in a more compact form as

$$u_t = a_0(r,t)u_{rr} + a_1(r,t)u_r + a_r(r,t)u + d(r,t), \tag{33}$$

where

$$a_0(r,t) = D_i^{gb}(T,t) = D^{gb}(r,t),$$

$$a_1(r,t) = D_i^{gb}(r,t)\left[\frac{1}{r} + \frac{Q^*}{RT(r,t)}\frac{\partial T(r,t)}{\partial r}\right],$$

$$a_2(r,t) = 2\sqrt{D_i(r,t)\lambda_i} - \lambda_i,$$

and

$$d(r,t) = 2\sqrt{D_i(r,t)\lambda_i}\,\beta_i(r,t)/(\delta\lambda_i). \tag{34}$$

Equation 33 can be solved numerically with a finite-difference method. Replacing the derivatives with the respective difference quotients, the approximate solution can be written as

$$u_i(r,t+k) = \sum_{p=-1}^{+1} c_r(r,t)u_i(r+ph,t) + kd(r,t), \tag{35}$$

with

$$c_{-1} = \Lambda a_0(r,t),$$

$$c_0 = 1 - 2\Lambda a_0(r,t) - \Lambda h a_1(r,t) + \Lambda h^2 a_2(r,t),$$

and

$$c_{+1} = \Lambda a_0(r,t) + \Lambda h a_1(r,t) \text{ with } \Lambda = \frac{h}{k^2}. \tag{36}$$

The values $u_i(r,t+k)$ can be successively obtained from Eq. 35, starting from the initial conditions $u_i(r,0) = 0$ and using, for $t > 0$, the boundary conditions

$$u_i(r,t) = 0$$

and

$$u_i(h,t) = u_i(-h,t).$$

The choice of the integration steps of Eq. 35 must satisfy the stability condition

$$\Lambda < \left(2D_i^{gb}\right)^{-1}.$$

The release rate from the pellet surface can be calculated from the diffusion flux

$$|\bar{J}_i| = D_i^{gb}\left(\frac{\partial u_i}{\partial r}\right)_{r=R},$$

where the concentration u_i is restricted to the volume fraction

$$\frac{V^{gb}}{V^g} = \frac{4\pi a^2\delta/2}{\frac{4}{3}\pi a^3} F_{gp} = \frac{3}{2}\frac{\delta}{a}F_{gp}.$$

We finally obtain the release rate

$$\frac{dR_i^{gb}}{dt} = \frac{3}{2}\frac{\delta}{a}F_{gp} \cdot 2\pi R D^{gb}\left(\frac{\Delta u_i}{k}\right)_{r=R}. \tag{37}$$

The amount of VFP escape per unit length of fuel at time t must be calculated at each integration step so that

$$R_i^{gb}(t_n) = \sum_{j=1}^{n}\left(\frac{dR_i^{gb}}{dt}\right)_j \Delta t_j. \tag{38}$$

The concentration profile of the VFP retained within the grains can be drawn with the balance equation

$$c_i(r_k,t_n) = \sum_{j=1}^{n}\left\{\beta_j - \frac{3\sqrt{D_i\lambda_i}}{a}\left[\frac{\beta_j}{\lambda_i} - u_i(r_k,t_j)\Delta t^j\right]\right\}\exp(-\lambda_i\Delta t_j). \tag{39}$$

Finally, the amount trapped in the pores at the time t, is given by

$$P_i(r_k, t_n) = \sum_{j=1}^{n} (1 - F_{gp}) \frac{1 - F}{F} \frac{3\sqrt{D_i \lambda_i}}{a} \left[\frac{\beta_j}{\lambda_i} - u(r_k, t_j) \right] \Delta t^j \exp(-\lambda_i \Delta t_j). \quad (40)$$

Considering the fraction of open porosity F_∞ defined in Sec. II.E.1.a, the amount

$$R_i^P(t_n) = \sum_{k=1}^{\bar{k}} F_\infty P_i(r_k, t_n) \Delta V_k F, \quad (41)$$

where ΔV_k is the volume of the zone of radius r_k, can be assumed as released, while the concentration

$$P_0(r_k, t_n) = (1 - F_\infty) P_i(r_k, t_n) \quad (42)$$

represents the VFP retained in closed pores. In summary, at the end of the steady-state calculation, the following quantities can be evaluated:

$u_i(r_k, t)$ = concentration at the grain boundaries (in atoms/cm^3 grain boundary),

$c_i(r_k, t)$ = concentration in solution within the grains (in atoms/cm^3 fuel),

$P_i^0(r_k, t)$ = concentration trapped in closed pores (atoms/cm^3 porosity),

R_i^P = VFP released via percolation (atoms/cm pellet),

and

R_i^{gb} = VFP released via grain-boundary diffusion (atoms/cm pellet).

These results will enable the eventual transient analysis to start with a sufficiently detailed description of the postirradiation fuel conditions.

b. Transient Release Model

Volatile fission products escape rapidly from fuel subjected to temperature excursions. This phenomenon occurs even when the excursion is limited to short times (a few seconds). This type of release is too rapid to be attributed to long-range diffusion processes, and it is therefore usually explained as a consequence of a fuel burst. However, a more precise approach to this concept is necessary to understand and calculate transient release rates with an analytical treatment.

The following model indicates that an exhaustive treatment of the VFP steady-state behavior and a detailed knowledge of the fuel structure make an accurate description of the rapid transient release processes possible.

The model is based on three assumptions.

(1) The VFP's present on the grain boundaries at the beginning of the transient, after migrating short distances, are trapped in pores.

(2) From the pores, the VFP's escape via a liquid and/or vapor phase through the network channel available at that moment. The release rate is determined by the pressure gradient built up by the temperature excursion. A viscous flow equation can be written for the VFP's in the porous fuel, which is assumed to have a certain permeability coefficient determined by its structural features. The DEH samples should provide the necessary information concerning the structural modification of the fuel during temperature excursions.

(3) After the first stage, where the VFP's present on the grain boundary escape, a second stage is initiated in which the VFP retained within the grains progressively arrive at the grain boundaries at a rate β.

A mathematical treatment is suggested that simultaneously takes into account hypotheses 1-3.

The viscous flow of a fluid is described by Darcy's law as

$$\bar{\varphi} = c\bar{v} = -B_1 c \text{ grad } p, \tag{43}$$

where $\bar{v}$ is the fluid velocity, c is the density of the fluid, and B_1 depends on the viscosity of the fluid and the morphological features of the porous medium, which is assumed to have a fractional porosity $\bar{F}$. If a certain amount of fluid is produced in the medium at a rate β, Eq. 43 can be written as

$$\beta + \text{div}(c\bar{v}) = -F\frac{\partial c}{\partial t},$$

which, in cylindrical coordinates, becomes

$$B_1 c\nabla^2 p + \frac{\partial(B_1 c)}{\partial p}\left(\frac{\partial p}{\partial r}\right)^2 + \beta = F\frac{\partial c}{\partial t}. \tag{44}$$

At this point, an equation of state must be established for the examined fluid to correlate c and p. For some of the fission products that attain their critical temperature during the excursion, we can assume

$$p = cRT,$$

and thus

$$\frac{F}{RB_1}\frac{\partial c}{\partial t} = \frac{\beta}{RB_1} + cT\Delta^2 c + \frac{\partial c}{\partial r}(4c\Delta T)\left(\frac{\partial c}{\partial r}\right)^2 + c\left(\Delta^2 T + \frac{\Delta T^2}{T}\right). \tag{45}$$

Equation 45 is practically applicable to iodine, bromium, cesium, and rubidium in a wide range of accidents. When less volatile products and/or lower temperatures are concerned, a two-phase liquid-vapor system must be considered. In these cases, the pressure is no longer directly dependent on concentration c but is given by

$$p = p_0 \exp(\Delta H_V / RT),$$

where ΔH_V is the heat of vaporization. After straightforward calculations, Eq. 44 becomes

$$\beta + V\left[\frac{\rho^L B_1^L + \rho^G B_1^G E}{1 + C^G(E - 1)} c\nabla p\right] = F\frac{\partial}{\partial t}\left[\frac{\rho^L + \rho^G E}{1 + C^G(E - 1)} c\right], \tag{46}$$

with

$$C^G = \frac{\rho^G}{\rho^G + \rho^L} \simeq \frac{Fp}{RT\rho^L}$$

and

$$E = \frac{c^G}{c^L} \simeq \frac{Fp}{RT\left(c - \frac{Fp}{RT}\right)},$$

where ρ indicates the density, the indexes G and L refer to gas and liquid phases, respectively, and c is the total concentration $c^G + c^L$. Equation 46 accounts simultaneously for evaporation-condensation processes and gas and liquid flow. Equation 45 or 46 can be solved numerically with the boundary conditions

$$c(r, 0) = \left[u(r, t^f)\frac{1 - F}{F}\frac{3\delta}{8a} + p_0(r, t^f)\right] \exp[-\lambda(t - t_f)],$$

where u and p_0 are taken from the steady-state model after an irradiation time t^f. The time $t - t^f$ is the fuel cooling time. The concentration u is now considered as distributed in the porosity volume; i.e.,

$$u(r,t^b)\frac{\pi a^2\delta/2}{F}\frac{1-F}{\frac{4}{3}\pi a^3} = u\frac{1-F}{F}\frac{3\delta}{8a}.$$

Also, we set

$$\frac{\partial c}{\partial r} = 0 \quad \text{at } r = 0 \text{ for } t > 0 \text{ (symmetry condition)}$$

and

$$c(R,t) = 0 \quad \text{for } t > 0 \text{ (external boundary condition).}$$

The release rate per fuel unit length is calculated as

$$\frac{dR}{dt} = -B_1 c\left(\frac{\partial p}{\partial r}\right)_{r=R}, \tag{47}$$

where $\partial p/\partial r$, for Eq. 46, depends uniquely on the temperature gradient of the fuel surface.

(1) Calculation of the Source Term in Eqs. 45 and 46. The amount c_i of VFP retained in the grains at a certain radial position r has been calculated with Eq. 39. Assuming this concentration to be constant in the grains, the transient diffusion equation is written as

$$D_i(t)\nabla k = \frac{\partial k}{\partial t} \qquad \begin{cases} k = c_i^0 \text{ at } t = 0, & 0 \le r \le a, \\ k = c \text{ at } t > 0, & r = a, \end{cases} \tag{48}$$

with the variable substitution

$$d\tau = D_i\, dt \left(\tau = \int_0^t D_i\, dt'\right). \tag{49}$$

Equation 48 can be integrated, obtaining

$$k = c_i^0 - (c_i^0 - c)\left[1 + \frac{2a}{\pi r}\sum^{\infty}\frac{(-1)^n}{n}\sin\frac{n\pi r}{a}\exp(-n^2\pi^2\tau/a^2)\right], \tag{50}$$

and the amount flowing to the grain boundary (φ) is given by

$$\varphi = 4\pi a^2 D \left.\frac{\partial k}{\partial r}\right|_{r=a} = \frac{4\pi a^2 D}{\sqrt{\pi\tau}}(c_i - c),$$

which corresponds, in the intragranular pore volume, to a production rate

$$\beta = \frac{4\pi a^2 D_i(t)}{\sqrt{\pi\tau}} \frac{1 - F}{F} \left(\tfrac{4}{3}\pi a^3\right)^{-1}(c_i^0 - c) = \frac{3D_i(t)}{a\sqrt{\pi\tau}} \frac{1 - F}{F}(c_i^0 - c). \tag{51}$$

(2) Evaluation of the Fuel-permeability Coefficient. The fuel-permeability coefficient B_1 is inversely proportional to the VFP viscosity and to several structural parameters of the fuel. One of the most reliable formulations of the dependence of B_1 on these parameters is given by (see, for example, Ref. 6)

$$B_1 = \frac{Fm^2}{\eta kq} F_\infty, \tag{52}$$

where η is the viscosity coefficient, F_∞ is again the fraction of open porosity, k is a geometrical factor that depends on the channel shape (for ceramic sintered media, k = 2.5), q (tortuosity factor) is the ratio of the actual path traveled by the fluid to the macroscopic permeated distance, and m is the mean diameter of the porosity channels given by the ratio between the pore volume and the pore specific surface; i.e.,

$$m = \frac{F}{\sigma(1 - F)}. \tag{53}$$

Here σ is the specific surface of the solid portion of the fuel measured by usual intercept methods. Finally, the factor q can be estimated only roughly from experimental data on materials comparable to the considered fuel pellets. According to the literature data, q should be 2-3 for UO_2 pellets that are 80-90% of the theoretical density.

References

1. S. Chandrasekhar, Rev. Mod. Phys. 15, 1 (1943).
2. B. Ham, J. Phys. Chem. Sol. 6, 335 (1958).
3. K. Maschke et al., Phys. Stat. Sol. (b) 60, 563 (1973).
4. A. H. Booth, CRDC-721 (1957).
5. J. A. Turnbull and C. A. Friskney (to be published).
6. M. R. J. Wyllie and W. D. Rose, Nature 165, 972 (1950).

Acknowledgments

The author of this appendix thanks Dr. B. R. T. Frost and Prof. R. Lindner for making possible his summer leave at Argonne, and L. R. Kelman and the L. A. Neimark and R. B. Poeppel groups for helpful and stimulating discussions.